MHD simulations of the Reversed Field Pinch

Robert Chahine

N° Ordre: 2017LYSEC56 Année 2017

THESE DE DOCTORAT DE L'UNIVERSITE DE LYON
opérée au sein de l'Ecole Centrale de Lyon

École Doctorale MEGA
Spécialité Mécanique des Fluides

MHD simulations of the Reversed Field Pinch

Soutenue publiquement le 30 Novembre 2017 par

ROBERT CHAHINE

Jury:

OLIVIER AGULLO	Examinateur
WOUTER J.T. BOS	Directeur de thèse
SUSANNA CAPPELLO	Rapporteur
BENJAMIN FAVIER	Examinateur
DANIEL HENRY	Président
PABLO MINNINI	Rapporteur
NICOLAS PLIHON	Invité

Acknowledgements

I couldn't achieve the present work without the assistance and implication of several people. For that, they deserve to be thanked and appreciated.

First, I would like to express my deep gratitude to Dr. Wouter Bos, my supervisor, for his enthusiastic encouragement and useful critiques of this work. The research journey with him started in year 2014 when he was first my internship supervisor. During this journey I learnt a lot from him, like how to simplify a presentation of a complex theoretical work, by watching him explain the universality of non-equilibrium turbulence and convince the domain experts, using hands gestures. I learnt as well the importance of team work and networking when he implicated me in several collaborations. Wouter is an impressive researcher and supervisor, but also he became a great friend, with whom I always enjoyed discussing non-scientific subjects like career development, family, etc.

I would like to offer my special thanks to Dr. Nicolas Plihon for the pleasant collaboration on the dynamo effect which will be presented in Chapter 6. The great enthusiasm he showed to investigate this topic is inspiring.

Advices given by the members of the jury, Professors Cappello and Minnini, and Doctors Agullo, Henry and Favier, has been a great help in correcting this work.

Special thanks should be given to the Microfiche team, Louis, Faouzi, Philippe, Loic, Laurent, Dan, Jean-Louis, Emmanuel, Alex and Mathieu, for the morning coffee and the summer barbecues.

I wish to acknowledge the fluid mechanics pedagogic team: Lionel, Gilles, Jean-Marc, Julian, Christophe, Alexis, Stephane, Pietro, Michel, and all the other colleagues with whom I enjoyed assisting in the Lab courses.

One cannot survive a PhD without his office colleagues. Thank you Donato, Aleksander, Srikanth, Baolin, Quan, Mathieu, Juan, Ming, Diane, Alexis, Alessandro and Thibault for the nice and funny atmosphere in the lab. And one cannot survive the daily life-stress without his close friends supporting him, and for that I would like to thank Michael, Peter, Joseph, Remi, Joane, Rodolphe, Hadi, Antoine and Xaled.

I would particularly like to thank my gorgeous lady for her support, love and encouragement. Thank you Lidia for being by my side the whole way.

Finally, I owe my deepest gratitude to my parents: Alexandre, Marie, Houssam and Hicham. Thank you for supporting me at every moment, believing in me and for being proud of me. You were my all-time motivation to move forward. I dedicate this thesis to you.

Résumé

La dynamique des plasmas de fusion par confinement magnétique dans la configuration Reversed Field Pinch (RFP) est étudiée en utilisant la description magnétohydrodynamique (MHD) incompressible. Une méthode pseudo-spectrale et une technique de pénalisation en volume sont utilisées pour résoudre le système d'équations dans un cylindre. Les simulations numériques montrent que la pression joue un rôle important dans la dynamique des RFP et ne peut pas être négligée. Ainsi, β n'est plus le paramètre principal pour décrire la dynamique des RFPs mais plutôt β'_∇, un nouveau paramètre qui équivaut le rapport du module de gradient de pression et le module de la force de Lorentz. A un autre niveau, l'effet du changement de la section poloïdale du RFP sur la dynamique est étudié. Les simulations des écoulements RFP ayant le même nombre de Lundquist et des sections différentes (circulaire et elliptique), montrent une grande différence dans les spectres et la diffusion turbulente radiale. Finalement, les écoulements RFP sont utilisés pour étudier l'effet dynamo. Les résultats obtenus montrent que les écoulements RFP sont capables d'amplifier un champ magnétique passif qui aura une tendance à être plus non-linéaire que le champ magnétique du RFP dans les régimes turbulents.

Mots clés: magnétohydrodynamique, reversed field pinch, gradient de pression, effet de la géométrie, modes toro´idaux, diffusion turbulente, dynamo cinématique.

Abstract

The dynamics of magnetic fusion plasmas in the Reversed Field Pinch (RFP) configuration are studied using an incompressible magnetohydrodynamics (MHD) description. A pseudo-spectral method combined with a volume penalization method are used to resolve the governing equations in a straight cylinder. Numerical simulations show that the pressure effects on the RFP dynamics cannot be neglected, and thus the β parameter is not adequate to characterize the importance of pressure in the dynamics. A new parameter, β'_∇, which is the ratio of the pressure gradient's magnitude to the Lorentz force's magnitude, is proposed to be the proper parameter to describe the RFP dynamics. Another investigated influence on the RFP dynamics is the shaping of the poloidal cross-section. Simulations of flows with the same Lundquist number and different cross-sections (circular and elliptic) show a clear change in the spectral behaviour, as well as in the radial turbulent diffusion. Finally, the RFP flows are used to study the dynamo effect. Numerical results show that RFP flows are capable of amplifying a seed magnetic field, which will have tendency to be more nonlinear than the RFP magnetic field in the turbulent regime.

Keywords: magnetohydrodynamics, reversed field pinch, pressure gradient, shaping effect, toroidal modes, turbulent diffusion, kinematic dynamo.

Contents

Notations

$\boldsymbol{A}$	Vector potential
A	Surface
a	Major semi-axis of the ellipse
b	Minor semi-axis of the ellipse
β	ratio of the pressure to the square of the magnetic field
$\boldsymbol{B}$	Magnetic field
$\boldsymbol{B}_p$	Poloidal magnetic field
$\boldsymbol{B}_z$	Axial magnetic field
c	Ellipticity
C_A	Alfvén velocity
$\boldsymbol{D}$	Passive magnetic field
$\boldsymbol{E}$	Electric field
E	Energy
F	Field reversal
$\boldsymbol{F}$	Force field
$\mathcal{F}$	Fourier transform
Ha	Hartmann number
H	Magnetic helicity
H_u	Kinetic helicity
$\boldsymbol{I}$	Electric current field
$\boldsymbol{J}$	Current density field
$\boldsymbol{k}$	Wavenumber vector
K	Cross-helicity
$\mathcal{L}$	Length-scale
L_z	Cylinder length
λ	Magnetic diffusivity
m	Poloidal wavenumber / mass
μ	Permeability
n	Toroidal wavenumber / density

ν	Kinematic viscosity
P	Pressure field
P_m	Magnetic Prandtl number
ψ	Magnetic flux
q	Safety factor
R	Major radius
ρ	Density
Re	Reynolds number
R_m	Magnetic Reynolds number
S	Lundquist number
τ_A	Alfvén time-scale
τ_c	Collision time
Θ	Pinch ratio
T	Scalar field
$\boldsymbol{u}$	Velocity field
U	Velocity scale
ω	Vorticity field
$\boldsymbol{z}^{\mp}$	Elsasser variable
$\boldsymbol{\zeta}^{\mp}$	Elsasser variable

Chapter 1

A short introduction to magnetically confined fusion

1.1 Introduction

After the second world war, the industrial sector witnessed a fast global development that led to a large increase in the world's energy consumption. In 2010, the world energy consumption is estimated at 550×10^{18} Joules per year, where the main energy resource, as shown in Figure 1.1(a), was and still is fossil fuel (natural gas, oil and coal). This primary energy resource is vital for factories' operation, transportations and electric power generation. However, its reserves are expected to seriously diminish starting year 2051 (see Figure 1.1(b)).

Alternative sources of energy are thus proposed to gradually replace fossil fuel, like solar energy, wind energy and nuclear fission power. Solar and wind energies are relatively easy to collect, but are for the near future not expected to generate sufficient amounts of energy to replace fossil fuels. Nuclear fission yields large amounts of radioactive waste and its safety risks are well-known. Nuclear fusion, if achieved, could possibily generate larger amounts of energy by using two isotopes of hydrogen that can be obtained by processing water, a resource considered as almost unlimited. Furthermore, nuclear fusion is not limited by any weather constraints and generates a small amount of nuclear waste compared to nuclear fission. In the latter, heavy uranium atoms are split into other heavy atoms and release thermal energy, while the fusion of hydrogen's isotopes (deuterium and tritium) generates light particles like helium and releases a colossal amount of thermal energy. Therefore, fusion seems a promising alternative to fossil fuels.

A controlled thermonuclear fusion reaction can be achieved using two methods: inertial

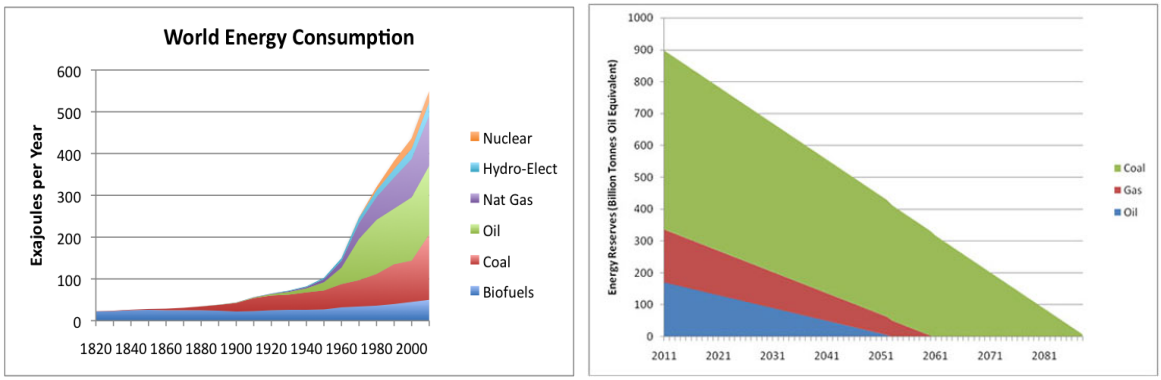

(a) (b)

Figure 1.1: (a) Time evolution of the world consumption of different energy resources [1], (b) expected time evolution of fossil energy reserves [2].

confinement fusion and magnetic confinement fusion. In the first, a high-energy laser beam hits a pellet that consists of a deuterium-tritium mixture, heats it and compresses it, thus initiating the fusion reaction. In the second, a deuterium-tritium (several other compnents can also be used, but deuterium-tritium is considered the most promising mixture) plasma is heated up to temperatures of the order of $150 \times 10^6\ K$ [3] to initiate the fusion reaction. This can be done by several methods, like ohmic heating which consists in inducing a current in the conductor plasma, neutral beam injection which consists in introducing high-energy particles that interact with the plasma, and radio-frequency heating which is done by sending high-frequency electromagnetic waves with suitable wavelength and polarization so its energy can be transferred to charged particles in the plasma. At high temperatures, the plasma is ionized and hence becomes controllable by magnetic fields. This is the concept of a Magnetic Confinement Fusion (MCF) reactor, where strong magnetic fields are used to hold the hot ionized plasma isolated from the reactor's wall, since no material on planet earth can support such high temperatures.

In the past decades, several magnetic configurations were proposed to achieve controlled thermonuclear fusion reactions. Between these configurations, three configurations remained most promising: the tokamak, the Reversed Field Pinch (RFP) and the stellarator. In the remainder of this chapter, we will briefly introduce each of these configurations.

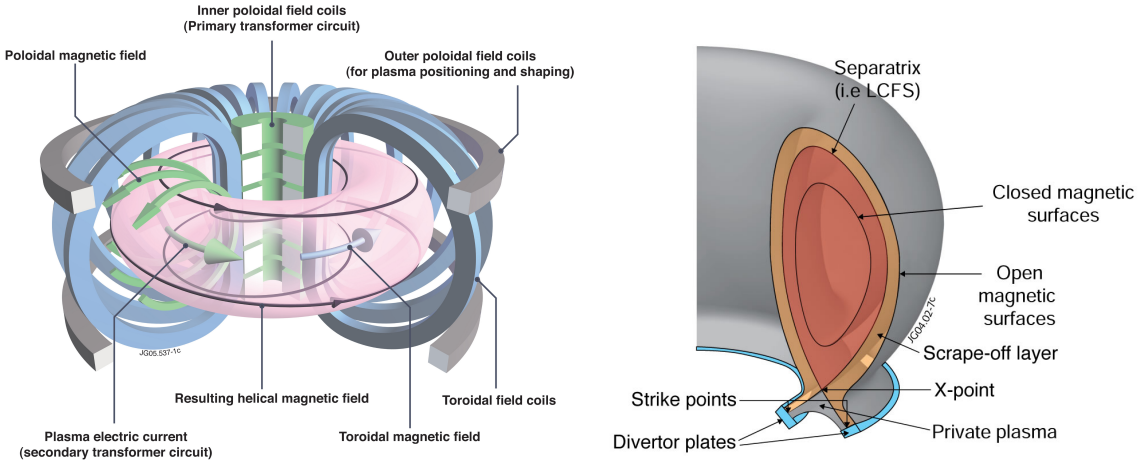

(a) (b)

Figure 1.2: (a) Tokamak magnetic components, (b) poloidal cross-section of a tokamak showing the Last Closed Flux Surface (LCFS).

1.2 Tokamak

Historically, the construction of the first experimental tokamak, named *T-3*, started in 1956 at the Kurchatov Institute Moscow. It was not until 1968 that this Soviet institute made a breakthrough on their upgraded tokamak, the *T-4*, in Novosibirsk, where the first ever quasistationary thermonuclear fusion reaction was obtained. Indeed, a fusion reaction was observed, but the energy to obtain the required conditions was orders of magnitude larger than the energy released from the reaction. Nevertheless this result motivated earlier fusion-energy researchers, and made the tokamak a candidate to achieve sustainable nuclear fusion. In consequence, the construction and operation of experimental tokamaks started in different parts of the world, like the Joint European Torus (JET) in the UK in 1973, the Japan Tokamak 60 (JT-60) in Japan in 1985, Tore Supra in France in 1988, etc. Later on, nuclear fusion research became of major interest for the international political powers, and this led to the collaboration of seven international parties (China, the European Union, India, Japan, Korea, Russia and the United States) to construct the International Thermonuclear Experimental Reactor (ITER) in Cadarache, France. ITER is a D-shaped tokamak, designed to produce 500 MW of fusion power from 50 MW of input power. It is expected to start operating in 2032. The geometrical and electrical parameters of different tokamak devices are shown in table 1.3.

The tokamak is a toroidal magnetic confinement fusion (MCF) reactor, characterized by its coils enveloping a plasma-containing vessel, and a vertical solenoid installed at the center

(Figure 1.2a). The coils generate the toroidal magnetic field $\boldsymbol{B}_t$, while the central solenoid generates a toroidal electric current $\boldsymbol{I}_t$ in the plasma, which induces a poloidal magnetic field $\boldsymbol{B}_p$. The resulting helical magnetic field, with a toroidal component several times larger than the poloidal one, is supposed to hold the plasma isolated from the vessel's walls. Metallic plates, called "limiters", are installed close to the wall to set the plasma confinement boundary, thereby protecting the vessel walls from the hot plasma. Nowadays, limiters are replaced in some tokamaks by 'divertors' (see Figure 1.2b) which set the confined plasma boundary, called the Last Closed Flux Surface (LCFS), using magnetic fields instead of solid surfaces.

The design and operation of large scale tokamaks is a challenge for plasma-physics, material-engineering and a number of other disciplines. Some major problems are due to the interaction of the hot plasma with the limiters and divertors, which are subjected to high heat loads and high fluxes of deuterium. Metallic impurities are formed through the interaction of the plasma with the walls and transported by the plasma. High concentrations of impurities can dilute the plasma and interrupt the fusion reaction. Avoiding this is one of the current challenges in tokamak design. Actual research on divertors aims to decrease its rate of impurity injection and control its heat absorption.

Another challenge for tokamak confinement is disruptive processes. A disruption, generated by a nonlinear MHD instability, leads to the loss of magnetic confinement, hence magnetic and thermal energy are rapidly lost, and the fusion reaction is abruptly terminated. Disruptions represent a great risk to the vessel as the highly accelerated electrons can damage the wall once the confinement is lost. Control of MHD instabilities is therefore a major issue in tokamak research.

A breakthrough in tokamak physics was the observation of the L-H transition. When the input power exceeds a certain threshold, the plasma reorganizes into a self-sustained regime where the radial transport from the hot central core to the edge region diminishes due to the formation of a shear flow near the boundary, called a transport barrier. This regime, characterized by the suppression of turbulence, is called high confinement or H-mode, while the regime before the formation of the transport barrier is called low confinement or L-mode [4]. When the L-H transition occurs, the plasma accumulates near the transport barrier. Therefore, during this high confinement regime strong pressure and density gradients are observed near this barrier, that increase the risk of a disruptive instability where the barrier relaxes and ejects the plasma to the edge region. This instability is called an Edge Localized Mode (ELM). Current studies on reducing ELMs and disruptions include the injection of different impurities in order to distribute uniformly the power density over the vessel walls and minimize possible excessive localized heat load.

MHD instabilities and the associated violent disruptions are the price one pays in tokamaks in order to have a well-controlled magnetic field. Indeed, an alternative is to allow the MHD instabilities to take place and to try to control the dynamics resulting from these

instabilities. This is the strategy followed in Reversed Field Pinches that we will discuss now.

Machine	R_0	a	I_t	B_t
ITER	6.2 m	2 m	15 MA	5.3 T
JET	2.96 m	1.25-2.10 m	3.2-4.8 MA	3.45 T
Tore supra	2.25 m	0.70 m	1.7 MA	4.5 T
JT-60	3.4 m	1 m	2 MA	4 T
ASDEX	1.65 m	0.50-0.80 m	1.6 MA	3.1 T
DIII-D	1.67 m	0.67 m	3 MA	2.2 T

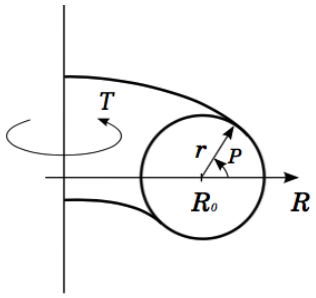

Figure 1.3: (Left) geometrical and electrical parameters of different tokamak devices, where R_0 is the major radius of the torus and $r = a$ the minor radius of the poloidal cross-section, (right) schematic figure of the toroidal geometry.

1.3 Reversed Field Pinch

The Reversed Field Pinch (RFP) is a toroidal MCF reactors with a magnetic geometry similar to the one of the tokamak: an imposed toroidal magnetic field combined with a poloidal magnetic field, associated with an induced toroidal current. Meanwhile, RFP differs from a tokamak by the magnitude of the toroidal magnetic field, which is of the same order as the one of the poloidal magnetic field.

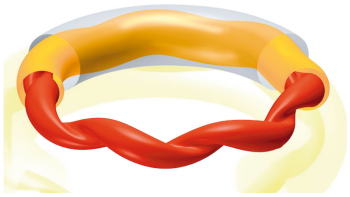

Figure 1.4: Schematic figure of the helical magnetic field in RFP.

When the toroidal current exceeds a certain threshold (Kruskal-Shafranov threshold), a helical MHD instability is triggered. This instability gives in general rise to a complex chaotic interplay of helical structures of different spatial frequency, reorganizing the plasma into a quasi-stationary state where the toroidal component reverses close to the boundary, whence the name of this reactor. The self-organization of this toroidal magnetic field, which has the originally imposed sign in the center and reversed close to the boundary, makes the RFP a disruption-free reactor since it corresponds to a full MHD relaxation of the magnetic field [5]. Hence, no limiters or divertors are needed in RFPs to protect the vessel from disruptive events. However, this self-organization leads to a magnetic turbulence and chaos that might deteriorate the confinement.

The first reversal states were observed in the ZETA machine at Culham (UK) in 1958, when the RFP dynamics were still unknown. ZETA was a toroidal pinch (z-pinch) created

by a toroidal magnetic field B_t using external coils, and a toroidal current I_t in the plasma. Experiments done on ZETA showed the remarkable feature of plasma relaxation: the plasma goes from an initial highly unstable state to a largely stable one, where the sign of the toroidal field at the edge is reversed relatively to the central one when the toroidal current is large enough. In 1974, J.B Taylor proposed a remarkable relaxation theory [6] which illustrates the reversal phenomenon observed in ZETA experiment and predicts the plasma to become multi-helical and chaotic at high energy regimes. This theory will be outlined in Chapter 2.

After the interesting results obtained from the ZETA experiments, construction and operation of multiple RFP devices helped better understanding of RFP dynamics, like MST in the USA, RFX-mod in Italy, EXTRAP T2R in Sweden, RELAX in Japan, and recently the KTX machine in China. The geometrical and electrical parameters of different RFP devices are shown in table 1.1. In the 2000s quasi-single-helicity (QSH) states were detected within turbulent flows in the RFX experiment [7–9]. These states are characterized by the appearance of a quiescent helical structure in the plasma core, which improves the plasma confinement [10–12]. These results motivated a small part of the fusion community to reconsider the RFP as a suitable candidate for nuclear fusion [13]. Recent studies show that high current regimes [14] and helical magnetic perturbations [15, 16] are the key to reduce magnetic turbulence in RFPs. Furthermore, increasing toroidal current is beneficial for RFPs since it increases the ohmic heating of the plasma, allowing to approach temperatures at which fusion can take place.

Machine	R_0	a	I_t	B_t
MST	1.5 m	0.5 m	0.6 MA	-
RFX-mod	2 m	0.459 m	2 MA	-
EXTRAP T2R	1.24 m	0.18 m	300 kA	-
RELAX	0.51 m	0.25 m	80 kA	-
KTX	1.4 m	0.4 m	1 MA	0.7 T

Table 1.1: Geometrical and electrical parameters of different RFP devices.

1.4 Stellarator

Both the tokamak and the RFP have a helical magnetic field, which is essential to obtain a correct confinement. The poloidal magnetic field is obtained by an imposed toroidal current. An alternative way to obtain a helical magnetic field is to change the position of the poloidal coils, as illustrated in Figure 1.5. This is the idea behind the stellarator.

The stellarator was invented by Lyman Spitzer in 1951 at the Princeton Plasma Physics

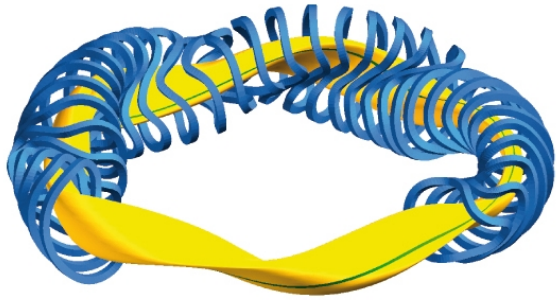

Figure 1.5: Design of a stellarator where the coils are in blue, the plasma in yellow and magnetic field line in green.

Laboratory (PPPL). It was in 1953 that the first model A's operation started and it demonstrated improved confinement. Later on, the reccurence of the "pump-out" technical issue that led to the loss of plasma in larger devices, demonstrated poor performance of the stellarator model. With the breakthrough made in the tokamak at the Kurchatov Institute, the fusion community lost its interest in constructing a commercial fusion reactor based on the stellarator model, and focused its interest on the tokamak model. The later problems and difficulties encountered in tokamaks were similar to the previous ones observed in the stellarator. This, with the development of new methods to manufacture improved magnetic coils, pushed a part of the fusion community to reconsider the stellarator as a promising reactor. Hence, multiple large devices have been built worldwide, namely the Wendelstein 7-X (W7-X) in Germany, Helically Symmetric eXperiment (HSX) in the USA and the Large Helical Device (LHD) in Japan. A remarkable breakthrough was made in February 2016 when the first hydrogen plasma was produced in W7-X, where the plasma electron temperature reached 10^8 K and the ion temperatures reached 10^7 K. The next goal for W7-X planned to be achieved in 2021 is to operate for a 30 minutes duration. Reaching such a phase will be a great demonstration of continuous operation which is an essential feature of a future nuclear fusion reactor.

The stellarator has a toroidal geometry like the two previous reactors, however its magnetic configuration is different. In this reactor, the central solenoid is absent, hence no toroidal current is driven in the plasma, and the imposed magnetic field is generated by complex poloidal coils that are not toroidally symmetric. These coils are shaped in a sophisticated way to assure the twist of the magnetic field, shown in Figure 1.5(a), in order to avoid the instabilities seen in purely toroidal reactors. The divertor geometry in a stellarator is significantly different from the one in tokamaks. Unlike the poloidal divertor in tokamak that imposes a separatrix by introducing additional poloidal fields, the stellarator's divertor configuration is based on the interaction with exhibited edge magnetic structures. It

consists in installing several plates along different regions of the vessel's wall which collect undesirable particles and impurities, and neutralize them so they can be removed subsequently by a pumping system. Since the toroidal symmetry is absent in stellerators, the divertor is three-dimensional and the magnetic field at the edge presents a stochastic layer. Numerical study of the edge stochastic behavior becomes difficult since it requires 3D transport models where no flux surfaces exist. In addition, the precision of the fabrication and assembly of coils and coil support structures raises the complexity of the design of stellarator reactors with respect to tokamaks and RFPs. However, the main advantage of stellarators is their ability to operate continuously due to their steady state magnetic field, unlike tokamaks which operate in pulsed mode, since the central solenoid that induces plasma current is a transformer coil which can only operate in pulsed mode. Furthermore, stellarator's dynamics are disruption free and do not suffer from any current-driven instabilities.

1.5 Overview of the rest of this manuscript

We have briefly described the three principle MCF-geometries. Technologically, the tokamak is the most advanced one, and a large part of the global fusion-research budget is spent on the enormous technical difficulties which are encountered in its design and operation. The stellarator seems a promising reactor but its geometry is fairly complicated.

The technically easiest configuration is the RFP, but its development is much more immature than that of tokamaks. However, if the flow within an RFP can be understood and controlled, RFPs might become the fusion reactor of the future, especially since their magnetic field is easier to create than in tokamaks, their geometry simpler compared to stellarators, and the plasma heating needed to attain fusion conditions is obtained by the Joule dissipation in the plasma itself, unlike in tokamaks, where additional heating is required to obtain fusion conditions. In the remainder of this manuscript we will focus on the RFP geometry and try to further contribute to the understanding of the RFP within the MHD description.

In the next chapter, we will first briefly discuss the different plasma descriptions and some key-features of RFP dynamics, followed by the discussion of the numerical methods employed in this thesis in chapter 3. In chapter 4 we will focus on the influence and the role of the pressure in RFPs. Then in chapter 5 we will see how the shape of the plasma containing vessel modifies the dynamics. Finally in chapter 6 we will further study the magnetic field modification and dynamo observed in cylindrical MHD simulations.

Chapter 2

Plasma description and the Reversed Field Pinch

As soon as the international community started to consider nuclear fusion as a promising source of energy, building a test reactor became a priority. In order to design a successful reactor, two issues have to be studied among other things: the fusion plasma dynamics, and the geometrical configuration of the reactor. As will be shown in chapter 5, these two features are strongly related, since the geometry will influence the dynamics. Changing the geometry of a reactor after construction is obviously complicated, given the nature of the reactors. Indeed after construction only minor modifications are possible so that numerical tests in the conception phase are primordial. For this to be successful, a precise enough description of the plasma is needed. The choice of the description is not straightforward.

In hydrodynamics, the collective behavior of fluid particles in most applications can be described by a continuum description, and the macroscopic velocity can be captured by the Navier-Stokes equations. The individual Boltzmann particle dynamics can thereby be simplified dramatically. For plasmas such a simplification is not straightforward, and a whole hierarchy of models exists, ranging from detailed particle dynamics (the Vlasov-equation) towards a continuum description (Magnetohydrodynamics (MHD)). Depending on the precise application, a more or less precise description of the plasma dynamics is needed.

In early fusion research, ideal MHD was used to derive analytical models for magnetostatic equilibria. An example is the famous Grad-Shafranov equation [17, 18]. Ideal MHD was used as well in variational approaches [6] to study RFP dynamics in an attempt to describe the reversal phenomenon observed in the ZETA machine. Such models provided reasonable insights on the plasma dynamics and instabilities in RFPs when Direct Numerical Simula-

tions (DNS) were not yet capable to compute global plasma dynamics at the reactor scale. Later on, with the growth of computational power, highly resolved MHD simulations and experiments proved that the behavior of the RFP plasma is not ideal. Resistive edges play a major role in the field reversal phenomenon, and the plasma gets self-organized in the range of some parameters leading to a better confinement. We will now briefly discuss some plasma descriptions. Note that in order to be concise, we give a very much simplified outline of the different descriptions. For further details we refer to the reference papers and textbooks on the different subjects.

2.1 The Vlasov equation and the gyrokinetic model

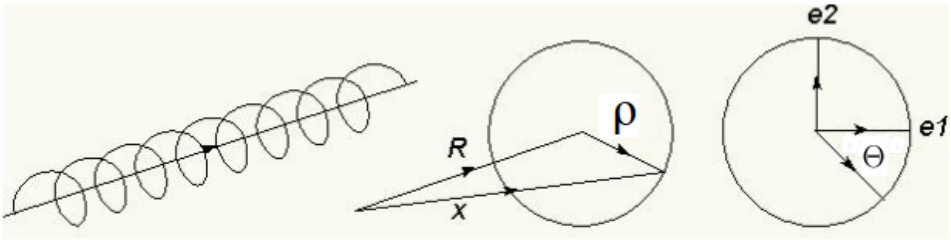

Figure 2.1: (Left) The helical trajectory of the charged particle around a field line, (middle, right) the gyrokinetic coordinates.

In hydrodynamics, the Boltzmann description considers the statistical behavior of a fluid by calculating the probability distribution of the position and the velocity of each particle at instant t. Analytically, the Boltzmann equation is derived by considering first the probablility density function $f(\boldsymbol{x}, \boldsymbol{v}, t)$ in a unit phase-space unit volume $d^3\boldsymbol{x}d^3\boldsymbol{v}$. If an external force $\boldsymbol{F}_e$ is exerted on each particle, and in the absence of particle collisions, the new position at $t + \Delta t$ is $\boldsymbol{x} + \boldsymbol{v}\Delta t$ and velocity $\boldsymbol{v} + (\boldsymbol{F}_e\Delta t)/m$, where m is the particle's mass. Furthermore, the probability density function must satisfy,

$$f(\boldsymbol{x} + \boldsymbol{v}\Delta t, \boldsymbol{v} + (\boldsymbol{F}_e\Delta t)/m, t + \Delta t)d^3\boldsymbol{x}d^3\boldsymbol{v} = f(\boldsymbol{x}, \boldsymbol{v}, t)d^3\boldsymbol{x}d^3\boldsymbol{v}, \tag{2.1}$$

and thereby its total derivative is,

$$\begin{aligned} \frac{df}{dt} &= \frac{\partial f}{\partial t}\frac{dt}{dt} + \frac{\partial f}{\partial \boldsymbol{x}}\frac{d\boldsymbol{x}}{dt} + \frac{\partial f}{\partial \boldsymbol{v}}\frac{d\boldsymbol{v}}{dt} \\ &= \frac{\partial f}{\partial t} + \boldsymbol{v}\cdot\frac{\partial f}{\partial \boldsymbol{x}} + \frac{\boldsymbol{F}_e}{m}\cdot\frac{\partial f}{\partial \boldsymbol{v}} = 0 \end{aligned} \tag{2.2}$$

This is called the collisionless Boltzmann equation. When the fluid is a collisionless plasma, strongly magnetized, the external force is the Coulomb force and equation (2.2) becomes

the Vlasov equation,

$$\frac{\partial f}{\partial t} + \boldsymbol{v} \cdot \frac{\partial f}{\partial \boldsymbol{x}} + \frac{q}{m}\Big(\boldsymbol{E} + \frac{1}{c}\boldsymbol{v} \times \boldsymbol{B}\Big) \cdot \frac{\partial f}{\partial \boldsymbol{v}} = 0, \tag{2.3}$$

where c is the speed of light, $\boldsymbol{E}$ the electric field and $\boldsymbol{B}$ the magnetic field. These quantities are described by the Maxwell equations,

$$\nabla \cdot \boldsymbol{E} = \frac{\rho_e}{\varepsilon_0}, \tag{2.4}$$

$$\nabla \cdot \boldsymbol{B} = 0, \tag{2.5}$$

$$\nabla \times \boldsymbol{E} = -\frac{\partial \boldsymbol{B}}{\partial t}, \tag{2.6}$$

$$\nabla \times \boldsymbol{B} = \frac{1}{\varepsilon_0 c^2}\Big(\boldsymbol{J} + \varepsilon_0 \frac{\partial \boldsymbol{E}}{\partial t}\Big), \tag{2.7}$$

where ρ_e and ε_0 are the total electric charge density and the permittivity of vacuum, respectively.

The trajectory of a charged particle in a magnetic field is a combination of a fast rotation around the field line, also called guiding center, and a slow translation along this line. The resulting movement is a helix winding around the magnetic line as shown in Figure 2.1. In the gyrokinetic model, the gyromotion is considered irrelevant, thus only the guiding center's motion is described. This is done first by combining the Vlasov equations and the following gyrokinetic variables change,

$$\boldsymbol{x} = \boldsymbol{R} + \boldsymbol{\rho}, \tag{2.8}$$

where $\boldsymbol{\rho}$ is the gyroradius. Then the resulting equations are gyrophase-averaged $\langle \cdots \rangle = (2\pi)^{-1} \oint \cdots d\theta$, leading to the final equation,

$$\frac{\partial \langle f \rangle}{\partial t} + \frac{\partial \boldsymbol{R}}{\partial t} \cdot \frac{\partial \langle f \rangle}{\partial \boldsymbol{R}} + \frac{\partial v_\parallel}{\partial t} \frac{\partial \langle f \rangle}{\partial v_\parallel} = 0, \tag{2.9}$$

where $v_\parallel = \boldsymbol{v} \cdot \boldsymbol{B}/B^2$, $\langle f \rangle = \langle f \rangle(\boldsymbol{R}, \mu, v_\parallel, t)$, $\mu \approx v_\perp^2/(2B)$, $v_\perp = \sin\theta \boldsymbol{e}_1 + \cos\theta \boldsymbol{e}_2$, and the subscripts $\parallel$ and $\perp$ means respectively parallel and orthogonal to the magnetic field $\boldsymbol{B}$(for detailed demonstration see [19, 20]).

The gyrokinetic approximation is a highly detailed description of a plasma, for instance, used to study microturbulence and particle transport in tokamaks driven by ion temperature gradient (ITG) and electron temperature gradient (ETG) modes.

The gyrokinetic model is effectively 5D instead of 6D since the gyro-averaging reduces the system by one dimension. This reduces the complexity, but it is in particular the timescales which are changed. The gyro-averaging removes the fast gyrofrequency which allows to win orders of magnitude of computational time. However, even so the gyrokinetic system remains a very expensive system compared to continuum approaches and only long simulations on the world's largest supercomputers allow to compute parts of a reactor on fusion relevant timescales [21].

The simplest continuum approach, MHD, will be discussed in the following.

2.2 The MHD description

The Magnetohydrodynamic (MHD) approximation is commonly used to study the global dynamics of fusion plasmas over time scales relevant to the bulk dynamics. MHD equations were first derived from kinetic equations by Braginskii [22]. The main assumptions are that one can neglect the electron inertia relative to the ion inertia and that the plasma can be considered charge-neutral. In the following, we derive the MHD equations using the force balance applied on a conducting fluid element containing charged particles.

Let's consider a particle carrying a charge q moving with velocity $\boldsymbol{u}$ in a medium exposed to a time-varying magnetic field $\boldsymbol{B}$. This particle is subject to three electromagnetic forces: the electrostatic or Coulomb force $\boldsymbol{f}_c = q\boldsymbol{E}_c$, the force exerted by the time-varying magnetic field $\boldsymbol{f}_i = q\boldsymbol{E}_i$, and the Lorentz force $\boldsymbol{f}_l = q(\boldsymbol{u}\times\boldsymbol{B})$. $\boldsymbol{E}_c$ and $\boldsymbol{E}_i$ are respectively the electric field resulting from the interaction of the charge with other charges, and the electric field induced by $\boldsymbol{B}$. Furthermore, $\boldsymbol{B}$ and $\boldsymbol{E}_i$ are related by Faraday's law,

$$\nabla \times \boldsymbol{E}_i = -\frac{\partial \boldsymbol{B}}{\partial t}, \tag{2.10}$$

and $\boldsymbol{E}_c$ is curl-free (Coulomb's law),

$$\nabla \times \boldsymbol{E}_c = \boldsymbol{0}. \tag{2.11}$$

The sum of the three forces, $\boldsymbol{f}_r$, can be written in terms of a resulting electric field $\boldsymbol{E}_r$,

$$\boldsymbol{f}_r = q(\boldsymbol{E}_c + \boldsymbol{E}_i + \boldsymbol{u} \times \boldsymbol{B}) = q\boldsymbol{E}_r. \tag{2.12}$$

Now if we consider a unit volume of a conducting fluid element dV, the resulting electromagnetic force $\boldsymbol{F}_r$ is obtained by summing equation (2.12) over dV. The sum of q gives the charge density ρ_e, and the sum of $q\boldsymbol{u}$ gives the current density $\boldsymbol{J}$. The volumetric version of (2.12) is therefore

$$\boldsymbol{F}_r = \rho_e(\boldsymbol{E}_c + \boldsymbol{E}_i) + \boldsymbol{J} \times \boldsymbol{B}, \tag{2.13}$$

where $\boldsymbol{F}_r$ is the electromagnetic force per unit volume. The first term on the r.h.s of equation (2.13) is negligible for fluids moving with a velocity much smaller than the one of light, and the current density $\boldsymbol{J}$ is given by Ampere's law,

$$\nabla \times \boldsymbol{B} = \mu \boldsymbol{J} \tag{2.14}$$

where μ is the magnetic permeability. The force on a fluid element due to the conducting character of the fluid is therefore $\boldsymbol{F}_l = \boldsymbol{J} \times \boldsymbol{B}$. This force should be added to the other forces, due to the pressure gradient and viscous friction.

The velocity field's evolution of a conducting fluid with density ρ and kinematic viscosity ν, is then described by the Navier-Stokes equation combined with the Lorentz force,

$$\rho(\frac{\partial \boldsymbol{u}}{\partial t} + \boldsymbol{u} \cdot \nabla \boldsymbol{u}) = -\nabla P + \rho\nu\Delta \boldsymbol{u} + \boldsymbol{J} \times \boldsymbol{B}. \tag{2.15}$$

In order to obtain the induction equation describing the evolution of the magnetic field, we need to apply Ohm's law first. It yields,

$$\boldsymbol{J} = \sigma \boldsymbol{E}_r = \sigma(\boldsymbol{E}_c + \boldsymbol{E}_i + \boldsymbol{u} \times \boldsymbol{B}), \tag{2.16}$$

where σ is the conductivity of the fluid. Taking the curl of (2.16) and combining it with (2.10) and (2.11) gives the induction equation,

$$\frac{\partial \boldsymbol{B}}{\partial t} = \nabla \times (\boldsymbol{u} \times \boldsymbol{B}) - \nabla \times \frac{\boldsymbol{J}}{\sigma}. \tag{2.17}$$

Considering that $\boldsymbol{B}$ is solenoidal ($\nabla \cdot \boldsymbol{B} = 0$), and noting that $\nabla \times \nabla \times \boldsymbol{B} = -\Delta \boldsymbol{B}$, equation (2.17) simplifies to

$$\frac{\partial \boldsymbol{B}}{\partial t} = \nabla \times (\boldsymbol{u} \times \boldsymbol{B}) + \lambda \Delta \boldsymbol{B}, \tag{2.18}$$

with $\lambda = (\mu\sigma)^{-1}$ the magnetic diffusivity.

In the following we will consider the MHD description stated in Alfveńic variables. This means that all velocities are normalized using the Alfveń velocity, $C_A = B_0/\sqrt{\rho\mu}$, where B_0 is a reference magnetic field (typically the imposed toroidal or poloidal magnetic field). The current density is normalized such that $\boldsymbol{J} = \nabla \times \boldsymbol{B}$. Using this normalization, the Navier-Stokes equation becomes

$$\frac{\partial \boldsymbol{u}}{\partial t} + \boldsymbol{u} \cdot \nabla \boldsymbol{u} = -\nabla P + \boldsymbol{J} \times \boldsymbol{B} + S^{-1}\Delta \boldsymbol{u}, \tag{2.19}$$

where $S = C_A\mathcal{L}/\nu$ is the viscous Lundquist number and $\mathcal{L}$ is a characteristic length-scale.

2.3 Ideal MHD

Equations (2.15) and (2.18) constitute without their dissipative terms on the r.h.s, the ideal MHD equations. This is the most basic single-fluid model, commonly used for determining the macroscopic equilibrium and stability properties of fusion plasmas. These equations give rise to a number of conservation laws. The conserved quantities are:

- mass,

$$\frac{dM}{dt} = 0, \tag{2.20}$$

we will consider in the following incompressible flow, so that mass conservation can be expressed locally by the constraint $\nabla \cdot \boldsymbol{u} = 0$.

- total energy,

$$\frac{d(E_{kinetic} + E_{magnetic} + E_{thermal})}{dt} = \frac{d}{dt}\int_V (\rho\frac{v^2}{2} + \frac{B^2}{2} + \frac{p}{\gamma - 1}) \quad dV = 0, \tag{2.21}$$

in our study, where the flow is incompressible and the density constant, the temperature does not influence the flow so that the conservation of energy of the flow is given by $E_{kinetic} + E_{magnetic} = cst$.

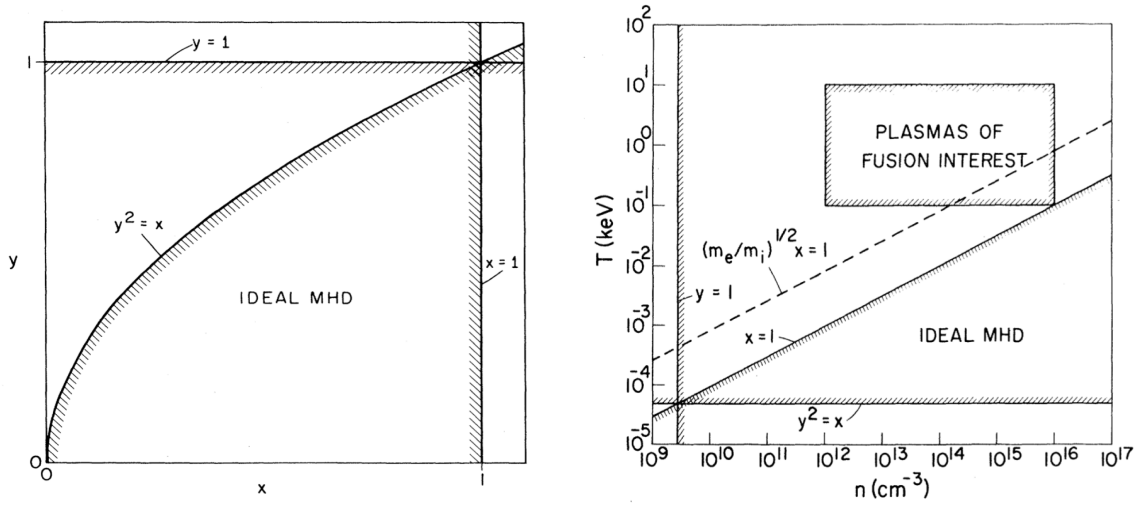

(a) (b)

Figure 2.2: (a) Region of validity of the ideal MHD model in terms of the normalized variables x and y, (b) n and T for fixed $\beta = 0.05$ and $a = 1$m. (Taken from [23])

These two conservation laws concern the most intuitive quantities. Two other quantities are conserved by the flow in the absence of dissipation and are specific to the MHD system. The first of these is the cross-helicity,

$$\frac{dK}{dt} = \frac{d}{dt}\int_V \boldsymbol{u}\cdot\boldsymbol{B} \quad dV = 0, \tag{2.22}$$

This quantity measures the alignment of the velocity and the magnetic field. This alignment is intimately related to the nonlinear coupling of the MHD equations as we will see in section 6.4.2. The other quantity is the magnetic helicity,

$$\frac{dH}{dt} = \frac{d}{dt}\int_V \boldsymbol{A}\cdot\boldsymbol{B} \quad dV = 0, \quad \text{with} \quad \boldsymbol{B} = \nabla\times\boldsymbol{A}, \tag{2.23}$$

where A is the magnetic potential. Magnetic helicity is the magnetic equivalent of the helicity $H_u = \int_V \boldsymbol{u}\cdot(\nabla\times\boldsymbol{u})dV$, an invariant of the Navier-Stokes equations in the absence of the Lorentz-force. The conservation of magnetic helicity is the key ingredient in Taylor's theory [6] of plasma relaxation in RFPs. This theory will be discussed in detail in section 2.5.

In [23], it is shown that ideal MHD requires electrons and ions to be collision dominated, hence the viscosity becomes negligible. In consequence, three independent conditions must be satisfied: small gyroradius, large collisionality and small resistivity. These conditions can be respectively written as follows,

$$y = \frac{r_i}{a} << 1, \tag{2.24}$$

$$x = \frac{v_i\tau_c}{a}\sqrt{\frac{m_i}{m_e}} << 1 \tag{2.25}$$

$$\frac{y^2}{x} = \frac{r_i^2}{a}\frac{1}{v_i\tau_c}\sqrt{\frac{m_e}{m_i}} << 1. \tag{2.26}$$

where x and y are two dimensionless variables introduced to simplify the discussion, r_i the ion gyroradius, a an MHD lengthscale, m_i the ion's mass, m_e the electron's mass, v_i the ion thermal transit velocity across a, and τ_c the collision time. The ideal MHD limit is shown in figure 2.2. It corresponds to the common region inside the dashed lines, that represent the previous mentioned conditions. In order to know wether the fusion plasma belongs to the ideal MHD region or not, conditions (2.24), (2.25) and (2.26) need to be written in terms of the plasma's measurable properties: the density n (in cm^{-3}) and the temperature T (in keV). This is done by assuming the parameter $\beta = 2\mu_0 nT/B^2$ constant, $\tau_c = 18$, and considering m_i as the mass of deuterium ion. The new conditions are:

$$y = 2.28\times10^5\sqrt{\frac{\beta}{a^2 n}} << 1, \tag{2.27}$$

$$x = 9.88 \times 10^{17} \frac{T^2}{na} << 1, \tag{2.28}$$

$$\frac{y^2}{x} = 5.26 \times 10^{-8} \frac{\beta}{aT^2} << 1. \tag{2.29}$$

Previous experiments and studies show that fusion plasma density and temperature lie in the range

$$\begin{aligned} 10^{12}\ \text{cm}^{-3} < n < 10^{16}\ \text{cm}^{-3}, \\ 0.1\ \text{keV} < T < 10\ \text{keV}. \end{aligned} \tag{2.30}$$

The plot of fusion plasma range (2.30) and conditions (2.27), (2.28) and (2.29) for $a = 1$ m and $\beta = 0.05$ is shown in figure 2.2. It is clear that the small gyroradius (2.27) and negligible resistivity (2.29) conditions are satisfied, however the large collisionality condition is not. Now if one considers a less restrictive collisionality by neglecting the ion-electron equilibration in condition (2.25) or (2.28), the new condition $\sqrt{m_e/m_i}\, x << 1$ is satisfied by a part of the fusion plasma, and hence it can be modelled using MHD. However, this empirical model based on multiple restrictive hypotheses cannot take into account all MHD instabilities, but can provide an approximative description of different fusion reactors dynamics.

Our view on this is that, even though the MHD description might not be strictly valid in fusion plasmas, it will allow to capture some key-features. In particular in RFPs, where a large-scale bulk dynamics of the plasma is observed, MHD might be the only description which is at the same time precise enough to capture some of the physics and simple enough to disentangle the physical processes.

2.4 Magnetostatic equilibrium

Most of early plasma equilibrium studies were based on the ideal MHD model where the force balance is between the pressure gradient and the Lorentz force,

$$\nabla P = \boldsymbol{J} \times \boldsymbol{B}. \tag{2.31}$$

Multiple classes of equilibria derive from this equation, and correspond to different degrees of freedom. This is mainly a result of different geometrical configurations and symmetries.

The equilibrium described in equation (2.31) can be easily achieved in straight cylindrical geometries, like the z-pinch, rather than toroidal geometries where it requires the addition of new terms into the momentum equation [24, 25]. Indeed, in toroidal geometry, under some weak constraints on the shape of the magnetic field, it can be shown that the curl

of the Lorentz-force is non-zero [24]. Taking the curl of equation (2.31), and realizing that $\nabla \times (\nabla P) = 0$, this implies that the other terms of the evolution-equation for $\boldsymbol{u}$, equation (2.19) cannot be zero and a static equilibrium becomes impossible within the MHD description.

In the investigations carried out in this manuscript, this is no important issue since all our simulations take into account the full dynamics of the system. However, since a large body of fusion research is based on static equilibria, we will discuss them in the following paragraphs, ignoring thereby the theoretical problem that concerns their existence in toroidal geometry.

2.4.1 One-dimensional equilibrium

One-dimensional configurations are used to disentangle different force balances, like axial and poloidal forces balance and radial pressure balance, which is the main interest of this configuration. In the following, we show an example of a one-dimensional equilibrium in a circular cylinder.

Let's consider a cylindrical pinch with imposed axisymmetric axial and poloidal magnetic fields. The equilibrium quantities depend only on the radial coordinate r,

$$P(r), \qquad \boldsymbol{B} = (0, B_\theta(r), B_z(r)). \tag{2.32}$$

Applying the force balance equation (2.31) in this case leads to

$$\frac{dP}{dr} = J_\theta B_z - J_z B_\theta = -\frac{1}{2}\frac{d(B_z^2)}{dr} - \frac{B_\theta}{r}\frac{d(rB_\theta)}{dr}. \tag{2.33}$$

Multiplying both sides of (2.33) by r^2 then integrating by parts between $r = 0$ and $r = a$,

$$\int_0^a r^2 \frac{dP}{dr} dr = -\frac{1}{2}\int_0^a r^2 \frac{d(B_z^2)}{dr} dr - \int_0^a rB_\theta \frac{d(rB_\theta)}{dr} dr,$$

$$\Rightarrow -\int_0^a 2Prdr = -\frac{1}{2}a^2 B_z^2(a) + \frac{1}{2}\int_0^a 2rB_z^2 dr - \frac{1}{2}a^2 B_\theta^2(a), \tag{2.34}$$

and finally by denoting the integral over the plasma cross-section by $\langle ... \rangle = \frac{2}{a^2}\int_0^a ...rdr$, (2.34) yields,

$$\langle P \rangle = \frac{1}{2}[B_\theta^2(a) + B_z^2(a) - \langle B_z^2 \rangle]. \tag{2.35}$$

This result shows that the simplest possible equilibrium relates the pressure to the axial magnetic field and the value of the poloidal field at the wall.

A significant parameter in nuclear fusion is the plasma beta, which measures the ratio of the plasma pressure to magnetic pressure and is defined by,

$$\beta = 2\frac{\langle P \rangle}{\langle B^2 \rangle}. \tag{2.36}$$

This parameter is of major importance to measure the confinement quality (roughly given by P) as a function of the magnetic field. Our chapter 4 will be dedicated to the investigation of the role of β in RFP dynamics.

Another important parameter is the safety factor q, which quantifies the magnetic field line twist. It is defined in the one-dimensional case as,

$$q(r) = \frac{rB_z(r)}{RB_\theta(r)}, \tag{2.37}$$

where $R = L_z/2\pi$ is the equivalent of a torus major radius for a cylindrical pinch, and L_z the cylinder length. It is found that instabilities are more likely to develop when q is low. Therefore, in tokamaks where MHD instabilities are avoided, the value of q is in general high. In RFPs this value is lower, since they operate beyond the MHD instability threshold.

Magnetic field line twist is also quantified by the ratio of the averaged poloidal magnetic field at the wall $\overline{B_p}$ over the volume-averaged axial magnetic field $\langle B_z \rangle$, called pinch ratio Θ,

$$\Theta = \frac{\overline{B_p}}{\langle B_z \rangle}. \tag{2.38}$$

This parameter takes values smaller than unity in the case of tokamak regimes, and larger than unity in the RFP regimes' case. In the latter case, an additional parameter F is used to study the reversal near the wall. F is called the field reversal parameter and is defined as the ratio of the averaged axial magnetic field at the wall $\overline{B_z}$ over its volume-average value $\langle B_z \rangle$,

$$F = \frac{\overline{B_z}}{\langle B_z \rangle}. \tag{2.39}$$

Clearly, F takes negative values when reversal is observed in the RFP dynamics.

One-dimensional equilibrium equations have been used previously [26] to study the stability of tearing modes in cylindrical RFP configuration at zero β regime.

2.4.2 Two-dimensional equilibrium

The two-dimensional equilibrium is obtained by breaking a symmetry in the one-dimensional configuration. This can be done by shaping the poloidal cross-section, binding a cylinder into a torus, imposing non-uniform current density, etc. We will limit this paragraph to the case of toroidal axisymmetry and derive the equilibrium equations. We consider the geometry illustrated in figure 2.3 , where R, ϕ and z are the cylindrical coordinates. Since $\boldsymbol{B}$ is solenoidal and toroidally axisymmetric ($\partial/\partial\phi = 0$) is assumed, its poloidal component, $\boldsymbol{B}_p = B_R\boldsymbol{e}_R + B_z\boldsymbol{e}_z$, derives from a toroidal potential A_ϕ and can be written as,

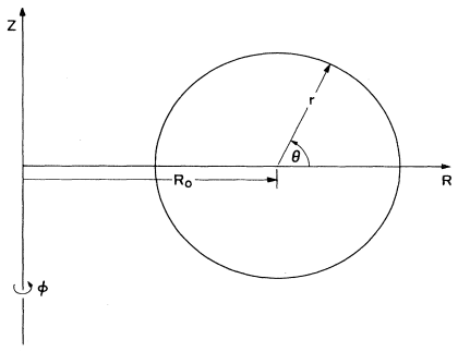

Figure 2.3: Sketch of the toroidal coordinates.

$$B_R = -\frac{\partial A_\phi}{\partial z} = -\frac{1}{R}\frac{\partial (RA_\phi)}{\partial z} = -\frac{1}{R}\frac{\partial \psi}{\partial z}, \tag{2.40}$$

$$B_z = \frac{1}{R}\frac{\partial (RA_\phi)}{\partial R} = \frac{1}{R}\frac{\partial \psi}{\partial R}, \tag{2.41}$$

where $\psi = RA_\phi$ is called the flux function which is introduced for analytical convenience. The current density is calculated by applying Ampere's law (2.14),

$$J_R = -\frac{\partial B_\phi}{\partial z}, \tag{2.42}$$

$$J_\phi = -\frac{\partial}{\partial R}\left(\frac{1}{R}\frac{\partial \psi}{\partial R}\right) - \frac{1}{R}\frac{\partial^2 \psi}{\partial z^2} \equiv -\frac{1}{R}\Delta^*\psi, \tag{2.43}$$

$$J_z = \frac{1}{R}\frac{\partial (RB_\phi)}{\partial R}. \tag{2.44}$$

Replacing these expressions in the equilibrium equation (2.31) yields,

$$\frac{\partial P}{\partial R} = -\frac{1}{R^2}\frac{\partial \psi}{\partial R}\Delta^*\psi - \frac{B_\phi}{R}\frac{\partial (RB_\phi)}{\partial R}, \tag{2.45}$$

$$0 = \frac{1}{R}\frac{\partial B_\phi}{\partial z}\frac{\partial \psi}{\partial R} - \frac{1}{R^2}\frac{\partial (RB_\phi)}{\partial R}\frac{\partial \psi}{\partial z}, \tag{2.46}$$

$$\frac{\partial P}{\partial z} = -\frac{1}{R^2}\frac{\partial \psi}{\partial z}\Delta^*\psi - B_\phi\frac{\partial B_\phi}{\partial z}. \tag{2.47}$$

Equation (2.46) can be rewritten as $\nabla\psi \times \nabla(RB_\phi) = 0$, which means that $F = RB_\phi$ is constant over a constant flux surface ψ, and hence $F = F(\psi)$. Similarly, multiplying equation (2.45) by $\partial\psi/\partial z$ and (2.47) by $\partial\psi/\partial R$ and combining them, leads to

$$\frac{\partial P}{\partial R}\frac{\partial \psi}{\partial z} - \frac{\partial P}{\partial z}\frac{\partial \psi}{\partial R} = 0. \tag{2.48}$$

This also can be rewritten as $\nabla P \times \nabla\psi = 0$, and thus $P = P(\psi)$. Finally, substituting $F(\psi)$ and $P(\psi)$ in (2.45) or (2.47) leads to the **Grad-Shafranov** equation,

$$\boxed{R^2\frac{\partial P}{\partial \psi} + F\frac{\partial F}{\partial \psi} + \Delta^*\psi = 0.} \tag{2.49}$$

This nonlinear equation describes toroidal equilibria. The choice of the two free functions $P(\psi)$ and $F(\psi)$, as well as the boundary conditions, determines the nature of the equilibria whether it is a tokamak configuration, RFP, etc. The Grad-Shafranov equation is usually solved numerically because of its nonlinear nature. Nevertheless, some analytical solutions are proposed under the constraint of simplifying assumptions and symmetries, like Solov'ev's solution [27] based on the assumption of the independence of the first two terms of equation (2.49) of ψ.

2.5 The classical RFP paradigm: Taylor's relaxation theory

An important theory deriving from ideal MHD is Taylor's relaxation theory of RFPs, which was developed to understand the reversal phenomenon observed in the ZETA experiment.

In this theory, the RFP plasma is considered as an ideal conductor surrounded by a perfectly conducting shell. Let a be the vessel's minor radius and R the major radius. Once the discharge is generated by inducing a strong toroidal current, the plasma is driven into a turbulent state. Due to dissipative interaction with the vessel wall, the plasma reaches a stable minimum energy state. The induction equation of this ideal case,

$$\frac{\partial \boldsymbol{B}}{\partial t} = \nabla \times (\boldsymbol{u} \times \boldsymbol{B}), \tag{2.50}$$

shows that the magnetic field lines are "frozen" into the plasma, so no breaking and reconnection of the field lines is allowed, hence the field line topology is conserved. In [28] it was proven that this field line topology conservation is equivalent to the conservation of magnetic helicity H. Indeed, in hydrodynamics, the "knottedness" of the vorticity field is also conserved in the absence of viscosity, which is represented by the conservation of

hydrodynamic helicity [29]. In practice, since the plasma is considered weakly dissipative, magnetic reconnection destroys most of the flux surfaces, and thus the field line topology is not conserved on every flux surface. The only flux surface where the identity is conserved is the one at the wall which is considered perfectly conducting. Therefore, the helicity over the total volume is conserved and not on individual flux surfaces. Applying the variational principle to calculate the minimum energy state subject to $H = constant$ yields,

$$\nabla \times \boldsymbol{B} = \mu \boldsymbol{B}, \tag{2.51}$$

so that,

$$\boldsymbol{B} \cdot \nabla \mu = 0, \tag{2.52}$$

where μ is a Lagrange multiplier. The solution of equation (2.51) corresponding to a minimum energy state in cylindrical coordinates, is either an $m = 0$ symmetric solutions,

$$\begin{aligned} B_r &= 0, \\ B_\theta &= B_0 J_1(\mu r), \\ B_z &= B_0 J_0(\mu r), \end{aligned} \tag{2.53}$$

or a superposition of $m = 0$ and $m = 1$ helical solution,

$$\begin{aligned} B_r &= -B_1 \left[\frac{k}{\alpha} J_1'(\alpha r) + \frac{\mu}{r\alpha^2} J_1(\alpha r) \right] \sin(\theta + kz) \qquad \text{with } \alpha = \sqrt{\mu^2 - k^2}, \\ B_\theta &= B_0 J_1(\mu r) - B_1 \left[\frac{\mu}{\alpha} J_1'(\alpha r) + \frac{k}{r\alpha^2} J_1(\alpha r) \right] \cos(\theta + kz), \\ B_z &= B_0 J_0(\mu r) + B_1 J_1(\alpha r) \cos(\theta + kz), \end{aligned} \tag{2.54}$$

where m is the poloidal mode number, J_0 and J_1 the zeroth and first order Bessel functions, B_0 the initial imposed toroidal magnetic field in the RFP, and B_1 the helical amplitude determined by the boundary condition $B_r(a) = 0$, given values of H and the toroidal magnetic flux ψ_t.

In order to verify this theory, two measurable parameters are calculated, the pinch ratio Θ and the field reversal F. These parameters are calculated in the symmetric case as follows,

$$\Theta = \frac{\overline{B_p}(a)}{\langle B_z \rangle} = \frac{B_\theta(a)}{V^{-1} \int_0^a B_z dV} = \frac{B_0 J_1(\mu r)}{(2\pi^2 a^2 R)^{-1} \int_0^a 2\pi R B_0 J_0(\mu r) r dr} = \frac{\mu a}{2}, \tag{2.55}$$

$$F = \frac{\overline{B_z}(a)}{\langle B_z \rangle} = \frac{B_z(a)}{V^{-1} \int_0^a B_z dV} = \frac{B_0 J_1(\mu r)}{(2\pi^2 a^2 R)^{-1} \int_0^a 2\pi R B_0 J_0(\mu r) r dr} = \frac{\mu a J_0(\mu a)}{2 J_1(\mu a)}, \tag{2.56}$$

where V is the plasma volume. It was found that for $\Theta < 1.56$ the minimum energy corresponds to the axisymmetric solution and for $\Theta > 1.56$ to the helical solution. Furthermore, reversal is estimated to take place for $\Theta > 1.24$.

Taylor's relaxation theory was generalized later by Reiman [30] to take into consideration toroidal geometries and different cross-sections, and it was found that the F-Θ curve stays unchanged for elliptical cross-section. Experimentally, Taylor's theory presents qualitatively good agreement with results obtained by DiMarco in 1983 and shown in Figure 2.4, however the experimental field reversal occurs for values of Θ greater than the predicted ones.

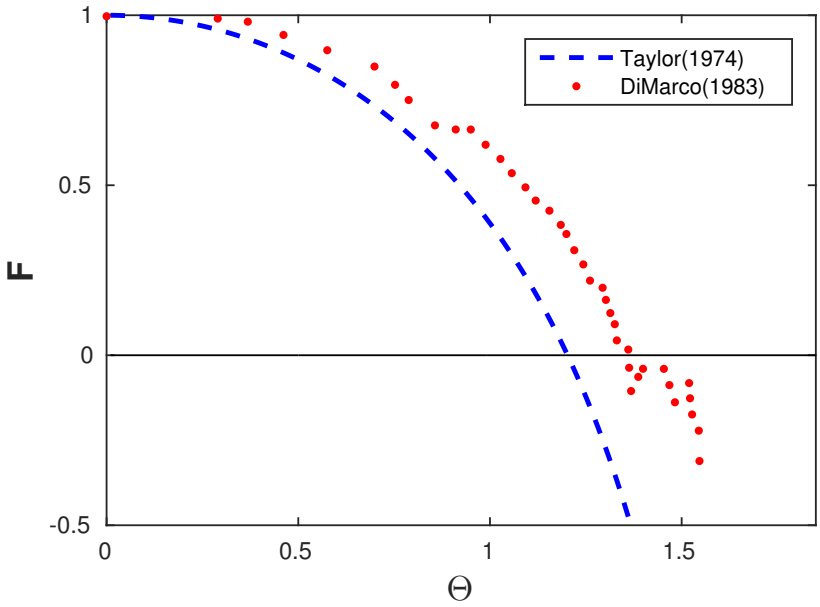

Figure 2.4: Experimental (red dots) and theoretical [6] (blue dashed) F-Θ curves.

Due to limited computational power back then, Taylor's relaxation theory couldn't be verified via direct numerical simulations, and therefore the RFP conserved its classical image as a bad candidate to succeed nuclear fusion due to magnetic chaos and strong wall interaction. In 2000, a quiescent helical structure present in the plasma core which was previously unnoticed in experimental results, came to light and changed the whole RFP picture. The new paradigm is presented in the following section.

2.6 "RFP gets self-organized": the new paradigm

2.6.1 Quasi-Single-Helicity states

With the growth of computational power in the 1990s, multiple MHD simulations have been carried out to study the RFP dynamics. It was found in references [31–33] that without any forced helicity in the flow, a bifurcation leads to an almost regular helical deformation of the plasma and a decrease in the magnetic chaos. This pure helix has one single toroidal mode $n = n_0$, whence the name Single Helicity (SH) state. This helical structure is observed in the laminar regime, when the viscosity and resistivity are large enough. More precisely a small value of the Hartmann number $Ha \sim (\nu\eta)^{-1/2}$ is needed to observe a SH state [34]. When dissipation decreases (Ha increases), the pure helix becomes more free to bend axially, and smaller helical structures detach from it. This corresponds to a Quasi-Single-Helicity (QSH) state, where secondary helicities appear with lower energy than the orginal one, but most of the energy is still contained in the principal helical structure. If the dissipation continues to decrease, the large helical structure will end up forming several helices with different modes n, which correspond to a Multiple Helicity (MH) state.

These numerical results motivated the RFX team to revisit their experimental database. In 2000, the team discovered shots with long lasting QSH states [7], where they lasted for several ms in the transient phase and for the whole pulse length in the stationary phase. Furthermore, a "bean" shaped magnetic island with dominant helicity was detected in the core of the plasma, and a strong temperature gradient was found at its edge. This island presented an electron internal transport barrier (eITB), i.e. a region where due to strong velocity gradients the radial electron flux was reduced. QSH states were detected as well later in other RFPs, like MST in 2002 [35], TPE-RX in 2004 [36] and in EXTRAP T2R in 2007 [37]. Thereby the hope revived that, if an RFP can be kept into this QSH state by control strategies or other means, fusion can be achieved in RFPs. In particular its relatively cheap magnetic design would make the RFP then a very competitive MCF reactor.

2.6.2 Single Helical axis topology

Another bifurcation found in MHD simulations [38] when the amplitude of the SH mode is low enough, is the existence of two magnetic axes, hence the topology is named Double Axis (DAx) state. One axis corresponds to the unperturbed axisymmetric magnetic field (point O in Figure 2.5 (a)), and the other to the magnetic island (point O' in Figure 2.5 (a)). When the amplitude of the SH mode increases, the magnetic island is suppressed due to collision of the island X-point with the unperturbed axis, thus leading to a topology

with a single helical axis (SHAx) corresponding to the former island O'-point as shown in Figure 2.5 (b). Moreover, the new topology, QSH states of the SHAx types, is much more resilient to magnetic chaos than the former topology where an island appeared in the QSH states. With magnetic chaos we indicate that the magnetic field lines move in time in an unpredictable manner.

The DAx topology was first observed experimentally [39] in QSH states where the secondary modes had non-negligible amplitude. In later experiments [14], an increase of toroidal current to an order of 1.4 MA in the upgraded RFX-mod vessel led to the observation of the SHAx topology predicted by the previous MHD simulations [38]. It was found that the confinement time had increased by a factor of four due to the formation of a transport barrier related to the flux surfaces of the dominant helical mode, and the electrons inside reached a temperature greater than 1 keV.

2.7 Classical vs. new paradigm

The results above show the great progress made in understanding the dynamics of RFP and its evolution since Taylor's relaxation theory. The discovery of QSH states was the first step towards a new paradigm where the RFP shows organized dynamics under one

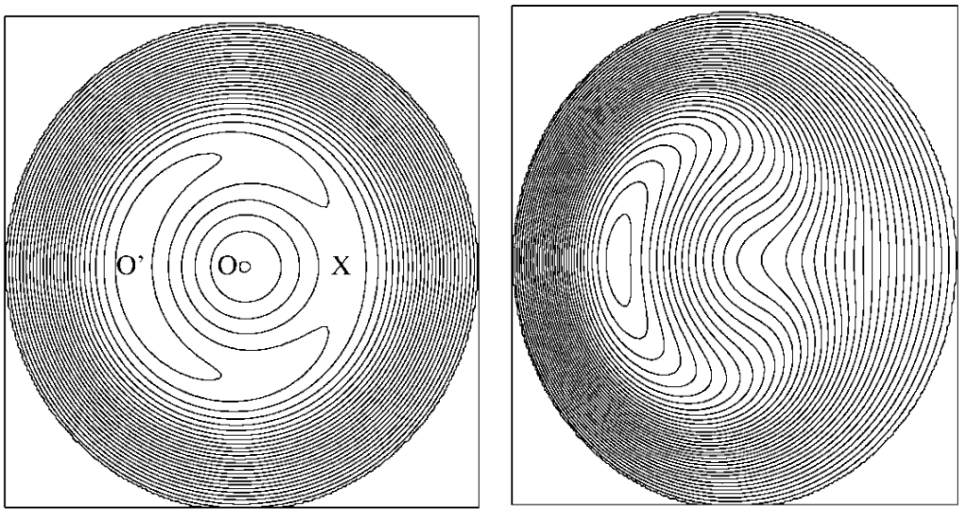

(a) (b)

Figure 2.5: Magnetic flux surfaces of: (a) DAx topology , (b) SHAx topology. (Taken from [38])

dominant helicity regime, leading to large reduction of magnetic chaos and improvement of confinement. One step further in understanding the self-organization of RFP was the prediction of suppression of the magnetic island detected in the QSH states where the magnetic topology changes from DAx to SHAx. This step was achieved experimentally in high current regimes (greater than 1 MA), during which the confinement time and quality increased by a factor of four. This new RFP paradigm based on the two main components, QSH states and SHAx topology, proves that RFP physics moved away from the Taylor picture, which essentially consisted of a chaotic RFP description.

This new picture of a well organized RFP plasma with reduced magnetic chaos is in contrast with the classical Taylor theory for several reasons. First, the walls are considered ideal conductor in the classical theory based on the assumption that edge resistivity prevents magnetic field reversal. This is inconsistent with later studies [33] where it is shown that field reversal is more efficient in a resistive edge configuration. Furthermore, considering the parallel Ohm's law at the edge shows that larger edge resistivity implies a larger electrostatic field, and therefore larger electrostatic drift that enhances the dynamo action to conserve the reversed configuration [40]. Another issue in the classical theory is the reversed axisymmetric magnetic profile corresponding to the range $1.2 < \Theta < 1.56$. This result is inconsistent with Cowling's theorem which mentions that no axisymmetric dynamo can conserve a symmetric magnetic field. Furthermore, adopting Taylor's reasoning by considering zero pressure gradient, yields the result that the current density and the magnetic field are parallel, reverse signs together, and thus become null together. Analytically, this means that the minimum value the magnetic field can reach, when its curl, the current density, equals zero, is zero. Therefore, no reversal can be reached in this configuration. Finally, the fluctuations acting in Taylor's relaxation are predicted to be small scale corresponding to line reconnection brought by a small scale Alfven wave motion [41]. Experiments and MHD simulations show that they are large scale corresponding to tearing modes. Further arguments showing the inconsistency of Taylor's theory are given in [42], where the consideration of relaxation toward a minimum energy state is criticized by invoking the tendency of an open Ohmic system with fixed currents to maximize its magnetic energy.

Even though, clearly, progress has been made in understanding RFPs, its understanding in terms of how the plasma reacts on a change of the control parameters remains quite incomplete. Therefore further research based on simple plasma descriptions such as MHD seem primordial if the RFP is to be taken to the level of confinement of tokamaks. The rest of this manuscript aims at enhancing this understanding.

Chapter 3

Numerical methods

Numerical simulations are a powerful tool to understand and predict the dynamics of complex flows. In the case of hydrodynamics, direct numerical simulations of the Navier-Stokes equations are nowadays even considered numerical experiments, almost on equal footing with actual experiments. This is not completely so for plasmas, where the complexity of the description impedes a complete and precise simulation of all the details of the flow on the scale of an actual fusion reactor. Nevertheless even at the coarse level of the MHD description numerical simulations can explain some of the important physical mechanisms which determine the confinement of a plasma. For instance, such simulations were used by Escande *et al.* [38] to predict the suppression of magnetic islands in DAx states leading to a SHAx state. This result was proved experimentally nine years later in the RFX-mod high current regime experiments [14]. Numerical simulations are thus a key element of the conception of experimental reactors.

We present in this chapter the numerical methods used to discretize in space and time the MHD equations introduced previously in Chapter 2, and we show how we impose a cylindrical geometry.

3.1 MHD equations

In the present work, we consider a plasma characterized by constant and uniform permeability μ, permittivity ϵ, conductivity σ and density $\rho = 1$. The more complicated case of non-uniform conductivity using the same numerical methods was considered in reference [43]. In the magnetohydrodynamic (MHD) description that we consider, the governing equations are the incompressible Navier-Stokes equations including the Lorentz force (2.15), and the induction equation (2.18). Normalizing these quantities by the Alfvén ve-

locity $C_A = B_0/\sqrt{\rho\mu}$, a reference magnetic field B_0 and a conveniently chosen length scale $\mathcal{L}$, and expanding the nonlinear term in equation (2.15) leads to the following expressions,

$$\frac{\partial \boldsymbol{u}}{\partial t} = -\nabla \Pi + \boldsymbol{u} \times \boldsymbol{\omega} + \boldsymbol{J} \times \boldsymbol{B} + \nu \nabla^2 \boldsymbol{u}, \tag{3.1}$$

and

$$\frac{\partial \boldsymbol{B}}{\partial t} = \nabla \times (\boldsymbol{u} \times \boldsymbol{B}) + \lambda \nabla^2 \boldsymbol{B}, \tag{3.2}$$

where $\Pi = P + \boldsymbol{u}^2/2$ is the modified pressure. The current density is given by

$$\boldsymbol{J} = \boldsymbol{\nabla} \times \boldsymbol{B}. \tag{3.3}$$

The velocity field $\boldsymbol{u}$ and the magnetic field $\boldsymbol{B}$ are both divergence free,

$$\boldsymbol{\nabla} \cdot \boldsymbol{u} = 0, \tag{3.4}$$

$$\boldsymbol{\nabla} \cdot \boldsymbol{B} = 0. \tag{3.5}$$

In Chapter 5, in order to measure the influence of the geometry on the confinement, we will consider the advection of a passive scalar T. We thereto solve the following equation simultanuously with equations (3.1) and (3.2),

$$\frac{\partial T}{\partial t} + \boldsymbol{u} \cdot \nabla T = \alpha \nabla^2 T, \tag{3.6}$$

where α is the scalar diffusivity, chosen equal $\alpha = 10\lambda$.

3.2 Pseudo-spectral discretization and determination of the pressure

Equations (3.1) and (3.2) are solved using a pseudo-spectral method in a periodic domain of size $N_x \times N_y \times N_z$ grid points. Spatial derivatives are evaluated in Fourier space and multiplications are computed in physical space. In the following, all Fourier transforms of different fields are denoted by the symbol $\widehat{\ }$or $\mathcal{F}\{\}$. These transforms consist in representing the fields as truncated Fourier series like in the following example of the velocity field,

$$\boldsymbol{u}(\boldsymbol{x}, t) = \sum_{k_x=-N_x/2}^{N_x/2-1} \sum_{k_y=-N_y/2}^{N_y/2-1} \sum_{k_z=-N_z/2}^{N_z/2-1} \widehat{\boldsymbol{u}}(\boldsymbol{k}, t) e^{i\boldsymbol{k}\cdot\boldsymbol{x}}, \tag{3.7}$$

$$\widehat{\boldsymbol{u}}(\boldsymbol{k}, t) = \frac{(8\pi^3)^{-1}}{N_x N_y N_z} \sum_{n_x=0}^{N_x-1} \sum_{n_y=0}^{N_y-1} \sum_{n_z=0}^{N_z-1} \boldsymbol{u}(\boldsymbol{x}, t) e^{-i\boldsymbol{k}\cdot\boldsymbol{x}}, \tag{3.8}$$

where $\boldsymbol{k} = (k_x, k_y, k_z)$ is the wave vector and $\boldsymbol{x} = (n_x L_x/N_x, n_y L_y/N_y, n_z L_z/N_z)$ the position vector. To avoid aliasing errors which consist of the production of small scales due to nonlinear terms which are not resolved on the grid, the velocity and magnetic fields are dealiased at each time step by truncating its Fourier coefficients using the 2/3 rule [44].

Using the incompressibility condition of the fluid, the pressure term can be eliminated by solving a Poisson equation obtained from taking divergence of the momentum equation. This can be written as follows,

$$\nabla^2\Big(P + \frac{u^2}{2}\Big) = \nabla \cdot \Big(\boldsymbol{u} \times \boldsymbol{\omega} + \boldsymbol{J} \times \boldsymbol{B} + \nu\nabla^2\boldsymbol{u}\Big). \tag{3.9}$$

The viscous term can be eliminated by using the following vector identity,

$$\nabla \cdot (\nabla^2\boldsymbol{u}) = \nabla^2(\nabla \cdot \boldsymbol{u}) = 0. \tag{3.10}$$

Equation (3.9) can be written in spectral space as,

$$-k^2\mathcal{F}\{P + \frac{u^2}{2}\} = i\boldsymbol{k} \cdot \Big\{\widehat{\boldsymbol{u} \times \boldsymbol{\omega}} + \widehat{\boldsymbol{J} \times \boldsymbol{B}}\Big\} \tag{3.11}$$

where the no-slip condition is considered ($\boldsymbol{u}_{wall} = 0$). The pressure can therefore be obtained by dividing by k^2 and applying an inverse Fourier transform,

$$P = \mathcal{F}^{-1}\left\{ -\frac{i\boldsymbol{k}}{k^2} \cdot \Big\{\widehat{\boldsymbol{u} \times \boldsymbol{\omega}} + \widehat{\boldsymbol{J} \times \boldsymbol{B}}\Big\}\right\} - \frac{u^2}{2}. \tag{3.12}$$

However, this does not yield the exact pressure field since the numerical integration constant is included in the resulting field. Thus, one last step needed is to substract the pressure value in the solid region from the resulting field.

The resolution of the previous Poisson equation introduces the Riesz projector $P_{ij} = \delta_{ij} - k_i k_j/\boldsymbol{k}^2$ in front of the nonlinear term and therefore yields equations (3.1),(3.2) and (3.6) in spectral space,

$$\frac{\partial\widehat{u}_i}{\partial t} = P_{ij}\Big\{(\widehat{\boldsymbol{J} \times \boldsymbol{B}} + \widehat{\boldsymbol{u} \times \boldsymbol{\omega}})_j\Big\} - \nu k^2\hat{u}_i, \tag{3.13}$$

$$\frac{\partial\widehat{B}_i}{\partial t} = \Big[i\boldsymbol{k} \times (\widehat{\boldsymbol{u} \times \boldsymbol{B}})\Big]_i - \lambda k^2\hat{B}_i, \tag{3.14}$$

and

$$\frac{\partial\widehat{T}}{\partial t} + \widehat{\boldsymbol{u} \cdot \nabla T} = -\alpha k^2\widehat{T}. \tag{3.15}$$

The Fourier transform is implemented in the code using the JMFFT library which has an order of complexity of $N \log_2 N$ with $N = N_x N_y N_z$. The pseudo-spectral method is a very efficient and precise method, as soon as the number of grid points becomes large. Indeed spectral methods of nonlinear equation need the resolution of convolution products of complexity N^3, which are far more expensive than the Fast Fourier Transfroms (FFT) for large value of N. The FFTs allow these convolution products to be reduced in physical space where their evaluations consist in a simple product.

3.3 Penalization method

The cylindrical geometry is built using the volume penalization method which consists in considering the solid boundary as a porous medium with a negligible permeability. The flow is considered in a domain composed of two subdomains with different permeabilities: fluid domain Ω_f and solid domain Ω_s. Numerically, this method introduces new term in the MHD and advection-diffusion equations as follows,

$$\frac{\partial \boldsymbol{u}}{\partial t} = -\nabla \Pi + \boldsymbol{u} \times \boldsymbol{\omega} + j \times \boldsymbol{B} + \nu \nabla^2 \boldsymbol{u} - \underbrace{\frac{\chi}{\eta}(\boldsymbol{u} - \boldsymbol{u}_{wall})}_{penalization\ term}, \tag{3.16}$$

$$\frac{\partial \boldsymbol{B}}{\partial t} = \nabla \times (\boldsymbol{u} \times \boldsymbol{B}) + \lambda \nabla^2 \boldsymbol{B} - \underbrace{\frac{\chi}{\eta}(\boldsymbol{B} - \boldsymbol{B}_{wall})}_{penalization\ term}, \tag{3.17}$$

and

$$\frac{\partial T}{\partial t} + \boldsymbol{u} \cdot \nabla T = \alpha \nabla^2 T - \underbrace{\frac{\chi}{\eta}(T - T_{wall})}_{penalization\ term}, \tag{3.18}$$

with $\boldsymbol{u}_{wall}$, $\boldsymbol{B}_{wall}$ and T_{wall} the imposed values of the velocity, the magnetic, and the scalar field in the solid domain, η the solid domain permeability and χ the mask function that can take arbitrary shape:

$$\begin{cases} \chi = 0 & \text{in the fluid domain } \Omega_f \\ \chi = 1 & \text{in the solid domain } \Omega_s. \end{cases}$$

In order to implement this method in the pseudo-spectral solver, a Fourier transform is applied to equations (3.16) and (3.17). The velocity equation in spectral space becomes,

$$\frac{\partial \widehat{u}_i}{\partial t} = P_{ij} \left\{ \left[\widehat{\boldsymbol{J} \times \boldsymbol{B}} + \widehat{\boldsymbol{u} \times \boldsymbol{\omega}} - \mathcal{F}\Big\{ \frac{\chi}{\eta}(\boldsymbol{u} - \boldsymbol{u}_{wall}) \Big\} \right]_j \right\} - \nu k^2 \hat{u}_i, \tag{3.19}$$

where the Riesz projector P_{ij} is also applied to the penalization term to ensure incompressibility, since this term is not necessarily divergence free. Similarly, the magnetic field is no longer solenoidal, only due to the penalization term. This is solved by adding a new term to equation (3.16) that restores solenoidality. In analogy with the penalized velocity equation, this term can be simply an auxiliary pressure gradient, and therefore leads to the following induction equation in spectral space,

$$\frac{\partial \widehat{B}_i}{\partial t} = P_{ij}\left\{\left[i\boldsymbol{k}\times(\widehat{\boldsymbol{u}\times\boldsymbol{B}}) - \mathcal{F}\Big\{\frac{\chi}{\eta}(\boldsymbol{B}-\boldsymbol{B}_{wall})\Big\}\right]_j\right\} - \lambda k^2 \hat{B}_i. \tag{3.20}$$

The main advantage of the penalization method is its simplicity which allows the implementation of complex geometries by just modifying the mask function χ. However, this method comes with several limitations. First, the penalized MHD equations are solved in the fluid and solid domains, therefore computational resources are partially wasted on computing the flow inside the walls. Such losses become important when the solid domain is large like in the case of Taylor-Couette flow. Another limitation of the penalization method is the high resolution needed to study the boundary small scale dynamics since no mesh refinement is available near the wall. Finally, the discontinuities in the different fields and their gradients generate Gibbs oscillations. These oscillations do not constitute a serious problem in most cases unless the discontinuity becomes large, thus increasing the oscillations size. To solve this problem, Hermite's polynomial interpolation is computed at the boundary to impose in a smooth way the continuity of the field profile and its derivative between the boundary value and zero. A last disadvantage is the loss of spectral precision. In the directions perpendicular to the wall, the method becomes second-order precise in space-discretization. Detailed description and validation of the volume penalization method can be found in [45], and an application of the method to investigate RFPs in toroidal domains is reported in previous work [43, 46]

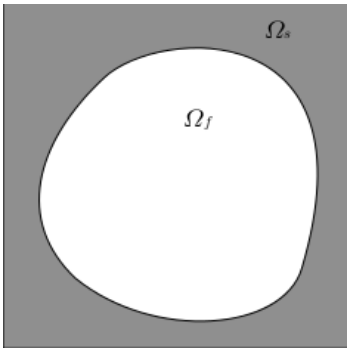

Figure 3.1: Fluid domain Ω_f in white and solid domain Ω_s in grey.

The penalization method has thus several drawbacks. Nevertheless, the flexibility of the mask-function allowing a rapid change of geometry and the existence of the highly efficient machinery for pseudo-spectral simulations make the penalization method combined with a pseudo-spectral solver an attractive alternative to geometry-adapted meshing, in particular when the goal of an investigation is to measure the influence of the shape of a domain on the flow-dynamics.

3.4 Time discretization

A semi-implicit third order time-advancing scheme of Adams-Bashforth type is used to solve the MHD equations. It consists in an exact integration of the dissipative and magnetic diffusion terms and explicit discretization of the remaining terms except the penalization term which is evaluated implicitly at instant t_n+1, whence the name *semi-implicit* [45,47]. Indeed, the time step size Δt is determined by the common CFL condition,

$$\Delta t_{n+1} = C\Delta x/U_{max}, \tag{3.21}$$

where $C<1$ is the CFL constant, Δx is the smallest spatial grid size and U_{max} the largest velocity values among the three components. It has been proven that for sufficiently small value of the penalization parameter η, the time step Δt replaces η [45,48]. In the following, we will present the time scheme only for the velocity field $\boldsymbol{u}$, since it is similar for the magnetic field $\boldsymbol{B}$.

First, equation (3.1) is rewritten in the form of a nonlinear evolution equation and then transformed into spectral space,

$$\partial_t \boldsymbol{u} - \nu\nabla^2\boldsymbol{u} = N(\boldsymbol{u}), \tag{3.22}$$

$$\partial_t \widehat{\boldsymbol{u}} + \nu k^2 \widehat{\boldsymbol{u}} = \widehat{N}(\widehat{\boldsymbol{u}}). \tag{3.23}$$

Applying the following variable change $\widehat{\boldsymbol{u}}(\boldsymbol{k},t_n) \rightarrow \widehat{\boldsymbol{u}}(\boldsymbol{k},t)e^{-\nu k^2 t}$ and considering an initial condition $\widehat{\boldsymbol{u}}(\boldsymbol{k},t_n)$ yield the following solution for the equation above,

$$\widehat{\boldsymbol{u}}(\boldsymbol{k},t_{n+1}) = e^{-\nu k^2 \Delta t_{n+1}}\widehat{\boldsymbol{u}}(\boldsymbol{k},t) + \int_{t_n}^{t_{n+1}} e^{-k^2\nu(t_{n+1}-s)}\widehat{N}(\widehat{\boldsymbol{u}}(\boldsymbol{k},s))ds. \tag{3.24}$$

This solution can be discretized using Adams-Bashforth second order (AB2) as,

$$\widehat{\boldsymbol{u}}(\boldsymbol{k},t_{n+1}) = e^{-\nu k^2 \Delta t_{n+1}}\left(\widehat{\boldsymbol{u}}(\boldsymbol{k},t_n) + \beta_{10}\widehat{N}^n + \beta_{11}e^{-\nu k^2\Delta t_n}\widehat{N}^{n-1}\right), \tag{3.25}$$

and Adams-Bashforth third order (AB3) as,

$$\widehat{\boldsymbol{u}}(\boldsymbol{k}, t_{n+1}) = e^{-\nu k^2 \Delta t_{n+1}} \left(\widehat{\boldsymbol{u}}(\boldsymbol{k}, t_n) + \beta_{20} \widehat{N}^n + e^{-\nu k^2 \Delta t_n} \left(\beta_{21} \widehat{N}^{n-1} + \beta_{22} e^{-\nu k^2 \Delta t_{n-1}} \widehat{N}^{n-2} \right) \right), \tag{3.26}$$

where $\widehat{N}^n$ is the nonlinear term of equation (3.23) at instant t_n, $\Delta t_n = t_n - t_{n-1}$ and β_{ij} the Adams-Bashforth's coefficients which are defined as follows,

$$\begin{aligned}
\beta_{10} &= \frac{\Delta t_{n+1}}{2\Delta t_n}(\Delta t_{n+1} + 2\Delta t_n), \\
\beta_{11} &= -\frac{\Delta t_{n+1}^2}{2\Delta t_n}, \\
\beta_{20} &= \frac{\Delta t_{n+1}(2\Delta t_{n+1}^2 + 6\Delta t_n \Delta t_{n+1} + 3\Delta t_{n-1}\Delta t_{n+1} + 6\Delta t_n^2 + 6\Delta t_{n-1}\Delta t_n)}{6\Delta t_n(\Delta t_n + \Delta t_{n-1})}, \\
\beta_{21} &= \frac{-\Delta t_{n+1}^2(2\Delta t_{n+1} + 3\Delta t_n + 3\Delta t_{n-1})}{6\Delta t_{n-1}\Delta t_n}, \\
\beta_{22} &= \frac{\Delta t_{n+1}^2(2\Delta t_{n+1} + 3\Delta t_n)}{6\Delta t_{n-1}(\Delta t_n + \Delta t_{n-1})}.
\end{aligned} \tag{3.27}$$

Finally, the penalization term is evaluated at instant t_{n+1} as the following,

$$\widehat{u_i}(\boldsymbol{k}, t_{n+1}) = P_{ij} \left\{ \mathcal{F} \left[\frac{\mathcal{F}^{-1}\{Q_i^n\} + \frac{\Delta t}{\eta} \chi u_{wall_i}(\boldsymbol{x}, t_{n+1})}{1 + \frac{\Delta t}{\eta}\chi} \right]_j \right\}, \tag{3.28}$$

where Q_i^n is equivalent to equation (3.26), the last step of Adams-Bashforth third order scheme,

$$Q_i^n = e^{-\nu k^2 \Delta t_{n+1}} \left(\widehat{\boldsymbol{u}}(\boldsymbol{k}, t_n) + \beta_{20} \widehat{N}^n + e^{-\nu k^2 \Delta t_n} \left(\beta_{21} \widehat{N}^{n-1} + \beta_{22} e^{-\nu k^2 \Delta t_{n-1}} \widehat{N}^{n-2} \right) \right). \tag{3.29}$$

The advection-diffusion equation of the scalar is resolved using the explicit form of this time-scheme, where the penalization term is explicitly added to the nonlinear term instead of being evaluated at instant t_{n+1} as in (3.28).

3.5 Boundary conditions

Initially, in the plasma a uniform current density J_0 in the z-direction and an axial magnetic field B_{z0} are imposed, resulting in a helically shaped magnetic field. The current density J_0 will induce an elliptical magnetic field B_{p0} parallel to the elliptic boundaries. At later times the magnetic field will reorganize through an interplay with the velocity field, and

the total magnetic field will then consist of B_{z0} and B_{p0} plus the self-induced contributions. At the boundaries the velocity is imposed to be zero and the magnetic field is parallel to the boundaries. The value of the poloidal parallel magnetic field at the boundary is fixed and its value is determined by J_0. The expression of B_{p0} in cylindrical coordinates reads,

$$B_r = -\frac{1}{2} J_0 r c \sin(2\theta) \tag{3.30}$$

$$B_\theta = \frac{1}{2} J_0 r (1 - c\cos(2\theta)) \tag{3.31}$$

with c the ellipticity which can be expressed as a function of the ellipse's major semi-axis a and minor semi-axis b, i.e,

$$c = \frac{a^2 - b^2}{a^2 + b^2}. \tag{3.32}$$

Note that the coordinates we use are cylindrical and not elliptical coordinates so that only in the case of the circle the radial vector $\boldsymbol{e}_r$ is everywhere perpendicular to the boundary. A study of the influence of the chosen boundary conditions is reported in section 6.3.4.

Equations (3.1) and (3.2) are solved in a periodic domain of size $\pi \times \pi \times 8\pi$ with $64 \times 64 \times 512$ grid points. The aspect ratio of the physical domain containing the plasma is $L_z/2\pi b = 4$.

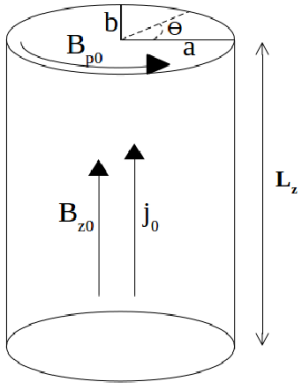

Figure 3.2: Sketch of the cylindrical geometry and imposed magnetic field and current density.

Chapter 4

On the role and value of β in MHD simulations

The parameter β, defined as the ratio of the pressure to the square of the magnetic field, is widely used to characterize astrophysical and fusion plasmas. The same quantity further plays a key-role in determining the magnetostatic equilibria of toroidally confined plasmas. However, in the dynamics it is the pressure gradient which is important rather than the value of the pressure itself. It is shown here that the value of β is not an adequate parameter to measure the importance of the pressure in the dynamics. An alternative quantity is proposed and its scaling is investigated using incompressible magnetohydrodynamic simulations in a periodic cylinder in the Reversed Field Pinch flow regime.

4.1 Introduction

In conducting fluids and plasmas, the force-balance on a fluid element contains, in addition to the pressure-gradient, also a magnetic pressure gradient. The ratio of the hydrodynamic to magnetic pressure is in general quantified by the parameter β,

$$\beta = 2\frac{P}{B^2}, \tag{4.1}$$

where we have used Alfvénic units to normalize the plasma pressure and magnetic field. The precise role of β and its definition depend on the field of application. For instance in astrophysical applications, the value of β is used to characterize the plasma which is considered. Typically, low values of β are observed in the solar wind, e.g. $\beta \ll 1$ in the mid-corona [49]. In the remainder of this investigation we will focus on the use of β in

the magnetically confined fusion community, but the results and ideas are, we think, of broader relevance.

In magnetic fusion devices such as tokamaks or Reversed Field Pinches (RFPs), obtaining a high pressure in the center of the plasma is one of the indicators of good confinement. Indeed, the challenge is to confine a plasma as well as possible for a given magnetic field. A very rough measure of the reactor's efficiency can then be defined by the pressure in the plasma (which indicates how high the temperature is), compared to the imposed magnetic field, in other words, by the value of β. One particular definition of β, $\overline{\beta}$, is defined here as

$$\overline{\beta} = 2\frac{\langle P \rangle}{\langle B^2 \rangle}, \tag{4.2}$$

where the brackets indicate a volume average over the plasma volume of interest. Other definitions are also used [50] based on the value of $\boldsymbol{B}$ at the wall of the plasma for instance. The quantity β is thus a key parameter in fusion design and operation, and further plays an important role in investigations of the stability of confined plasmas [51] and the dynamics of magnetic islands in tokamaks [52].

In many fusion related flows the value of β is low, of the order of a few percent or even less, and as such, the effects of pressure are therefore sometimes neglected. This approximation was for instance used in investigations of the single-helicity states in the RFX reactor [34, 38], and in studies on helical modulation of the magnetic field at the boundary of the plasma [53, 54] and on sawtooth mitigation [55]. Also in the prediction of the relaxed Taylor-state [41], the influence of β was considered negligible. These are only few of the numerous studies where the low-β approximation is invoked to neglect the influence of pressure.

The validity of this approximation is however not self-evident and its assessment constitutes the objective of this investigation. It will be shown that, even though many qualitative features might remain unchanged, the zero-β approximation is not strictly valid in incompressible MHD simulations.

4.2 Is β a relevant quantity in MHD simulations?

In the MHD description, the Navier-Stokes equations are modified by the presence of the Lorentz force $\boldsymbol{F}_L$. In Alfvénic units, this gives

$$d_t \boldsymbol{u} = \nu \Delta \boldsymbol{u} - \nabla P + \boldsymbol{F}_L. \tag{4.3}$$

where $\boldsymbol{u}(\boldsymbol{x}, t)$ is the velocity, $P(\boldsymbol{x}, t)$ the pressure and ν the viscosity. We consider for simplicity the incompressible isothermal formulation, where $\nabla \cdot \boldsymbol{u} = 0$ and the density ρ is

uniform. The left hand side of this equation represents the acceleration of a plasma-fluid element. Through Newton's second law the right-hand-side gives the force-balance per unit mass. We see the contributions of three forces: viscous friction, the pressure gradient and the Lorentz-force. The Lorentz-force is given by

$$\boldsymbol{F}_L = \boldsymbol{J} \times \boldsymbol{B}, \tag{4.4}$$

where the current density is given by the curl of the magnetic field $\boldsymbol{J}(\boldsymbol{x}, t) = \nabla \times \boldsymbol{B}(\boldsymbol{x}, t)$. Using vector identities, part of the Lorentz force can be written as the gradient of a scalar quantity, so that it can be regrouped with the pressure term. Doing so, equation (4.3) becomes

$$d_t \boldsymbol{u} - \nu \Delta \boldsymbol{u} = -\frac{1}{2} \nabla (B^2(1+\beta)) + \boldsymbol{B} \cdot \nabla \boldsymbol{B}. \tag{4.5}$$

where β is given by expression (4.1). It seems from this expression that if $p \ll B^2$, the hydrodynamic pressure drops out of the equation. This leads to the intuitive result that if in a plasma we measure a low value of β, the hydrodynamic pressure can be neglected. In this limit, (4.5) does not need the restriction $\nabla \cdot \boldsymbol{u} = 0$ anymore and the description thereby simplifies.

We will here illustrate that this approximation is not straightforward. The important point is that in equation (4.5), it is the gradient of the pressure and of the magnetic pressure which play a role, and not the values of the pressures themselves. If one would like to measure the influence of the hydrodynamic pressure gradient compared to the gradient of the magnetic pressure, one needs to compare the norms of these vectors. Introducing the unit vectors

$$\boldsymbol{e}_P = \frac{\nabla P}{\|\nabla P\|} \quad \text{and} \quad \boldsymbol{e}_B = \frac{\nabla B^2}{\|\nabla B^2\|} \tag{4.6}$$

one can write equation (4.5) as

$$d_t \boldsymbol{u} - \nu \Delta \boldsymbol{u} = -\frac{1}{2} \|\nabla B^2\| \left(\boldsymbol{e}_B + \boldsymbol{e}_P \beta_\nabla\right) + \boldsymbol{B} \cdot \nabla \boldsymbol{B}. \tag{4.7}$$

In this expression β_∇ is defined by

$$\beta_\nabla \equiv 2 \frac{\|\nabla P\|}{\|\nabla B^2\|}. \tag{4.8}$$

The difference between expressions (4.8) and (4.2) is obviously the presence of the gradients in the latter, which is essential in measuring the effects of pressure on the dynamics. Evidently a large uniform pressure will not induce any acceleration of the plasma and one can thus always change the value of the pressure without changing its gradient by adding a uniform pressure field.

Furthermore, the separation of the Lorentz-force into a gradient $\nabla(B^2/2)$ and $\boldsymbol{B} \cdot \nabla \boldsymbol{B}$ seems natural when we want to consider the influence of the pressure, and it is so in the absence

of motion, when the left-hand-side of equation (4.3) is zero. Computing subsequently an equilibrium field by considering a force-free magnetic state is a classical way to determine tokamak equilibria, already widely used in the early days of fusion research [17, 18], and plasma physics in general [56]. For this static case we have thus

$$\frac{1}{2}\nabla(B^2(1+\beta)) = \boldsymbol{B}\cdot\nabla\boldsymbol{B}, \tag{4.9}$$

and for small values of β, only the magnetic pressure can balance $\boldsymbol{B}\cdot\nabla\boldsymbol{B}$. However, if one focuses on the importance of the pressure on the nonlinear dynamics in equation (4.7), i.e. when $\boldsymbol{u} \neq 0$, there is no reason, other than esthetics, to separate the Lorentz-force in two parts. Indeed, as soon as the plasma will start to move, the acceleration $d\boldsymbol{u}/dt$ of the plasma will be governed by the pressure gradient, the Lorentz-force and the viscous stress, and the pressure gradient is no longer *a priori* negligible.

Note that we can ignore the contribution of the viscous diffusion of momentum on the acceleration when the dynamics become turbulent [57, 58]. This is plausible to hold in the present case for large values of the Lundquist number. Indeed, viscous dissipation is an essential feature in the eventual dissipation of kinetic energy of turbulent flows, but its influence on the acceleration is small, when eddy diffusion becomes more important than molecular viscous diffusion. We will not further consider it here.

What we will consider therefore is the comparison of the forces due to pressure, and the Lorentz-force. What we will therefore look at is the equation,

$$d_t\boldsymbol{u} - \nu\Delta\boldsymbol{u} = \left(-\boldsymbol{e}_P\beta'_\nabla + \boldsymbol{e}_F\right)\|\boldsymbol{J}\times\boldsymbol{B}\|, \tag{4.10}$$

where $\boldsymbol{e}_F = \boldsymbol{F}_L/\|\boldsymbol{F}_L\|$, and

$$\beta'_\nabla \equiv \frac{\|\nabla P\|}{\|\boldsymbol{J}\times\boldsymbol{B}\|}. \tag{4.11}$$

In order to have global measures of the importance of the different terms, we introduce, as in expression (4.2), the volume averaged quantities,

$$\overline{\beta}_\nabla \equiv 2\frac{\langle\|\nabla P\|\rangle}{\langle\|\nabla B^2\|\rangle} \quad \text{and} \quad \overline{\beta'_\nabla} \equiv \frac{\langle\|\nabla P\|\rangle}{\langle\|\boldsymbol{J}\times\boldsymbol{B}\|\rangle}. \tag{4.12}$$

It is only when $\overline{\beta'_\nabla}$ is small that the pressure term might be negligible in the dynamics. However, if this quantity is of order unity, there is no reasonable indication that the pressure gradient can be safely ignored. We will now assess this in the context of RFP simulations.

4.3 Validation of the Poisson-solver

The simulations we carry out consider incompressible visco-resistive magnetohydrodynamics in a periodic cylinder. The numerical method is described in Chapter 3. What we will validate here in addition to the code is the post-processing routines which resolve a Poisson equation to get the pressure field and compute the different quantities which appear in β, β_∇ and β'_∇.

This pseudo-spectral Poisson solver is benchmarked in a cylindrical geometry of a unit radius, at instant $t = 0$ where the momentum equation can be solved analytically. The initial velocity field is a random noise with a kinetic energy of the order of $E_k \approx 10^{-7}$, the initial current density has only an axial component $J_{z0} = 2.8$, and the magnetic field consists of an axial component $B_{z0} = 0.2$ and a poloidal component B_{p0} induced by J_{z0}. By considering the velocity terms negligible relative to the magnetic terms, the momentum equation can be written at $t = 0$ as,

$$\nabla P = \boldsymbol{J} \times \boldsymbol{B}. \tag{4.13}$$

Using the radial component of equation (4.13) and zero pressure boundary condition yields the following analytical solution,

$$P(r) = \frac{J_{z0}^2}{4}(1 - r^2). \tag{4.14}$$

The benchmark of the pressure, the magnetic energy and the Lorentz force profiles is presented in Figure 4.1. The numerical quantities obtained by the solver collapse well with the theoretical curves, validating its accuracy. Subsequently, the ratios β, β_∇ and β'_∇ are calculated analytically and compare to the numerical values with an error of order of 2% or less.

4.4 Results for β and β_∇ in straight-cylinder RFP simulations

4.4.1 Numerical set-up

In this section we will evaluate how $\overline{\beta}$, $\overline{\beta_\nabla}$ and $\overline{\beta'_\nabla}$ scale in incompressible MHD simulations in a periodic cylinder with aspect ratio $\Gamma = L_z/2\pi r = 4$, where L_z and $r = 1$ are the cylinder length and radius, respectively. Equation (4.7) is solved together with the induction equation,

$$\frac{\partial \boldsymbol{B}}{\partial t} = \nabla \times (\boldsymbol{u} \times \boldsymbol{B}) + \lambda \nabla^2 \boldsymbol{B}, \tag{4.15}$$

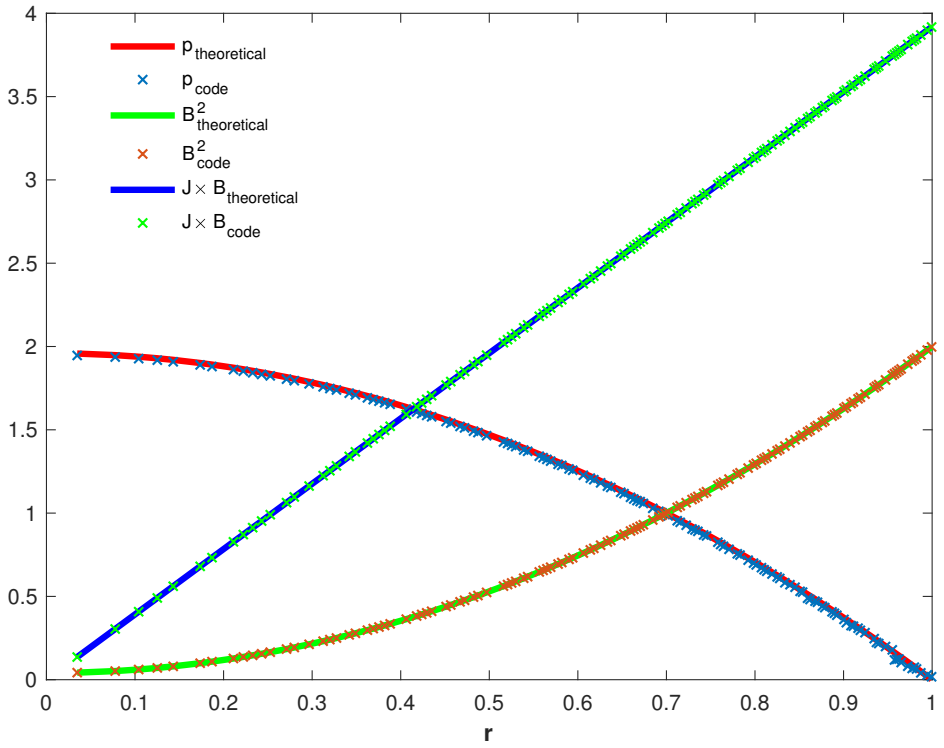

Figure 4.1: Comparison of the numerical and the analytical solution for the pressure P, the magnetic energy B^2 and the Lorentz force $\boldsymbol{J} \times \boldsymbol{B}$.

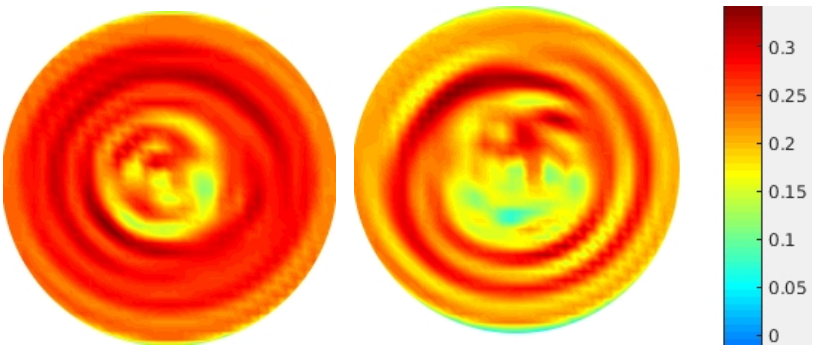

(a) (b)

Figure 4.2: Visualization of (a) $z = 0$ (b) $z = L/2$ cross-sections of the pressure field in the RFP in the turbulent state $S = 33600$ and $\Theta = 7$, in the statistically steady state.

and the condition $\nabla \cdot \boldsymbol{B} = 0$. Computations are performed using a pseudo-spectral solver on a Cartesian mesh of $128 \times 128 \times 512$ gridpoints, combined with a volume-penalization technique to enforce the boundary conditions. The boundary conditions are no-slip on the cylinder wall for the velocity. The magnetic field is enforced by imposing the poloidal component of the magnetic field B_p at the wall, which thereby determines the global axial current. The radial magnetic field vanishes at the wall and the axial component B_z consists of a uniform, fixed contribution plus a variable part which is left free to evolve, so that the magnetic field can self-organize towards a typical RFP dynamic equilibrium. Details on the numerical method can be found in chapter 3 and reference [45].

The pressure field is calculated using the incompressibility condition by solving the Poisson equation obtained from taking divergence of the momentum equation, expression (4.3),

$$\nabla^2 P = \nabla \cdot (-\boldsymbol{u} \cdot \nabla \boldsymbol{u} + \boldsymbol{J} \times \boldsymbol{B}) \,, \tag{4.16}$$

where the time-derivative and viscous term vanish due to incompressibility. In a pseudo-spectral code, this Poisson equation can be easily solved using Fourier transforms. The boundary condition for this resolution is zero pressure on the plasma boundaries. In all simulations, we will consider the RFP regime where the magnetic geometry is self-organized into a helical structure. Typical similations using the same code and set-up are reported in [46]. In Figure 4.2 we show visualizations of the pressure field in cross-sections of the cylinder for a typical flow.

4.4.2 Influence of the pinch-ratio

We consider first the case of a fixed Lundquist number, $S \equiv B_p r/\lambda = 2.8 \times 10^4$, $P_m \equiv \nu/\lambda = 1$ for different values of the pinch $\Theta = \overline{B}_p/\langle B_z \rangle$, where the overline indicates the surface average on the edge of the plasma and the brackets indicate a volume average. Error-bars here and in the following measure the temporal fluctuations of the evaluated quantities during the statistically stationary state, during which the quantities are evaluated.

In figure 4.3 the evolution of the different definitions of β is shown to stay constant with respect to the pinch ratio. Furthermore, $\overline{\beta}$ takes a value less than 20% while the quantity $\overline{\beta'_\nabla}$ is greater than 80%. Hence, even if the pressure is considered small compared to the magnetic field, its gradient plays a major role in the RFP dynamics regardless of the magnetic pinch ratio.

4.4.3 Influence of the Lundquist number

We now turn to the dependence of the different βs on the Lundquist number. In Figure 4.4 it is observed that increasing S, $\overline{\beta}$ drops, approximately following a powerlaw proportional

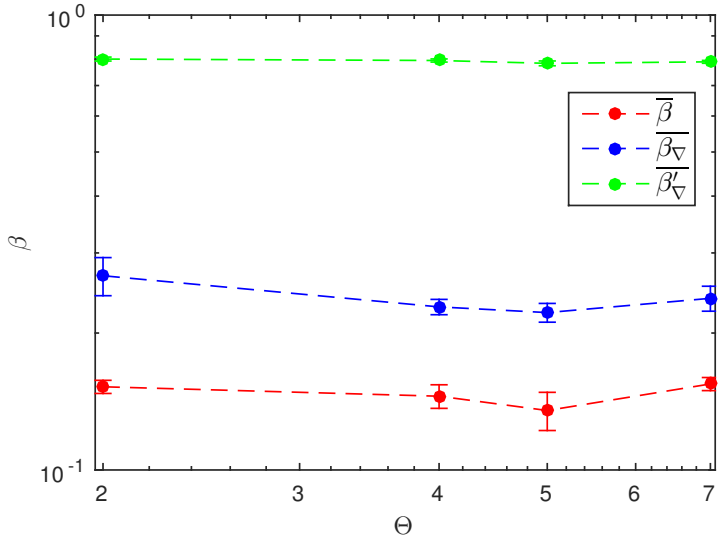

Figure 4.3: Importance of the pressure force on the dynamics as measured by $\overline{\beta}$, $\overline{\beta_\nabla}$ and $\overline{\beta'_\nabla}$ for different values of the pinch ratio with $S = 2.8 \times 10^4$.

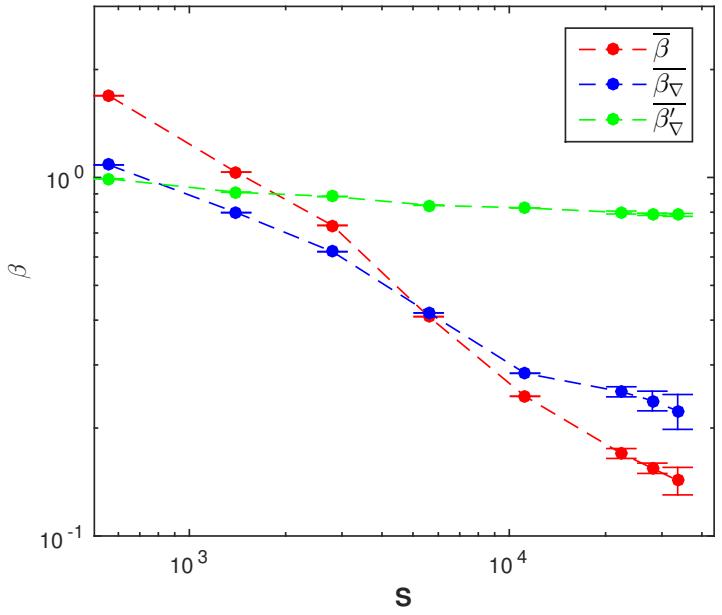

Figure 4.4: Importance of the pressure force on the dynamics as measured by β, $\overline{\beta_\nabla}$ and $\overline{\beta'_\nabla}$ for different values of the Lundquist number.

to $S^{-1/2}$. Judging from this dependence only, one would be tempted to say that in realistic regimes, where S is at least an order of magnitude higher, the pressure is negligible. However, considering the influence of the pressure gradient on the force balance by comparing the pressure-gradient to the Lorentz-force, it is observed that the influence of the pressure force remains comparable to the Lorentz-force for all values of S. Indeed $\overline{\beta'_\nabla}$ remains order unity when S is increased.

4.4.4 Influence of the poloidal shape

Now we study the influence of the poloidal shape of the cross-section on the different β ratios. The context and interest of this study will be illustrated in details in Chapter 5.

We consider 3 different geometries: a circle with a radius r=1, an ellipse with a major semi-axis $a = 1.2$ and minor semi-axis $b = 0.833$ and an ellipse with $a = 1.4$ and $b = 0.714$. Simulations in these 3 geometries are carried out for the same Lundquist number $S = 2\times10^4$ and pinch ratio $\Theta = 7$. The cross-sections of the pressure field of these three geometries are shown in Figure 4.5. First observation is that the pressure field changes drastically with the change of poloidal shape of the RFP. In the ellipses' case, the pressure reaches a maximum value of $P \approx 0.45$ in the central region while it reaches a value $P \approx 0.3$ in the circular case. Furthermore, the region in which the pressure exceeds 0.35 in the ellipses constitutes more than 50% of the surface of the cross-section, which is significantly more than the high pressure region observed in the circular cylinder. Subsequently, the mean of the pressure increases with cross-section elongation, and the values of β for the geometries with $a = 1; 1.2; 1.4$, are $\beta = 0.19; 0.35; 0.41$, respectively.

Now we consider the case of the ellipse with $a = 1.4$ and we check the influence of the Lundquist number on the different β ratios. The results plotted in Figure 4.6 show that β decreases with the increase of S, while β_∇ and β'_∇ tend to stay constant. The variation of β_∇ is different from the one observed in the circular case in Figure 4.4. This difference is possibly related to a more perturbed magnetic structure in the ellipses, which is further away from a force-free equilibrium than the circular case, but this needs further analysis.

The pressure gradient is thus not negligible in the dynamics. A question is now how the results change if the we neglect the pressure anyway. This will be illustrated in the following.

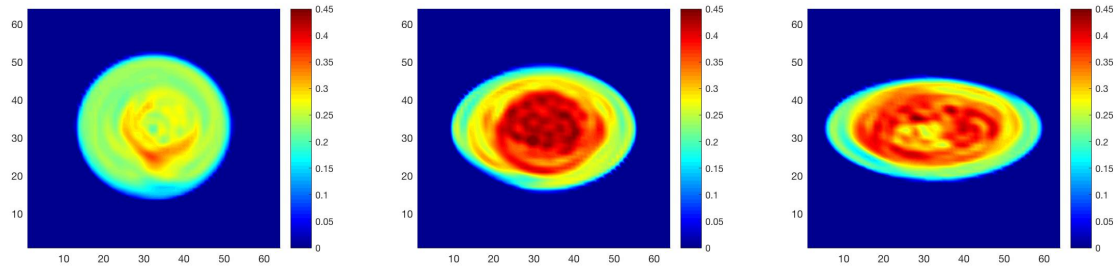

(a) (b) (c)

Figure 4.5: Visualization of the cross-section $z = L/2$ of the pressure field in the RFP in the turbulent state $S = 2 \times 10^4$ and $\Theta = 7$, for (a) a circle with $r = 1$, (b) an ellipse with $a = 1.2$ $b = 0.833$ and (c) an ellipse with $a = 1.4$ $b = 0.714$, in the statistically steady state.

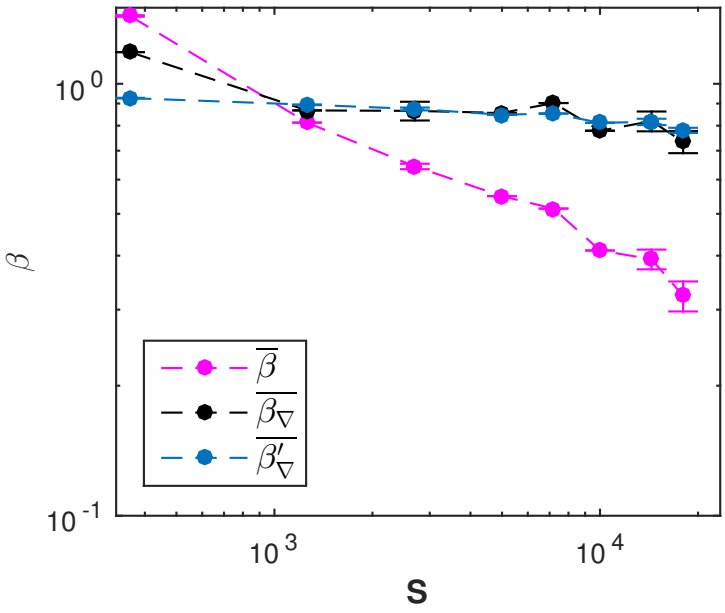

Figure 4.6: Importance of the pressure force on the dynamics of elliptical RFP with $a = 1.2$ $b = 0.833$, as measured by β, $\overline{\beta_\nabla}$ and $\overline{\beta'_\nabla}$ for different values of the Lundquist number.

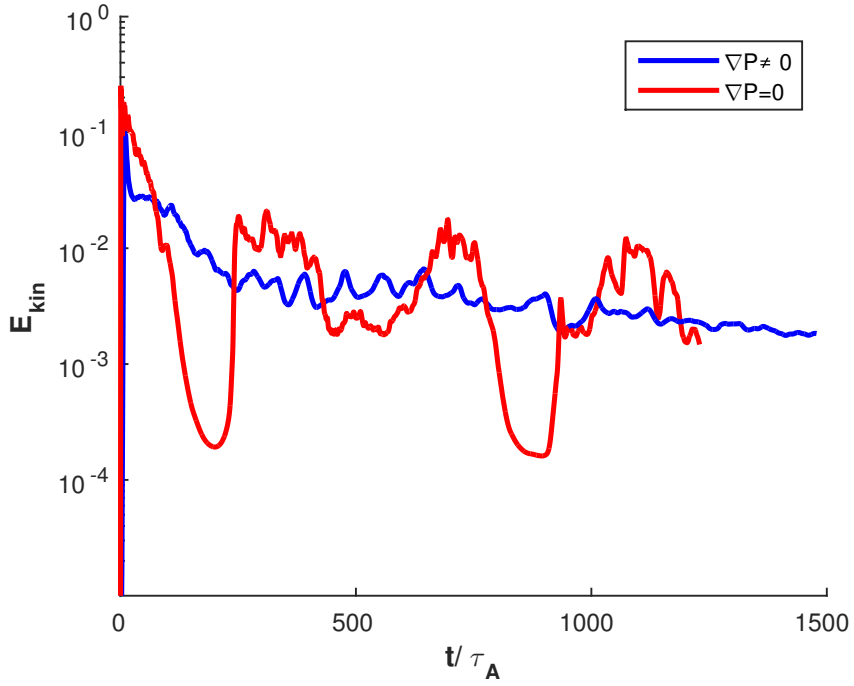

Figure 4.7: Time evolution of the kinetic energy for simulations with $S = 22400$ $\Theta = 7$, in the presence (blue) and absence (red) of the pressure gradient.

4.5 On the difference between incompressible and zero-β simulations

To illustrate the importance of the foregoing we will show here the influence of the pressure gradient term by removing it from the equations. The system we consider is thus

$$d_t \boldsymbol{u} - \nu \Delta \boldsymbol{u} = \boldsymbol{J} \times \boldsymbol{B}, \tag{4.17}$$

combined with equation (4.15). A similar comparison was reported in [59]. A theoretical study [33] explained some of the differences between the results.

In Figure 4.7 we show the evolution of the kinetic energy ($E_{kin} = (|\boldsymbol{u}|^2)/2$) for two simulations at $S = 22400$, $\Theta = 7$. It is observed that the dynamics are more violently fluctuating in the pressureless simulations. In Figure 4.8 we show the average axial magnetic field as a function of the radial coordinate. We compare the results from incompressible and zero-β simulations for Lundquist numbers ranging from $S = 11200$ upto $S = 33600$. The main observation is that we have a dichotomy where the profiles of the simulations without

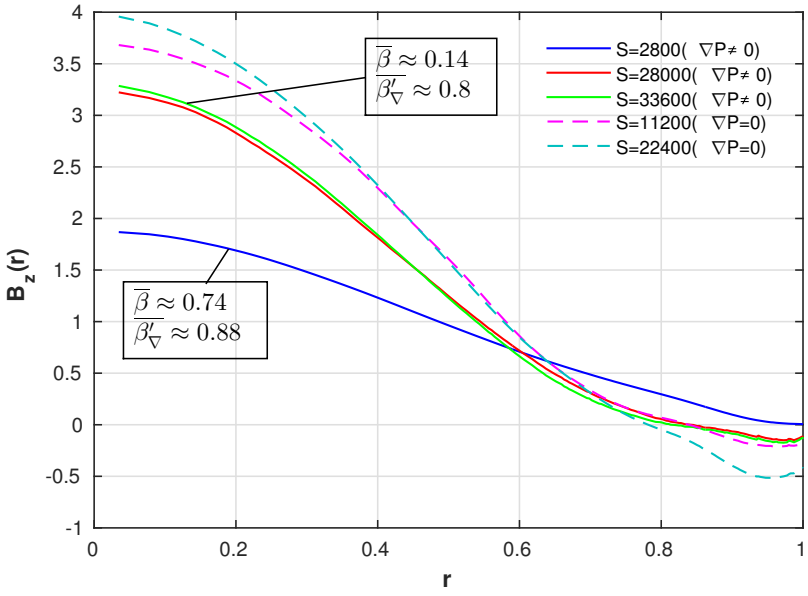

Figure 4.8: Importance of the pressure force to determine the magnetic field for different values of the Lundquist number.

pressure are qualitatively different from the full incompressible dynamics. For both cases the profiles become roughly independent of S for $S > 10^4$, but the asymptotic profiles are different with a deeper reversal for the pressureless dynamics.

For the incompressible runs we have a β which decreases as a function of S, as shown in 4.4. We observe that between the lowest and the highest values of the Lundquist number, β has decreased significantly. However, even at the highest value of S, the radial profile of the axial magnetic field has not approached the incompressible solution towards the zero-β solution. This clearly illustrates that the pressure plays an important role and that it is not β which can measure the importance of the pressure force on the dynamics. Indeed the value of $\overline{\beta'_\nabla}$ is of order unity for all the incompressible simulations.

4.6 Conclusion

We have argued that the quantity which measures the importance of the pressure on the dynamics in incompressible MHD simulations is $\overline{\beta'_\nabla} = \langle \|\nabla P\| \rangle / \langle \|\boldsymbol{J} \times \boldsymbol{B}\| \rangle$. Indeed, it is shown that even when β might vary considerably, in particular when increasing the Lundquist number, the value of $\overline{\beta'_\nabla}$ remains of order unity and the influence of the pressure

gradient cannot be neglected. Our results considered the simplest case of incompressible isothermal flow. We have not carried out simulations of compressible MHD, but the results will probably be intermediate between those of the pressureless and the incompressible cases considered in the previous section. Complexifying the description is however an interesting issue to be further explored.

These results in no sense invalidate the insights obtained in the zero-β simulations. Indeed, a lot of qualitative features observed without pressure can carry over to the actual incompressible MHD dynamics. Some of this coincidence is fortunate and it would be wise to validate these results using more a more complete MHD description involving the pressure term. However, MHD is already a very simplified description of the actual plasma and ignoring the pressure gradient is only one approximation among many others. It is our viewpoint that MHD simulations should be considered as tools to discover possible physical mechanisms, which can be assessed in realistic experiments. Furthermore, neglecting the pressure in MHD is less dramatic than in hydrodynamics. Indeed, the presence of the magnetic pressure will take over part of the role normally played by the hydrodynamic pressure. This is not so in the absence of a magnetic field, where the pressureless equations (Burger's equation) will lead to a far more extreme dynamics with large gradients and shocks which change completely the flow-dynamics. However even in the present case the pressureless dynamics are more violent than the full incompressible system, as illustrated in Figure 4.7.

What should be retained from this study is that the pressure forces play an important role on the dynamics. It might be due to the dominance of tokamaks in fusion research that a low-β is associated with negligible pressure effects. Indeed in tokamaks often the MHD-induced flows are considered small. In such a case the left-hand-side of equation (4.3) can be neglected. When this is the case, one can have the approximate equality

$$\nabla P \approx \boldsymbol{J} \times \boldsymbol{B}. \tag{4.18}$$

It is in this case possible that both sides are close to zero, and $\nabla P \approx 0$. In this situation a force-free magnetic field can be constructed from the equality $(1/2)\nabla B^2 \approx \boldsymbol{B} \cdot \nabla \boldsymbol{B}$, leading to classical equilibrium configurations. However, as soon as the velocity is unequal to 0, nonlinear-dynamics drastically change the picture and the pressure gradient is no longer purely decorative.

Chapter 5

The effect of shaping on RFP dynamics

The influence of the shape of the plasma on the dynamics of RFPs is investigated in numerical simulations of fully nonlinear visco-resistive magnetohydrodynamics. The axial mode-spectrum is qualitatively changed in cylinders with elliptic cross-section, and the radial turbulent diffusion is affected. Even though from the present study it cannot be concluded what the optimal shape of an RFP should be, it is clear that the shape of the cross-section is an important parameter that should be taken into account when optimizing the confinement quality of an RFP.

5.1 Introduction

Tokamaks are supposed to work in a stable regime where the magnetic field roughly corresponds to the imposed magnetic field. It is therefore a quite obvious thing to change the shape of the magnetic geometry of the tokamak and to measure the influence of this change on the stability properties. Therefore the optimization of the confinement quality for tokamak plasmas by changing the plasma shape has been the subject of many studies. For instance, it has been shown that shaping has a beneficial effect on the β limits of tokamaks [60], and increases the total plasma current I in the case of elliptic cross-sections, yielding thereby a better confinement.

Since RFPs work in the unstable, self-organized regime, where the magnetic field is very different from the imposed one, the question how to control and optimize the confinement is quite different. Indeed, instability studies starting from a magnetostatic equilibrium, do not make sense in the nonlinear regime. However, other control strategies can be used.

Indeed, applying helical magnetic perturbations seems a promising way to affect the self-organized state in an RFP [53]. Another obvious way would be to change directly the shape of the plasma. Since RFPs operate beyond the MHD instability threshold, one should not measure the effect of the change in the geometry on the stability, but directly on the confinement quality of the nonlinear saturated state.

Investigations on the influence of shaping on the confinement properties of RFPs are, however, relatively scarce. Some rare examples of experimental observations were presented in [61, 62], and numerical investigations are reported in references [51, 63] where two-dimensional equilibrium studies were carried out in order to investigate the shaping effect on RFP plasmas. Their work led to the conclusion that shaping does not bring an advantage to the plasma dynamics in RFPs and is even destabilizing in the case in which the poloidal cross-section is elongated. These studies focused on the stability properties of RFPs, but did not consider the fully developed nonlinear dynamics. Here we proceed one step further in the investigation of the effect of changing the shape of the cross-section of RFPs by considering the fully nonlinear dynamics within a resistive fluid description. More precisely, we investigate the effect of elongation of the poloidal cross-section on plasmas in RFPs by means of direct numerical simulations using a three-dimensional MHD pseudo-spectral solver [47]. We consider the simplified case where the torus is modeled by a straight periodic cylinder. We justify the choice of this simplification as follows. In reference [46], we compared the straight-cylinder approach to fully toroidal simulations. We showed that most of the qualitative features remained unchanged. The most significant change was the appearance of a toroidally invariant mode, the influence of which we do therefore necessarily neglect in the present work. It is true that considering the effect of curvature on the dynamics of RFP could be interesting, but we aim at the understanding of the two effects (curvature and shape of the cross-section) independently in order to pinpoint the most important physical effects, before considering their possible interplay. Furthermore, in Paccagnella et al. [51] the influence of curvature was considered with respect to the stability properties of RFPs and its effect was shown to be minor.

In the present work is shown that elongation of the cross-section has a significant effect on the dynamics of the plasma. To probe the confinement, we consider the advection of a passive scalar, injected in the core of the plasma. The mean scalar profile that establishes allows us to directly determine the turbulent diffusivity associated with the RFP dynamics. The results of our simulations show that in some cases the confinement compared to circular RFPs is improved by shaping.

5.2 Equations, numerical methods and parameters

5.2.1 Visco-resistive MHD equations

We repeat here the governing equations,

$$\frac{\partial \boldsymbol{u}}{\partial t} = -\nabla \Pi + \boldsymbol{u} \times \boldsymbol{\omega} + \boldsymbol{J} \times \boldsymbol{B} + \frac{P_m}{S} \nabla^2 \boldsymbol{u}, \tag{5.1}$$

and

$$\frac{\partial \boldsymbol{B}}{\partial t} = \nabla \times (\boldsymbol{u} \times \boldsymbol{B}) + S \nabla^2 \boldsymbol{B}, \tag{5.2}$$

where the magnetic Prandtl number $P_m = \nu/\lambda$ is the ratio of kinematic viscosity over magnetic diffusivity and $S = B_0 \mathcal{L}/\lambda$ the Lundquist number. The velocity field $\boldsymbol{u}$ and the magnetic field $\boldsymbol{B}$ are both divergence free,

$$\boldsymbol{\nabla} \cdot \boldsymbol{u} = 0, \tag{5.3}$$

$$\boldsymbol{\nabla} \cdot \boldsymbol{B} = 0. \tag{5.4}$$

We stress that the pressure is not neglected and is obtained from the incompressibility condition by taking the divergence of the momentum equation (5.1) and solving the resulting Poisson-equation. We illustrated in the previous chapter that it is important to retain this feature in the dynamics unlike in previous investigations of RFPs (e.g. [34, 64]), where the pressure was entirely neglected invoking low-β dynamics. We thus take into account the influence of pressure on the dynamics, but we neglect all compressibility effects and consider the dynamics of an isothermal plasma. Note that imposing incompressibility was shown to diminish the reversal of the magnetic field [65] (see also section 4.5), and this will thus necessarily be the case in the present investigation. We note here that the resistivity profile can also influence the reversal [66]. The combined influence of shaping, compressibility and non-uniform resistivity constitutes an interesting perspective for future work.

5.2.2 Shaping parameters

In the present investigation we focus on the influence of the shape of the cross-section on the confinement properties of the plasma. The parameters should be carefully chosen to disentangle the effect of changing the geometry from the effect of changing other control parameters. Considering a periodic cylinder instead of a torus is motivated by this attempt to reduce the number of control parameters to a strict minimum. Even in this simplified geometry, the way in which the parameters are varied is not unique. For instance, if the same toroidal current-density J_z is chosen for two geometries, the mean current I_z will be

the same, only if the surface A of the cross-section is kept constant, a condition which we will impose. This will also lead to equal values of the toroidal magnetic flux $\psi = B_z A$, for a given imposed toroidal magnetic field B_z.

The poloidal magnetic B_p field is computed from the current density. Its reference value is evaluated as an average over the circular, or elliptic boundary. Necessarily, keeping the surface A, J_z and B_z fixed, the average value $\overline{B}_p$ varies when changing the shape of the cross-section (the bar indicates a boundary average). The pinch-ratio, defined as

$$\Theta = \frac{\overline{B_p}}{\langle B_z \rangle}, \tag{5.5}$$

where the brackets denote a volume average, therefore depends on the value of the ellipticity c. An important parameter in non-ideal MHD is the Lundquist number, which we define as

$$S = \frac{2\bar{B}_p b}{\lambda}, \tag{5.6}$$

where we used the poloidal magnetic field strength and minor radius as reference quantities. We have chosen b, rather than a, since it is this smallest minor radius which will probably determine the confinement quality. This choice is further discussed in section 4. Imposing the same value of S for different values of the ellipticity allows to determine the value of λ. In all our simulations the value of the magnetic Prandtl number, P_m is chosen unity.

The influence of β and β_∇ was considered in the previous chapter, where it was shown that β is not the important parameter to measure the influence of the pressure on the dynamics. Indeed in our incompressible simulations β is not a control parameter. We have therefore not tried here to keep β equal in the different simulations, however it is shown that the dynamically important parameter $\overline{\beta'_\nabla}$ is of the same order of magnitude in the different simulations.

5.3 Results

5.3.1 F-Θ stability

The imposed magnetic field in RFPs is unstable for large values of Θ and S, and it will form a dynamic helical structure with a certain amount of chaotic or turbulent motion superimposed.

The modification of the magnetic field can be quantified by the field reversal parameter F, representing the normalized toroidal field at the boundary,

$$F = \frac{\overline{B_z}}{\langle B_z \rangle}. \tag{5.7}$$

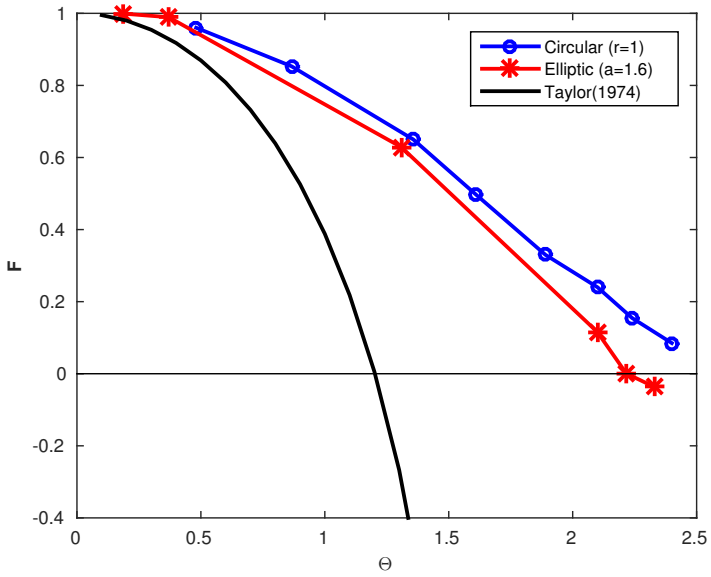

Figure 5.1: Field reversal parameter F as a function of the pinch parameter Θ for cylinders with circular and elliptic cross-section. Also shown is Taylor's prediction [6] for reference.

As the current increases, the kink instability increases, leading to the decrease of the toroidal magnetic field at the boundary, so that F decreases as a function of Θ.

This behavior is qualitatively predicted by Taylor's theory [6] and more sophisticated theories allow to improve this agreement [30,41,67]. In studies [51,63] based on two-dimensional equilibrium equations, it was shown that shaping does not alter the F-Θ curve. Preliminary simulations for cylinders of small aspect ratio $L_z/2\pi b \sim 2$ and $S \sim 4200$ are carried out and compared with Taylor's prediction [6] for an ellipticity $a = 1.6$. Figure 5.1 shows the results of the field reversal parameter F versus Θ. In previous studies [51, 63] it was shown that shaping had a small destabilizing effect for large curvature, but the $F-\Theta$ curve was unaffected. Indeed, the two geometries yield roughly the same behavior. We confirm this observation, even though our numerical values of F are substantially higher than in these references. The effect of compressibility might explain this discrepancy [33].

The reversal parameter is a global parameter and does not give insight into the fine structure of the dynamics. It is this fine structure, constituted by the nonlinear interplay of a large number of modes which will determine the confinement quality of a reactor. The modification of the fine structure is now assessed by evaluating the modal behavior of the flow.

5.3.2 Helical modes and safety factor

We study now the effect of shaping on the helical modes. We have hereto performed simulations for a higher value of S and a larger aspect ratio $L_z/2\pi b = 4$ to approach more realistic conditions. We consider three shapes: a circle with radius $r = 1$, an ellipse with $a = 1.2$ $b = 0.83$ and an ellipse with $a = 1.4$ and $b = 0.714$. The Lundquist number for the three cases is $S \approx 2.10^4$ and the magnetic Prandtl number is $P_m = 1$. To give an idea of the intricate structure of the velocity field, we show in figure 5.2 an illustration of an instantaneous velocity field. The complex helical structure is clearly visible in this visualisation.

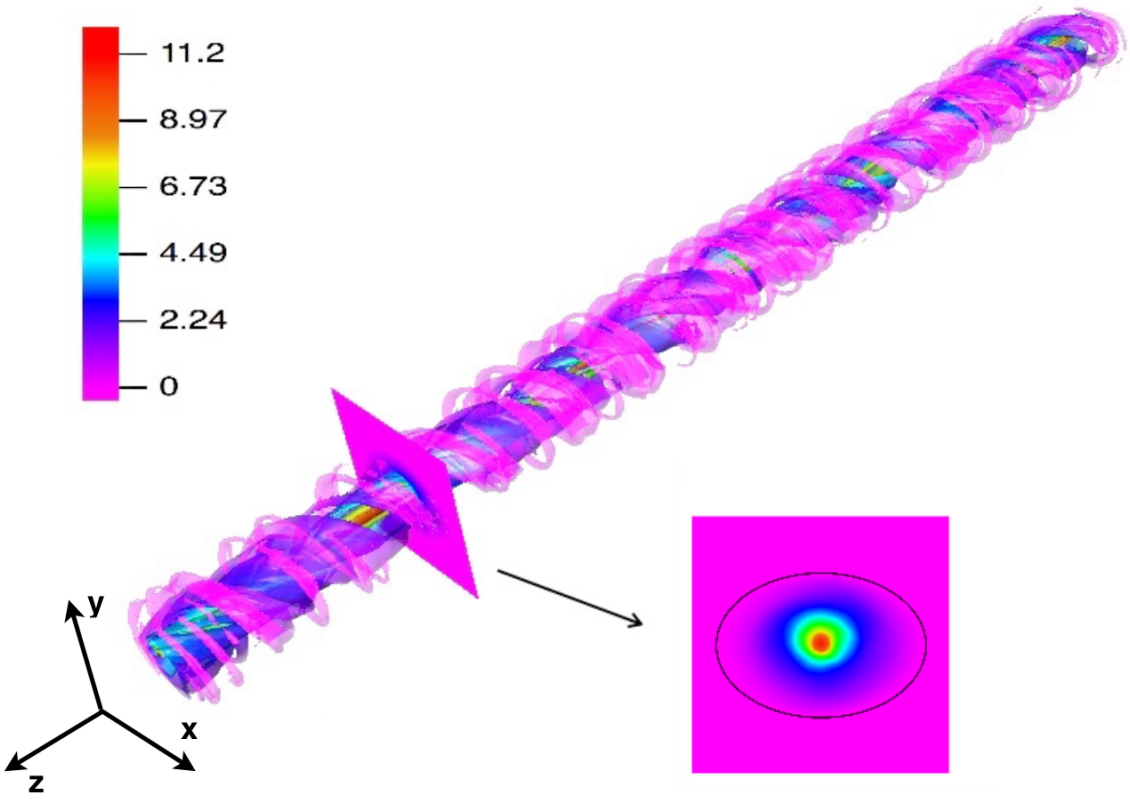

Figure 5.2: Isosurface of axial velocity $u_z = 8.10^{-2} C_A$ colored by the scalar field for an ellipse with $a = 1.2$.

Figure 5.3 shows the predominance of a magnetic mode with toroidal modenumber $n = 7$ in the circular case, which is consistent with what has been observed in the RFX-mod device.

In the elliptical case ($a = 1.2$) a tendency for mode $n = 14$ to dominate is observed, while the magnetic modes $n = 3$ and $n = 4$ contain most of the magnetic energy for $a = 1.4$. This last case seems to be closer to a multiple-helicity state, where not a single mode contains most of the energy. Similar spectral differences are observed in the kinetic spectra, where $n = 0$ and $n = 1$ are the dominating kinetic modes in the circular case, $n = 14$ in the $a = 1.2$ elliptical case, and $n = 8$ in the $a = 1.4$ elliptical case.

Further information of the magnetic structure of the plasma is given in Figure 5.4(a-c), where we display contours of the magnetic flux surfaces in a given cross-section. A clear difference is observed. In the circular case, concentric circular contours are observed, whereas in the $a = 1.2$ case magnetic islands appear at the edges of the ellipse. Similar behavior to the latter case is observed in the most elongated case, but additional magnetic islands appear in the central region of the ellipse.

The safety factor is defined as

$$q(\psi) = \oint \frac{B_z}{B_p} \frac{dl}{2\pi r}, \tag{5.8}$$

where ψ is the magnetic flux. Figure 5.4 shows the profile of the safety factor q for the three geometries as a function of the normalized flux, defined as $(\psi - \psi_0)/(\psi_{sep} - \psi_0)$, where ψ_0 is the minimum magnetic flux in the core plasma and ψ_{sep} is the magnetic flux at the separatrix.

The value of q at the center increases considerably with the increase of the ellipticity. In Fig 5.5 axial magnetic fluctuations are shown in various poloidal cross-sections. The fluctuations of the axial magnetic field are obtained by showing the magnetic field without the axially invariant ($k_z = 0$) magnetic contribution. Only in a few sections a clear poloidal mode structure is observed. These graphs, combined with the spectra shown in Figure 5.3 give a hint about the possible instabilities underlying the dynamics. Tearing modes are known to appear on places in the plasma where the ratio $m/n = q$ is close to a rational number. For the circular geometry, where an $n = 7$ magnetic toroidal mode is dominant, in one of the cross-sections a clear $m = 1$ poloidal structure can be identified. The value $q = m/n = 1/7$ is not attained in the plasma, but this value is approached in the center of the domain (see Figure 5.4(d)). The triggered instability could possibly be associated with an ideal kink mode. For the elliptical cylinder with $a = 1.2$, a hint of $m = 1$ and $m = 2$ structures is visible in the cross-sections taken at instant $t = 9.8 \times 10^3 \tau_A$, where the $n = 14$ magnetic mode is dominant. The same analysis at different instants where no magnetic mode n dominates, shows the persistance of the poloidal mode $m = 2$. Thus, both rational surfaces $q = 1/14$ and $q = 2/14$ are within the plasma, so that in this case external tearing modes are a candidate to explain the underlying dynamics, even though modes near the axis are generally observed to be more unstable. The conclusion from these observations is that shaping significantly influences the velocity and magnetic fields, both qualitatively and quantitatively.

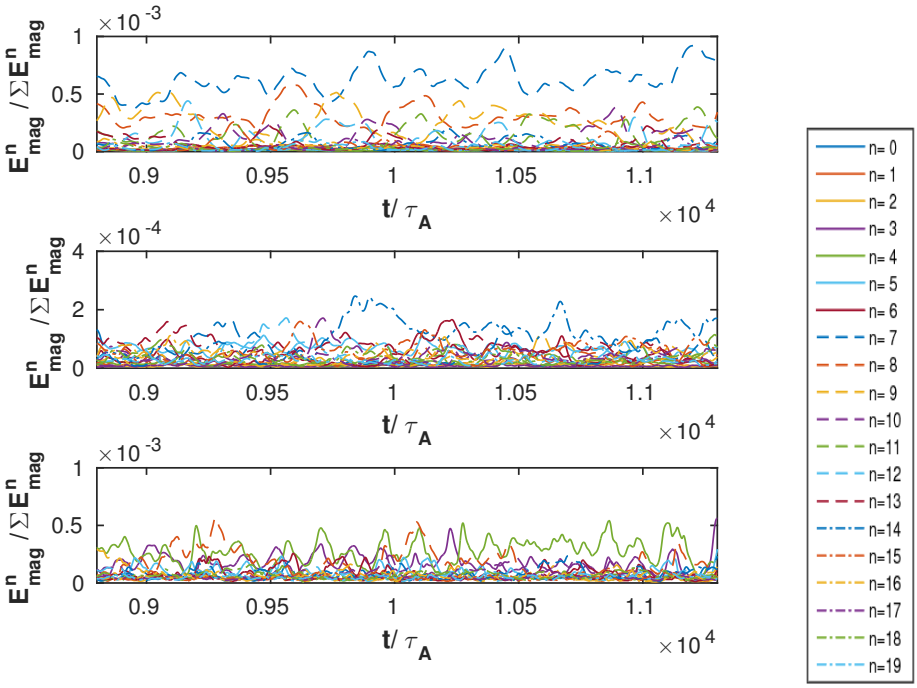

(a)

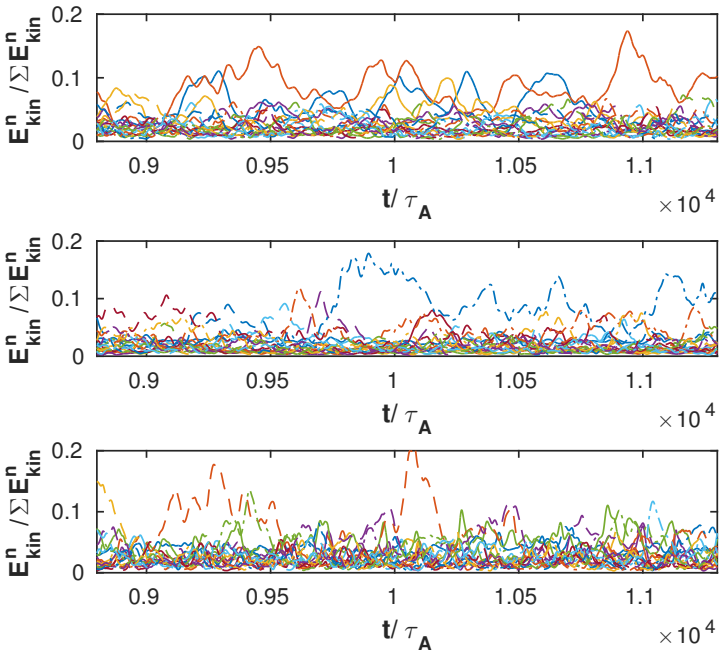

(b)

Figure 5.3: Axial spectra of magnetic (a) and kinetic (b) energy, normalized respectively by the total magnetic and kinetic energy, considering three shapes, respectively from top to bottom, a circle with radius r=1, an ellipse with major semi-axis a=1.2 and one with a=1.4.

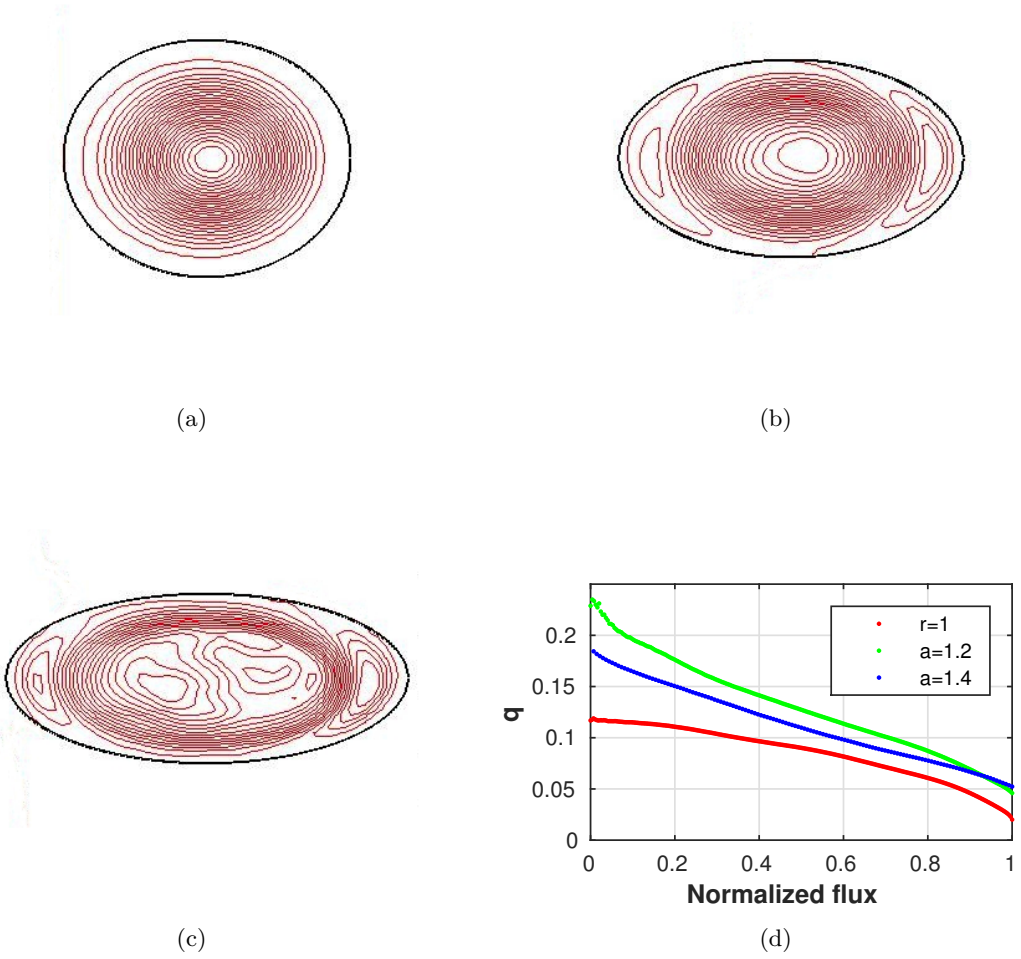

(a) (b)

(c) (d)

Figure 5.4: Profile of the safety factor q function of the normalized flux, for the three geometries at $t = 9.8 \times 10^3 \tau_A$. Flux surfaces for the three geometries.

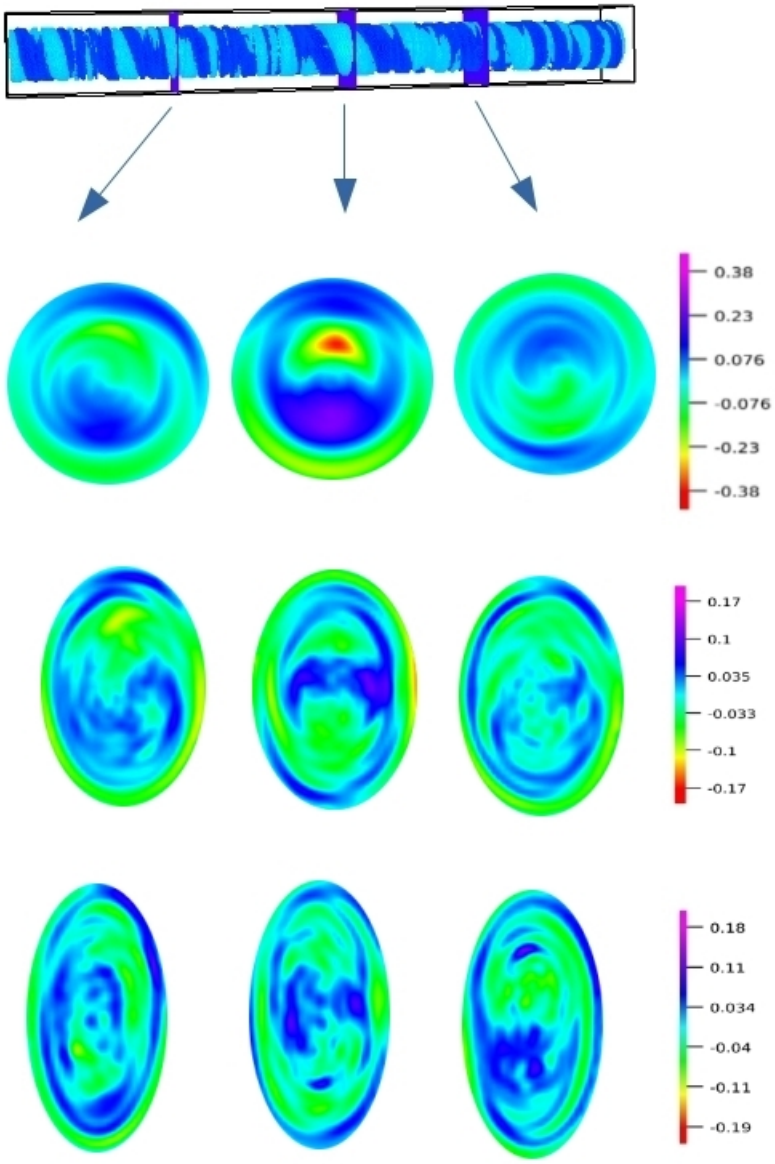

Figure 5.5: Poloidal cross-sections of the cylinder for circular (top) and the two elliptical (center, bottom) geometries, illustrating the axial magnetic fluctuations at $t = 9.8.10^3 \tau_A$.

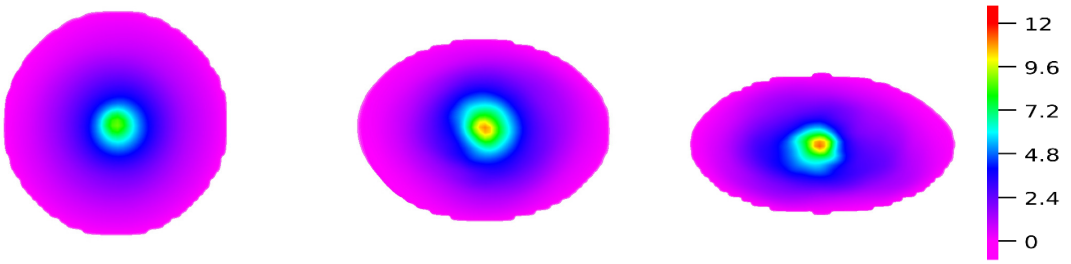

Figure 5.6: Cross-section of the scalar field for different shapes, for $S \sim 2.10^4$ and $L_z/2\pi b = 4$.

5.3.3 Turbulent diffusion

In order to assess the influence of the velocity field on the confinement, we have compared the radial diffusion of a passive scalar in the different geometries. By fixing the rate of injection at the same value for all three geometries, the confinement can be evaluated by the mean scalar profile which establishes in the statistically stationary state. The injection corresponds to a constant force term f_T at the RHS of the temperature evolution equation,

$$\frac{\partial T}{\partial t} + \boldsymbol{u} \cdot \nabla T = \alpha \nabla^2 T - \frac{\chi}{\eta}(T - T_{wall}) + f_t, \tag{5.9}$$

which is non-zero only in a central region with $r < 0.1$. The value of T at the wall is kept constant and is fixed at zero value using the penalization technique. The value of T at the center of the plasma is thereby a direct measure of the confinement quality. In the present work, T is therefore an auxiliary quantity, which in the case of small temperature fluctuations, assuming isotropic transport coefficients, could be associated with the temperature. However, in the present case we do not model the interaction of the plasma in the presence of temperature differences, but we consider the case of an isothermal plasma, where T is a passive scalar, advected by the RFP velocity field. An investigation of the fully coupled problem between velocity and temperature will be done in a future work.

One particularly important feature of magnetized plasmas is ignored here. This feature is the anisotropy of the transport coefficients. Since the mean free path along the magnetic field lines is orders of magntitude larger than the Larmor-radius, which determines the mean free path perpendicular to the magnetic field, the homogeneization of a scalar quantity such as the temperature is very fast along the magnetic field. This can be taken into account by anisotropic diffusion coefficients. This is beyond the scope of the present analysis. Nevertheless, the advection of a passive scalar will allow to measure the turbulent diffusivity due to the velocity fluctuations. Our result can thus only be interpreted to probe the turbulent diffusion, which is, as we verified, larger than the molecular diffusion due to α, in our simulations.

A difficulty in the comparison of the diffusion is the fact that for the elliptical cross section, the scalar profile depends on the angle, and that in any case the maximum scalar does not need to be exactly in the center. What is important for confinement, is the maximum temperature, not necessarily its spatial location. In order to overcome all these difficulties, we define a sorted scalar profile, by sorting all scalar values in the plasma from high to low. By properly normalizing the x-axis, we convert this sorted dataset into an effective scalar profile, corresponding to a circular, perfectly centered, axisymmetric scalar distribution. This procedure is somewhat similar to the introduction of a magnetic flux function in tokamak studies. However, here the ordering of the spatial points is carried out as a function of isothermal contours. This type of sorting of temperature profiles is common in studies of stratified turbulence [68].

In practice, these profiles are obtained by sorting the different points in the fluid domain of each plane orthogonal to the z-axis, in decreasing order of scalar value, then averaging over the volume. All geometries have the same number of points in the fluid domain because of the equal cross-sections. The sorted profiles are shown in Figure 5.7 left. The x-axis is now a function of the generalized radius $\widetilde{r}$. This generalized radius is defined by

$$\tilde{r} = \sqrt{\frac{n}{N}} r_0 \tag{5.10}$$

where N is the total number of measurement points, n the n-th point of the sorted values and r_0 the reference radius, which equals 1 in our case. For non-axisymmetric profiles and cross-sections this representation will allow a direct comparison between the different scalar distributions.

Figure 5.6 and 5.7 show that the elliptical cases have the highest scalar value in the center of the plasma. The turbulent diffusion associated with the chaotic-turbulent motion can be directly evaluated from the average scalar profile by introducing an effective diffusivity D_T defined by,

$$D_T = \frac{G}{\tilde{r}\frac{\partial \langle T \rangle}{\partial \tilde{r}}} \qquad \forall\ \widetilde{r} > r^* \tag{5.11}$$

where G is the total injected heat computed from the scalar source term,

$$G = -\iint_0^{r^*} f_T r d\theta dr, \qquad \text{with} \quad r^* = 0.1. \tag{5.12}$$

A peak in the diffusivity profile in the near-wall region $0.8 < \tilde{r} < 1$ is observed, which could possibly be associated with an enhanced level of turbulence, generated in the shear-layer between the helical structure and the wall.

A further, more detailed characterization of the transport, probing the stochasticity of the flow, using for instance Poincaré maps, would be an interesting perspective. Also, considering directly the Ohmic heating as a source term, would be an elegant way to investigate the temperature diffusion in a self-consistent manner.

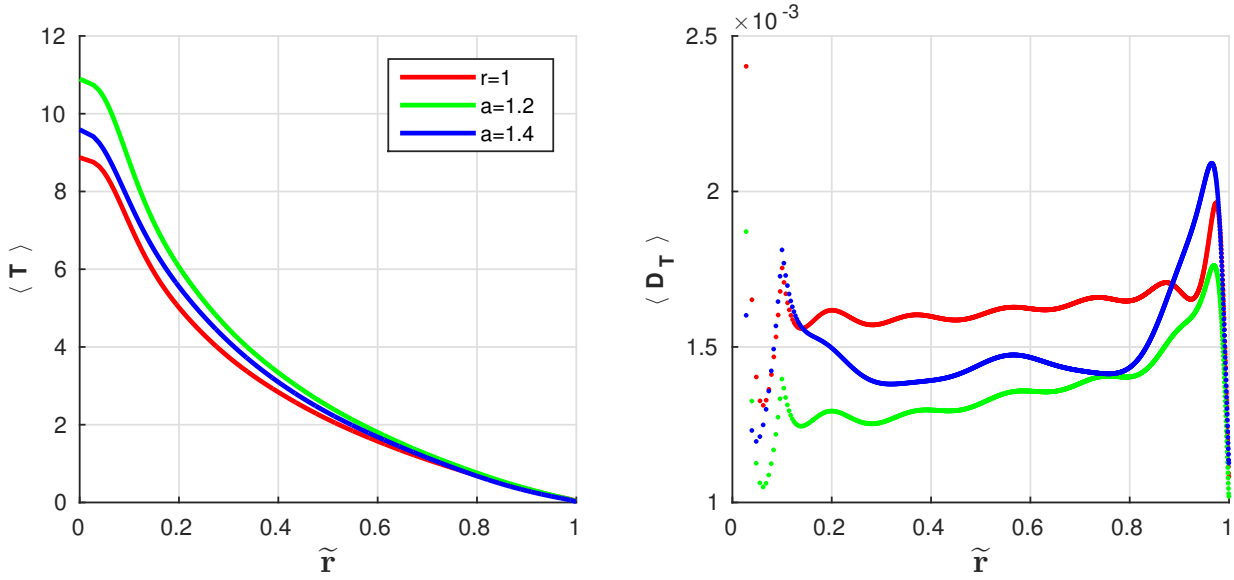

Figure 5.7: Mean scalar profiles as a function of the generalized radial coordinate $\tilde{r}$ (left). Effective diffusivity profile normalized by the cross-sectional surface. Both profiles are time-averaged over $3 \times 10^3 \tau_A$ (right).

5.4 On the choice of different characteristic scales

Different physical systems can only be meaningfully compared if the dimensionless parameters of the system are evaluated. These dimensionless numbers appear in general when the evolution equations of the system are non-dimensionalized by appropriate length, time, magnetic and other relevant scales. Hereby appear, for the case of MHD, dimensionless quantities like the Hartmann and Lundquist number. For example, the Hartmann number defined as,

$$Ha = \frac{C_A \mathcal{L}}{\sqrt{\eta \nu}}, \tag{5.13}$$

where η is the magnetic resistivity, $\mathcal{L}$ is a characteristic length scale and C_A the Alfvén velocity, plays a major role in describing laminar MHD dynamics [69–71] and the transition from multi-helical states to single-helical states [34]. On the other hand, the Lundquist number S is generally used in the fusion community to describe the plasma dynamics in the turbulent regime. For our case, where $\eta = \nu$, those two numbers have equal values, $Ha = S$. An important question is now how to define the length scale $\mathcal{L}$.

In the case of a circular cross-section, the most logical choice of the reference length scale is the radius of the cylinder. Deforming the cross-section breaks the symmetry of the

	r	a	b	C_A	$\mathcal{L}$	λ
Case 1	1	-	-	$\overline{B_p} = 1.4$	r	1.4×10^{-4}
	-	1.2	0.83	$\overline{B_p} = 1.36$	b	1.1×10^{-4}
	-	1.4	0.71	$\overline{B_p} = 1.26$	b	9×10^{-5}
Case 2	1	-	-	$\overline{B_p} = 1.4$	r	1.4×10^{-4}
	-	1.2	0.83	$\overline{B_p} = 1.36$	$\sqrt{ab}$	1.35×10^{-4}
	-	1.4	0.71	$\overline{B_p} = 1.26$	$\sqrt{ab}$	1.25×10^{-4}

Table 5.1: Parameters for case 1 where $\mathcal{L} = b$ and case 2 where $\mathcal{L} = \sqrt{ab}$, for the three geometries.

problem, and the radius is not longer uniquely defined by a simple number. A rather logical choice of the reference length is now $\mathcal{L} = \sqrt{ab}$, but this choice is not free from some arbitrariness. Another relevant length scale could be b, the minor axis, since this length scale is the smallest distance from the center to the wall, and as such it could pilot the confinement quality of the plasma. The choice of these two different typical length scales leads, for a given toroidal magnetic field and Lundquist number, to distinct values of the magnetic diffusivity. We have therefore considered two different choices for $\mathcal{L}$ and evaluated their impact onto the dynamics. The parameters of different cases are summarized in table 5.1.

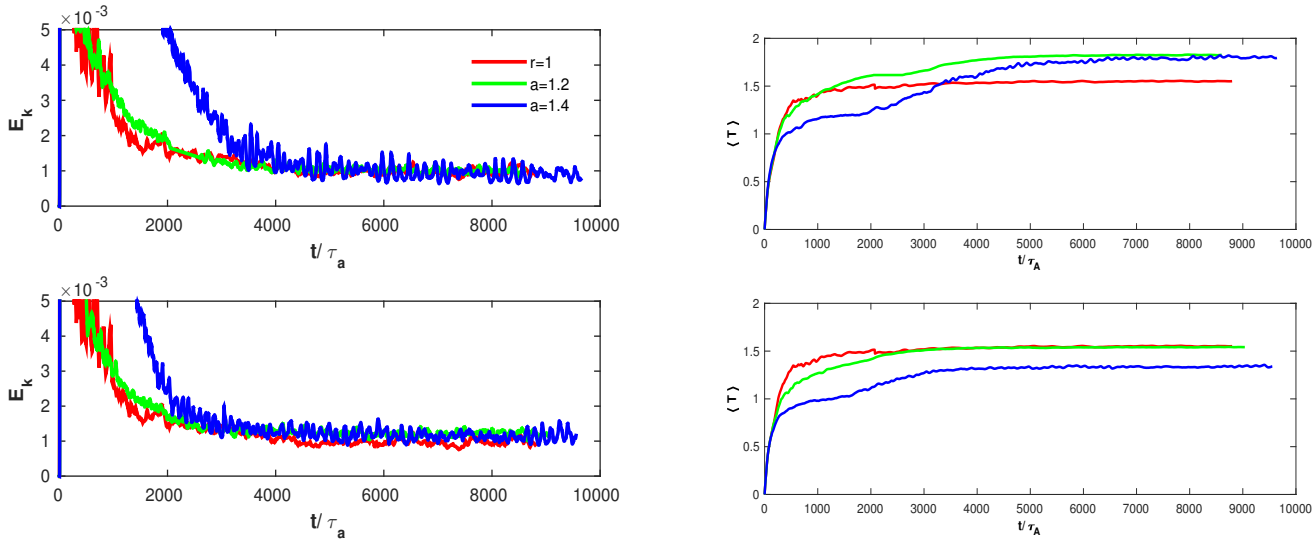

Figure 5.8: Evolution in time of the kinetic energy E_k (left), and the mean of the scalar value $\langle T \rangle$ (right), respectively from top to bottom for cases 1 and 2.

First, the evolution of the kinetic energy and average scalar value for cases 1 and 2, having the same characteristic magnetic scale and different lengthscales, are considered and presented in Figure 5.8. For $\mathcal{L} = b$, the kinetic energy fluctuates around the same value for the three geometries. For this case, which we considered in the previous sections, the value of the scalar in the elliptical geometries is larger than that observed in the circular one. On the other hand, for $\mathcal{L} = \sqrt{ab}$, the kinetic energy fluctuates around the same value in the elliptical cases, and it is slightly larger than the one of the circular case. While the evolution of kinetic energy is close in cases 1 and 2, the evolution of the scalar shows a drastic change. Furthermore, the mean of the scalar value for the elliptical cases decreases, to reach the same value of the circular case for $a = 1.2$, and a smaller value for $a = 1.4$.

5.5 On the influence of the pinch on the dynamics

It seems from our results that changing the geometry, for given current and toroidal magnetic field, will lead to a self-organized state with a different level of magnetic fluctuations. We have carried out supplementary computations in which we increased the axial magnetic field for the circular geometry, thereby lowering the initial pinch by a factor 1.75. The increased stability in this case led to a lower level of magnetic fluctuations. However, even in this case in which the turbulent magnetic activity was of the level of the elliptic case (with $a = 1.2$) the safety factor remained roughly unchanged, and so did the diffusion. It seems thus that a change in the geometry affects the self-organized state with respect to the safety factor and diffusion, and that this result persists even when the initial pinch ratio is significantly changed. The details are given in the following.

The new case corresponds to a circular RFP with $B_z = 0.35$ instead of $B_z = 0.2$, as in previous simulations. The results are represented in magenta in the following figures. Figure 5.9 shows that the magnetic energy of the new case relaxes towards a state close to the elliptical case. On the other hand, as shown in figure 5.9, and calculated at instant $t \approx 3000\tau_A$, the q-profile of the new case is closer to the previous circular case, and the value of $< T >$ also remains close to its old value.

5.6 Conclusion

Direct numerical simulations of viscoresistive MHD show that in periodic cylindrical geometry in the RFP regime, the shape of the cross-section significantly changes the nonlinear dynamics. Moreover, different helical states can be observed and different energetic modes are excited in different geometries. Modifying the elliptical elongation leads to different modal behaviors. We quantified the impact on the confinement properties by considering the radial advection of a passive scalar, injected in the center of the domain. Indeed, the

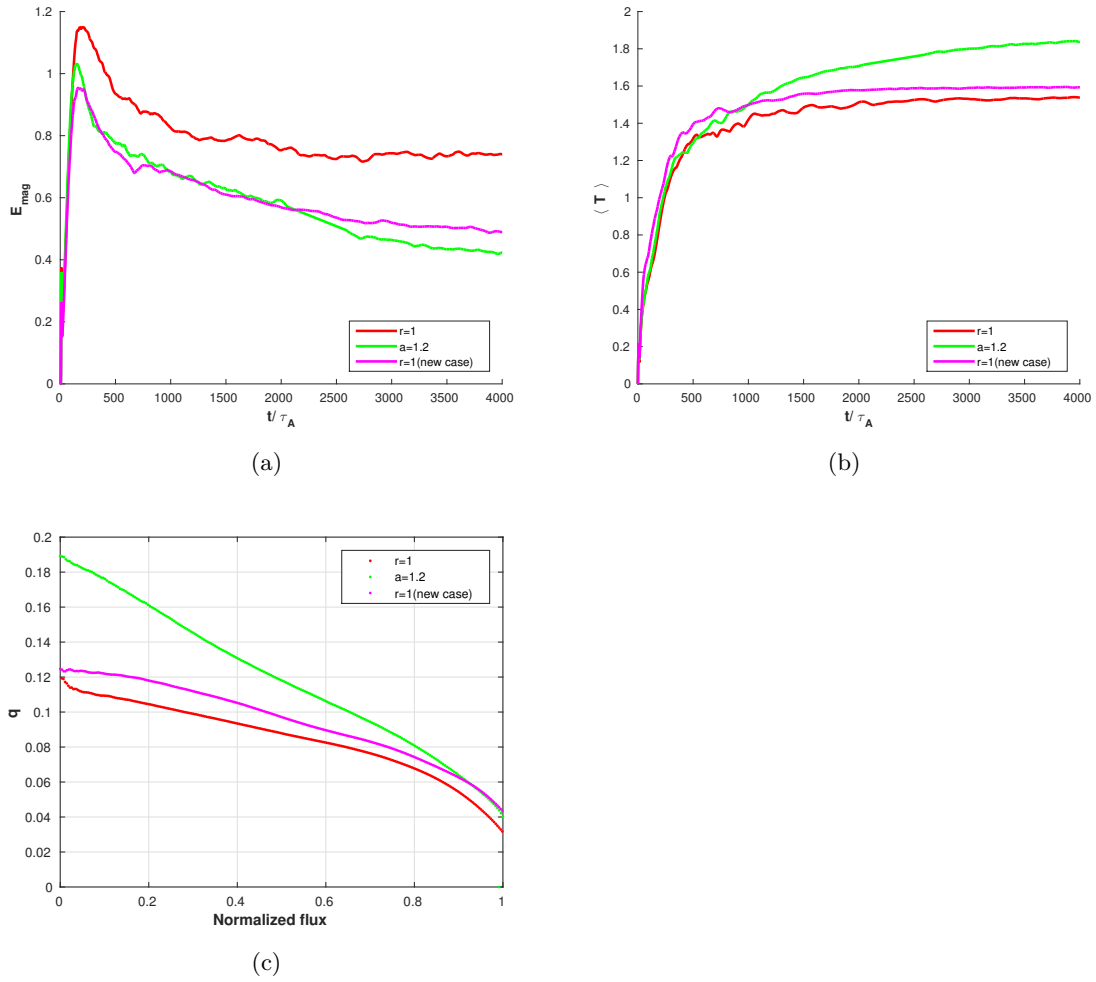

Figure 5.9: a) Evolution of the magnetic energy for the 3 cases. (b) Evolution of the mean of temperature for the 3 cases. (c) q-profile function of the flux, for the three cases, at $t = 3000\tau_A$.

evaluation of the eddy-diffusivity shows a clear enhancement of the confinement quality for elliptic cross-sections.

The physical reason why elongation could enhance confinement deserves certainly further investigation.

One possibility is that changing the geometry, for given current and toroidal magnetic field, will lead to a self-organized state with a different level of magnetic fluctuations. We have

carried out supplementary computations in which we increased the axial magnetic field for the circular geometry, thereby lowering the initial pinch by a factor 1.75. The increased stability in this case led to a lower level of magnetic fluctuations. However, even in this case in which the turbulent magnetic activity was of the level of the elliptic case (with $a = 1.2$) the safety factor remained roughly unchanged, and so did the diffusion. It seems thus that a change in the geometry affects the self-organized state with respect to the safety factor and diffusion, and that this result persists even when the initial pinch ratio is significantly changed.

Another possibility is that elongation leads to symmetry breaking of the poloidal flow. Indeed in 2D turbulence, changing the flow-geometry from circular to elliptical, leads to the generation of angular momentum [72]. This effect was shown to persist in 2D MHD turbulence [73] and its investigation is considered an interesting perspective, since large scale poloidal motion could enhance radial transport barriers. A preliminary investigation of this effect is shown in Fig 5.10 where for a given time-instant the angular momentum associated with the poloidal flow is computed for each cross-section. Even though the total volume averaged angular momentum might be small, it is shown that for the case of the circular geometry, locally large values of the poloidal angular momentum exist.

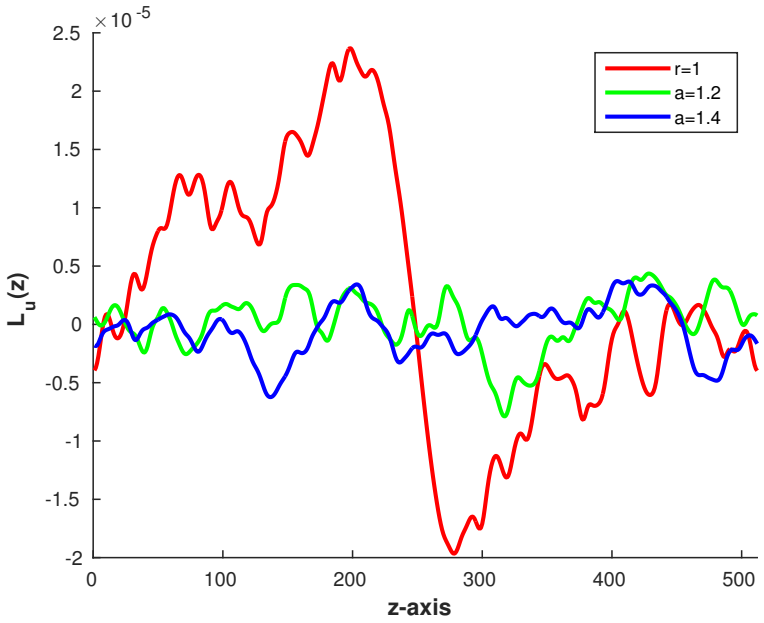

Figure 5.10: z-dependence of the instantaneous poloidal angular momentum for the three geometries at $t = 11 \times 10^3 \tau_A$.

The most important message of this work is perhaps not the knowledge of a certain value of the elongation, most efficient to obtain an optimal confinement, but the mere fact that elongation can change the confinement of RFPs. We would therefore encourage experimentalists to consider the poloidal shape of the confining magnetic field as an important control parameter for RFP design and operation. If an experiment allows for a simple modification of the plasma shape, it might give more freedom to obtain a competitive fusion plasma.

Chapter 6

Observation of the dynamo effect in an RFP

6.1 Introduction

The dynamo effect is the generation and sustainment of a magnetic field resulting from the motion of an electrically conducting fluid. It plays a major role in the description of the generation of celestial and planetary magnetic fields, such as the terrestrial one, generated by the movement of the liquid metal core.

Analytically, the amplification of the magnetic field takes place when the inductive term dominates over the resistive term of the induction equation,

$$\frac{\partial \boldsymbol{B}}{\partial t} = \underbrace{\nabla \times (\boldsymbol{u} \times \boldsymbol{B})}_{inductive\ term} + \underbrace{\lambda \nabla^2 \boldsymbol{B}}_{resistive\ term} . \tag{6.1}$$

The imbalance between these terms is quantified by the magnetic Reynolds number R_m, which gives an order of magnitude estimate of the ratio of the inductive term over the resistive term,

$$R_m = \mathcal{O}\Big(\frac{|\nabla \times (\boldsymbol{u} \times \boldsymbol{B})|}{|\lambda \nabla^2 \boldsymbol{B}|}\Big) = \frac{U\mathcal{L}}{\lambda}, \tag{6.2}$$

where U and $\mathcal{L}$ are reference velocity and length scales, respectively. A simple way to detect dynamo action corresponds to the observation of a positive time derivative of the magnetic energy E_m over a considerable time-interval. The equation of evolution of E_m is

obtained by multiplying equation (6.1) by $\boldsymbol{B}$ and integrating over the volume,

$$\frac{\partial E_m}{\partial t} = \underbrace{\int (\nabla \times \boldsymbol{B}) \cdot (\boldsymbol{u} \times \boldsymbol{B}) dv}_{production\ term} \quad - \quad \underbrace{\lambda \int |\nabla \times \boldsymbol{B}|^2 \, dv}_{Joule\ dissipation}. \tag{6.3}$$

So the dynamo effect is observed when the production term in equation (6.3) is greater than the Joule dissipative term.

A critical magnetic Reynolds number R_{mc}, below which no dynamo exists, can be calculated analytically in the case of prescribed flows [74–77]. This is called the kinematic dynamo, and it is used to study flows where the magnetic fluctuations are small so that the Lorentz force retroaction can be neglected. The governing equations in the kinematic dynamo regime are,

$$\frac{\partial \boldsymbol{u}}{\partial t} + \boldsymbol{u} \cdot \nabla \boldsymbol{u} = -\nabla P + \nu \nabla^2 \boldsymbol{u}, \tag{6.4}$$

and

$$\frac{\partial \boldsymbol{B}}{\partial t} = \nabla \times (\boldsymbol{u} \times \boldsymbol{B}) + \lambda \nabla^2 \boldsymbol{B}. \tag{6.5}$$

When the Lorentz force rectroaction is important and cannot be neglected anymore, the dynamics are governed by the saturated dynamo which can be described by the following equations,

$$\frac{\partial \boldsymbol{u}}{\partial t} + \boldsymbol{u} \cdot \nabla \boldsymbol{u} = -\nabla P + \nu \nabla^2 \boldsymbol{u} + \boldsymbol{J} \times \boldsymbol{B}, \tag{6.6}$$

and

$$\frac{\partial \boldsymbol{B}}{\partial t} = \nabla \times (\boldsymbol{u} \times \boldsymbol{B}) + \lambda \nabla^2 \boldsymbol{B}. \tag{6.7}$$

The only difference is thus the presence of the Lorentz force, which allows the magnetic field to react back on the velocity field by which it is stretched and advected.

It has been shown using kinematic dynamo theory that geometrical constraints apply on the flow and therefore not any flow can trigger dynamo action no matter the value of R_m. For example, 2D flows and planar flows are unable to generate a dynamo field. Another example is Cowling's theorem [78] which mentions that axisymmetric magnetic fields cannot be maintained by the dynamo action, i.e. a dynamo with axisymmetric magnetic field is impossible. It was shown by Moffatt [79] that helicity is beneficial for the amplification of a seed magnetic field. Indeed helicity allows the simultaneous stretching and twisting of magnetic field lines. The helical character of an RFP flow field should therefore be a good candidate to amplify a magnetic field. Indeed, previous investigations of screw-flow in a toroidal domain, quite similar in shape to the RFP flow demonstrated the possibility of dynamo activity [80, 81].

In turbulent flows, classically the mean field theory is proposed to study the dynamo effect. It consists in applying Reynolds' decomposition to write the total velocity and

magnetic fields as the sum of the ensemble average (overlined quantities) of the field and its fluctuation (primed quantities),

$$\boldsymbol{u} = \overline{\boldsymbol{u}} + \boldsymbol{u}', \qquad \boldsymbol{B} = \overline{\boldsymbol{B}} + \boldsymbol{B}', \tag{6.8}$$

and then deriving their evolution equations. The mean field induction equation can then be written as:

$$\frac{\partial \overline{\boldsymbol{B}}}{\partial t} = \nabla \times (\overline{\boldsymbol{u}} \times \overline{\boldsymbol{B}}) + \nabla \times \underbrace{(\overline{\boldsymbol{u}' \times \boldsymbol{B}'})}_{e.m.f} + \lambda \nabla^2 \overline{\boldsymbol{B}}. \tag{6.9}$$

The mean field theory focuses on modelling the electromotive force (e.m.f) arising from the turbulence which is commonly written as,

$$\overline{\boldsymbol{u}' \times \boldsymbol{B}'} = \alpha \overline{\boldsymbol{B}} - \beta \overline{\boldsymbol{J}}. \tag{6.10}$$

where α corresponds to the e.m.f generated by the turbulence in the direction along the mean field and β to the one along the mean current field. While this model yields simple dynamo solutions and links the dynamo effect to the magnetic helicity $\boldsymbol{H}_m$ [82], its validity is however limited [83].

The more classical approach, where the amplification of a magnetic field is studied in well defined analytical flows containing helicity is now more and more replaced by the study of fully turbulent flows. This is already illustrated by the most famous dynamo experiments where the first dynamos were observed in a well-controlled laminar flow, and where later experiments aimed at observing a dynamo in a turbulent setting. These experiments are discussed now.

The first dynamo action in a fluid was observed in 2000 at the Riga [84, 85] and Karlsruhe [86] facilities. In the Riga experiment, a propeller is driven to produce a single-vortex-like helical flow in a bath of liquid sodium initially at rest. The self-excitation of a slowly growing magnetic field eigenmode with a growth rate $p \approx 0.0315\ s^{-1}$ was detected at propeller's rotation rate 2150 rpm. The Karlsruhe experiment consisted of 52 tubes assembled in series which generated alternated helical flow, i.e, the rotation and translation's sign changes between a tube and another. A smooth increase of two components of the magnetic field was observed, thereby demonstrating the presence of dynamo-activity producing a mean magnetic field of the order of $40 - 60\ Ga$. This experiment is based on the G.O Roberts kinematic dynamo [77] while the Riga's experiment is based on the Ponomarenko kinematic dynamo [76].

The results of these two experiments motivated the dynamo community to design an experiment with less geometrical flow constraints, more complex dynamics and strong turbulence. This might result in the generation of a more complicated magnetic field than the stationary magnetic field in Karlsruhe and the periodic one in Riga. This was achieved by the von Kármán Sodium (VKS) experiment [87–89] where two counter-rotating impellers generated

the sodium flow in a cylinder. Such flow, characterized by intense turbulence and non-zero helicity, is believed to favor the dynamo action [79]. The dynamo effect observed in this experiment exhibited interesting dynamics where the magnetic field polarity changed sign quasi-periodically. This result was previously observed in the numerical simulations of the terrestrial magnetic field reversal carried out by Glatzmaier and Roberts [90]. Further numerical observations of dynamo action were reported in a number of papers, for instance [91] where the limit of small magnetic Prandtl number was considered in Large Eddy Simulations (LES) of the MHD equations.

In RFP fusion reactors, it is known that increasing the toroidal current I_z above a certain threshold for a given toroidal magnetic field B_z gives in general rise to a complex chaotic interplay of helical structures of different spatial frequency, reorganizing the plasma into a stable state where the toroidal component reverses close to the boundary. The generation of this toroidal magnetic field, which has the originally imposed sign in the center and reversed close to the boundary, is referred to as the dynamo effect in the fusion community. It was pointed out by Caramana [92] that this term is "*borrowed*" from astrophysics, and later by Escande [5] that it should be called "*half a dynamo*" since an externally imposed e.m.f drives the toroidal current. Indeed, an obvious difference of the RFP phenomenology compared to the astrophysical definition of a dynamo, is that in the latter case one considers the amplification of an infinitesimally small seed-magnetic field, whereas in the RFP context one considers the modification of an initially strong imposed magnetic field.

The reversal phenomenon in RFPs, which is believed to be linked to the dynamo effect, was observed first in early RFP experiments [92–94] and extensively studied using different approaches. In [95] the parallel Ohm's law was used to point out the diamagnetic effect, while in [96] mean field theory was used and the α-model was invoked to explain the RFP reversal. It was also pointed out in [97] that cross-helicity plays a major role in the RFP dynamo. After the observation of quasi-single-helicity states in [7] in 2000, the dominant electrostatic nature of the RFP dynamo was illustrated in [98, 99].

In this chapter we carry out a thought experiment where we extract the self-consistent velocity field computed from the coupled set of equations presented in Chapter 3, and analyse its dynamo capability. We hereby reconcile the astrophysics and fusion community with respect to the presence, or not, of a dynamo in RFPs. We consider the interaction of three vector-fields (as in [100]): the velocity field $\boldsymbol{u}$, generated by an MHD instability resulting from its interaction with the magnetic field $\boldsymbol{B}$, and an initially weak magnetic field $\boldsymbol{D}$, passively advected by the velocity field $\boldsymbol{u}$. Results will show that the RFP velocity field acts as a dynamo, for sufficiently large magnetic Reynolds numbers.

6.2 Governing MHD equations

The RFP velocity field $\boldsymbol{u}$ is generated by the MHD instability resulting from its interaction with the RFP magnetic field $\boldsymbol{B}$. This is done similarly in Chapter 4 by resolving the visco-resistive MHD equations (3.1) and (3.2),

$$\frac{\partial \boldsymbol{u}}{\partial t} = -\nabla \Pi + \boldsymbol{u} \times \boldsymbol{\omega} + \boldsymbol{j} \times \boldsymbol{B} + \nu \nabla^2 \boldsymbol{u}, \tag{6.11}$$

and

$$\frac{\partial \boldsymbol{B}}{\partial t} = \nabla \times (\boldsymbol{u} \times \boldsymbol{B}) + \lambda \nabla^2 \boldsymbol{B}. \tag{6.12}$$

The passive magnetic field's evolution is described by the following induction equation,

$$\frac{\partial \boldsymbol{D}}{\partial t} = \nabla \times (\boldsymbol{u} \times \boldsymbol{D}) + \lambda' \nabla^2 \boldsymbol{D}, \tag{6.13}$$

where λ' is the magnetic diffusivity corresponding to $\boldsymbol{D}$. The velocity field $\boldsymbol{u}$, the magnetic field $\boldsymbol{B}$ and the passive magnetic field $\boldsymbol{D}$ are all divergence free,

$$\boldsymbol{\nabla} \cdot \boldsymbol{u} = 0, \quad \boldsymbol{\nabla} \cdot \boldsymbol{B} = 0 \quad \text{and} \quad \boldsymbol{\nabla} \cdot \boldsymbol{D} = 0. \tag{6.14}$$

In the remainder of the Chapter, all quantities related to the passive magnetic field $\boldsymbol{D}$ are primed in order to avoid any confusion with quantities related to $\boldsymbol{B}$, e.g, $R_m = U\mathcal{L}/\lambda$ while $R'_m = U\mathcal{L}/\lambda'$. Here and in the following U is the RMS value of the velocity field averaged over the volume of the cylinder, and $\mathcal{L}$ is the diameter of the cylinder. Furthermore, unless stated otherwise, the Prandtl number $P_m = \nu/\lambda$ is considered unity, and hence $Re = R_m$ in this case.

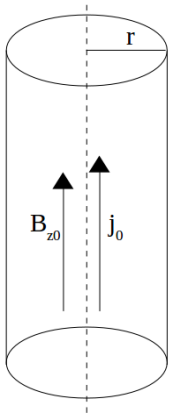

Figure 6.1: Sketch of the cylindrical geometry.

The difference between $\boldsymbol{B}$ and $\boldsymbol{D}$ is that the former interacts with the velocity field, whereas the latter is passively advected and stretched. Another difference is that the initial passive magnetic field $\boldsymbol{D}$ is a random noise similar to the velocity field, but with initial energy $E_D \approx 10^{-10}$. The initial magnetic field is, as in the foregoing chapters the combination of an axial field $B_{z0} = 0.2$ and a poloidal field B_{p0} induced by an imposed axial current density $j_{z0} = 1.4$. At the boundary, no slip condition is imposed for the velocity field, while for $\boldsymbol{B}$ and $\boldsymbol{D}$ only the poloidal component is set to zero.

Two numerical simulation set-ups are considered: the first one corresponds to a "frozen" velocity field and the second one to a "dynamic" velocity field. The first case consists in using in equation (6.13) a time-invariant velocity field obtained by resolving first, equations (6.11) and (6.12) until reaching a statistically stationary state.

Such a method is suitable for laminar flows with small Lundquist number $S = C_A\mathcal{L}/\lambda$, where few kinetic modes dominate, and dynamo action is more probable due to lack of kinetic fluctuations. In the second case, equations (6.11), (6.12) and (6.13) are resolved simultaneously. This method is suitable for flows with high Lundquist number exhibiting turbulent dynamics.

In the previous chapters we characterized the influence of the viscosity and magnetic diffusivity by a control parameter, the Lundquist number S, but in the dynamo-community one considers the Reynolds number Re instead. Since Re is an output parameter that cannot be directly imposed, we first quantify in Figure 6.2 the Reynolds number as a function the Lundquist number in our simulations. In order to vary the Lundquist number, and thereby the Reynolds number, only the kinematic viscosity ν is varied while the imposed magnetic and current fields are kept the same as previously mentionned in this section. Similarly, the passive magnetic Reynolds number R'_m is varied for each flow by only changing the value of λ'.

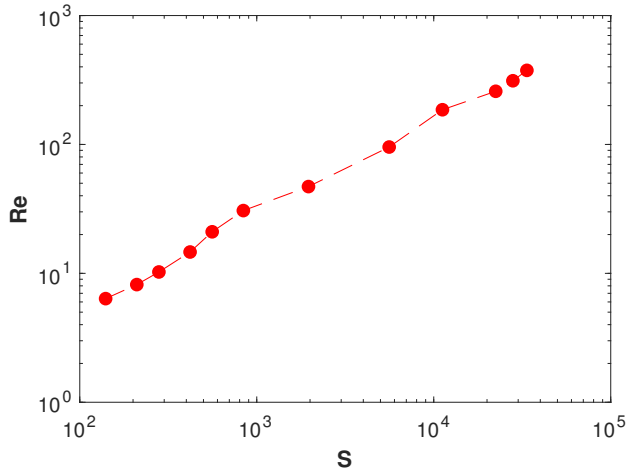

Figure 6.2: Reynolds number Re as a function of the Lundquist number S.

6.3 Dynamo generated by a laminar RFP velocity field

In this section, dynamo action in laminar RFP flows are studied using kinematic dynamo theory. This choice is justified by the fact that laminar flows can be considered as prescribed and quasi-time invariant. Furthermore, the passive magnetic field has no retroaction on the velocity field.

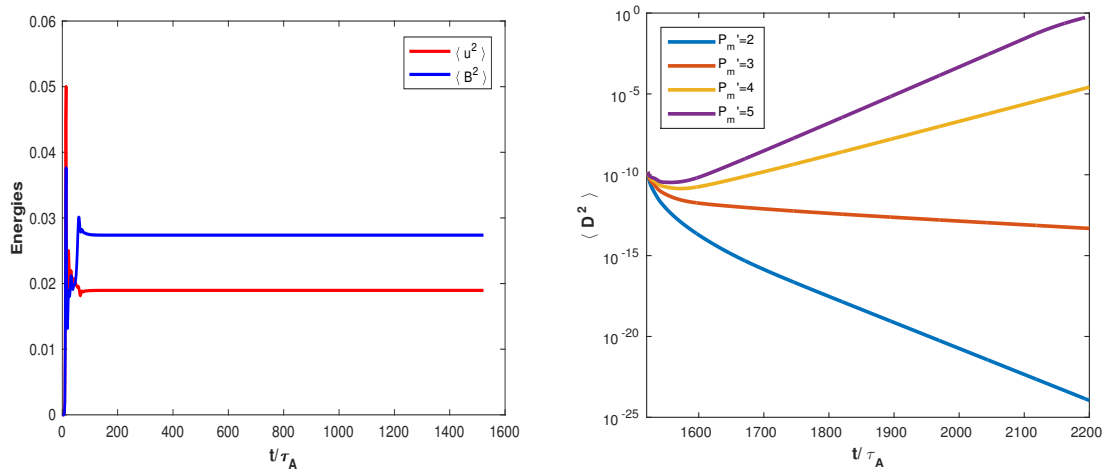

(a) (b)

Figure 6.3: Time evolution of: (a) the kinetic and magnetic energies, (b) the passive magnetic energy for different values of P'_m of a flow with $Re = 10$.

6.3.1 Is the RFP velocity field a dynamo?

The ability of an RFP velocity field to amplify an initially weak magnetic field by dynamo action is checked in this section. It consists in using the first simulation setup where the velocity field is frozen. Thereto, equations (6.11) and (6.12) are solved until the kinetic energy $E_k = \frac{1}{2}\langle \boldsymbol{u}^2 \rangle$ and magnetic energy $E_B = \frac{1}{2}\langle \boldsymbol{B}^2 \rangle$ reach a statistically stationary state as shown in Figure 6.3(a). Then the frozen velocity field is taken at $t = 1500\tau_A$ where the flow's Reynolds number is $Re = 10$, and simulations of equation (6.13) for different values of λ' are carried out in order to check the critical Reynolds number R'_{mc} or the critical Prandtl number $P'_{mc} = R'_{mc}/Re$. In Figure 6.3(b), the passive magnetic energy $E_D = \frac{1}{2}\langle \boldsymbol{D}^2 \rangle$ is amplified for $P'_m > 3$ and therefore proves the existence of dynamo action in RFP at least in the laminar, kinematic case.

6.3.2 Dynamo growth rate

In kinematic dynamo theory, the passive magnetic field has no retroaction on the velocity field which makes the induction equation linear in $\boldsymbol{D}$. In consequence, its solution can be written as,

$$\boldsymbol{D}(\boldsymbol{x}, t) = \boldsymbol{D}_0(\boldsymbol{x}) e^{p' t}, \tag{6.15}$$

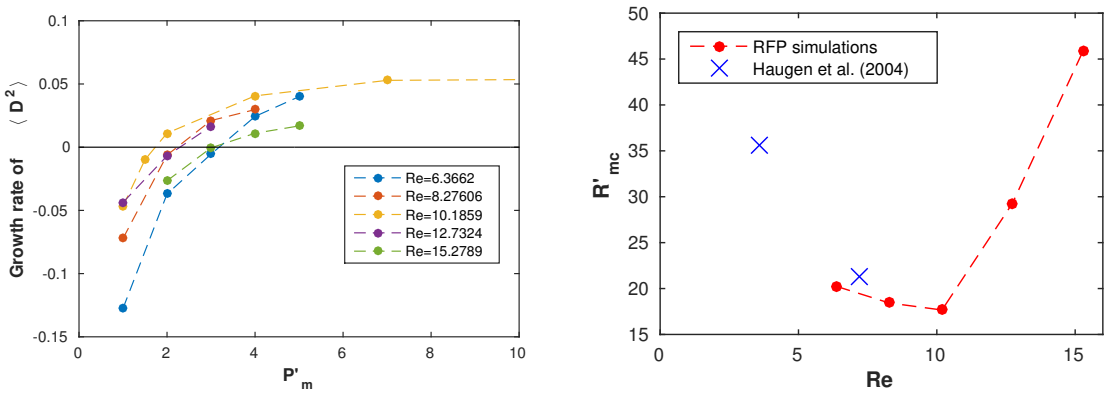

(a) (b)

Figure 6.4: (a) Growth rate of $\langle D^2 \rangle$ for different values of Re and P'_m, (b) critical magnetic Reynolds number R'_{mc} function of Reynolds number Re.

where p' is the growth rate. Hence, passive magnetic energy is expected to have exponential growth, which can be seen clearly in Figure 6.3(b). Simulations with different values of Re and P'_m are carried out, and the corresponding growth rate values are plotted in Figure 6.4(a). The critical Reynolds number R'_{mc} which corresponds to zero growth rate is calculated by interpolating the different growth rate values of each flow, and are represented in Figure 6.4(b). It is observed that the value of the critical Reynolds number is of the order 18 for $Re \leq 10$, then it fastly increases for the range of $10 < Re < 16$. We also show in this range the simulation results carried out in reference [101], where the dynamo action is studied in a periodic flow with non-helical forcing.

A first observation is that these results match well with our RFP simulations, which shows that RFP flows are suitable for dynamo studies. Indeed, the critical value of the magnetic Reynolds number is of the same order of magnitude as those observed in flows which were specifically designed to generate a dynamo [102,103]. This illustrates that the RFP flow has very favorable properties for dynamo generation. This can be qualitatively understood since RFP flows are characterized by high helicity and high shear, two properties which enhance dynamo activity. We can anticipate that once the flow becomes turbulent, dynamo activity will be harder to obtain. This was illustrated, for example, in [91] where low magnetic Prandtl number regimes have been studied using Taylor-Green forcing. Furthermore, their results show that the critical magnetic Reynolds number increases sharply with the decrease of the magnetic Prandtl number.

6.3.3 Interaction between u and D

The passive magnetic field is amplified by the motion of the conducting fluid. It is not clear to what extent it can be expected that $\boldsymbol{D}$ presents a similar structure as the velocity field. The comparison of the modal and geometrical structure of $\boldsymbol{u}$ and $\boldsymbol{D}$ is investigated in this section.

We consider first the induction equation of $\boldsymbol{D}$, written using indices to simplify the analysis,

$$\frac{\partial \boldsymbol{D}(\boldsymbol{x},t)}{\partial t} = \nabla \times (\boldsymbol{u} \times \boldsymbol{D}) + \lambda \nabla^2 \boldsymbol{D}. \tag{6.16}$$

Taking the Fourier transform of equation (6.16) and using Levi-Civita notation leads to the following equation,

$$\frac{\partial \widehat{D_j}(\boldsymbol{k},t)}{\partial t} = \varepsilon_{jab} i k_a (\varepsilon_{bcd} \widehat{u_c D_d}) - \lambda k^2 \widehat{D_j}. \tag{6.17}$$

The Fourier transform of the product $u_c D_d$ is a convolution that can be written as,

$$\begin{aligned} \widehat{u_c D_d}(\boldsymbol{k}) = \int_{-\infty}^{\infty} u_c(\boldsymbol{p}) D_d(\boldsymbol{k}-\boldsymbol{p}) d\boldsymbol{p} &= \int_{-\infty}^{\infty} u_c(\boldsymbol{p}) \int_{-\infty}^{\infty} D_d(\boldsymbol{q}) \delta(\boldsymbol{k}-\boldsymbol{p}-\boldsymbol{q}) d\boldsymbol{q} d\boldsymbol{p} \\ &= \iint_{-\infty}^{\infty} \delta(\boldsymbol{k}-\boldsymbol{p}-\boldsymbol{q}) u_c(\boldsymbol{p}) D_d(\boldsymbol{q}) d\boldsymbol{q} d\boldsymbol{p}. \end{aligned} \tag{6.18}$$

In consequence, the induction term exists under the condition

$$\boldsymbol{k} - \boldsymbol{p} - \boldsymbol{q} = \boldsymbol{0}, \tag{6.19}$$

which can be written similarly for the axial components,

$$k_z - p_z - q_z = 0. \tag{6.20}$$

Hence the generation of a passive magnetic field resulting from the interaction of the velocity field and the initial passive magnetic field is expected to have axial modes $n = k_z$ equal to the sum of the dominant kinetic axial mode p_z and the initial dominant passive magnetic axial mode q_z. In order to check this, numerical simulations of flows with $P'_m = 4$ and $Re = 6.37, 10.2, 15.3$ are carried out and the plot of different normalized axial energy spectra is shown in Figure 6.5 for toroidal modes $n \leq 40$. This choice is justified in Figure 6.6 where these axial spectra are plotted for all toroidal modes in log-scale. The spiky pattern of the spectra is generated by the harmonics of the dominating mode, a common modal behaviour for laminar flows, and the dominating modes are in the range of $n < 40$. In the case of $Re = 10$, the dominant kinetic axial mode is $|\boldsymbol{p}_z| = 9$ and the passive magnetic one is $|\boldsymbol{q}_z| = 2$. If one assumes that the previous reasoning is correct, then the interaction of $|\boldsymbol{p}_z| = 9$ and $|\boldsymbol{q}_z| = 2$ would generate $|\boldsymbol{k}_z| = 11$ ($\boldsymbol{p}_z$ and $\boldsymbol{q}_z$ have the same

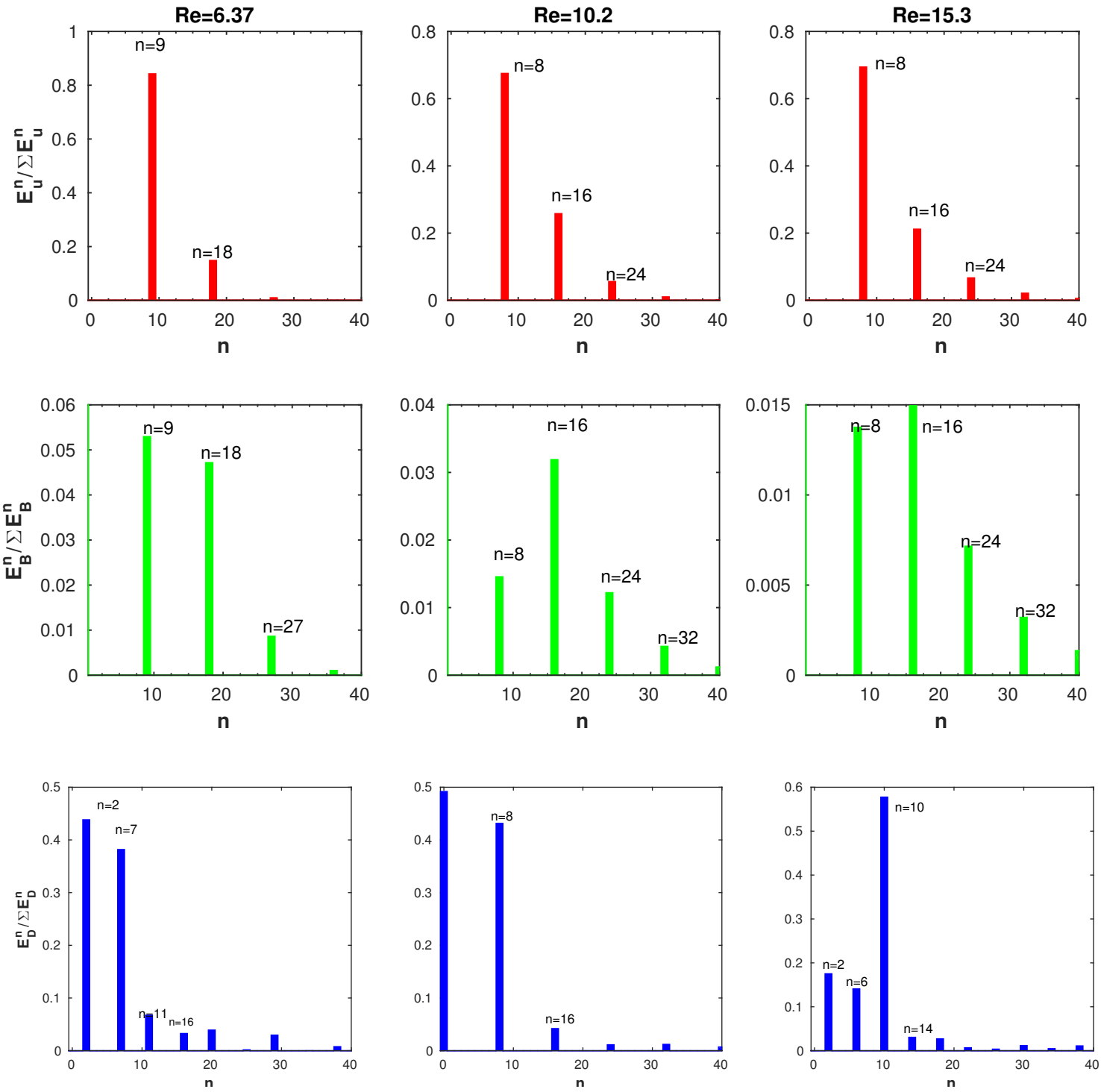

Figure 6.5: Axial spectra of u^2 (red), B^2 (green) and D^2 (blue) for different values of Re and for $P'_m = 4$.

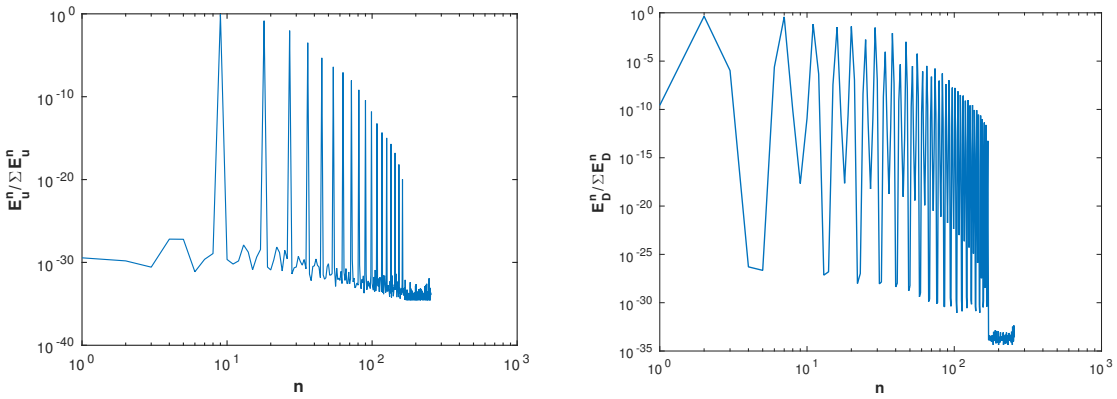

(a) (b)

Figure 6.6: Normalized axial spectra of (a) u^2, (b) D^2 in log-scale for $Re = 6.37$ and $P'_m = 4$.

sign) and $|\boldsymbol{k}_z| = 7$ ($\boldsymbol{p}_z$ and $\boldsymbol{q}_z$ have opposite signs). This expected result is consistent with the axial spectra of D^2 shown in Figure 6.5, and is also observed for the flows with $Re = 16$ and $Re = 24$.

Furthermore, this interaction is expected to stay unchanged for flows with the same Re (i.e, same ν) and different P'_m, as long as the resistive term, which can be written as $(\nu/P'_m)(\nabla^2 \boldsymbol{D})$, is negligible compared to the induction term. This is shown in Figures 6.7 and 6.8 where the modal structure of D^2 stays unchanged for the case of $Re = 10$ and $Re = 16$ with different values of P'_m. The same behaviour is observed in the case of $Re = 24$ but is not reported here.

Now we will explore the $\boldsymbol{u} - \boldsymbol{D}$ interaction by analyzing the 3D visualization of different fields. Isosurfaces of the kinetic and passive magnetic energies normalized by their volume averages, $u^2/\langle u^2 \rangle$ and $D^2/\langle D^2 \rangle$ respectively, are shown in Figure 6.9. A first observation is that the velocity field and the passive magnetic field have a different spatial structure. Moreover, the kinetic structures occupy most of the central region of the cylinder, while most of the passive magnetic structures exist outside the central part. Another observation is that the different magnetic structures connect at the high shear region where the velocity gradient is large, i.e region between the red ($u_z > 0$) and violet ($u_z < 0$) kinetic structures. Furthermore, the axial component of these magnetic structures reverses sign after each connection.

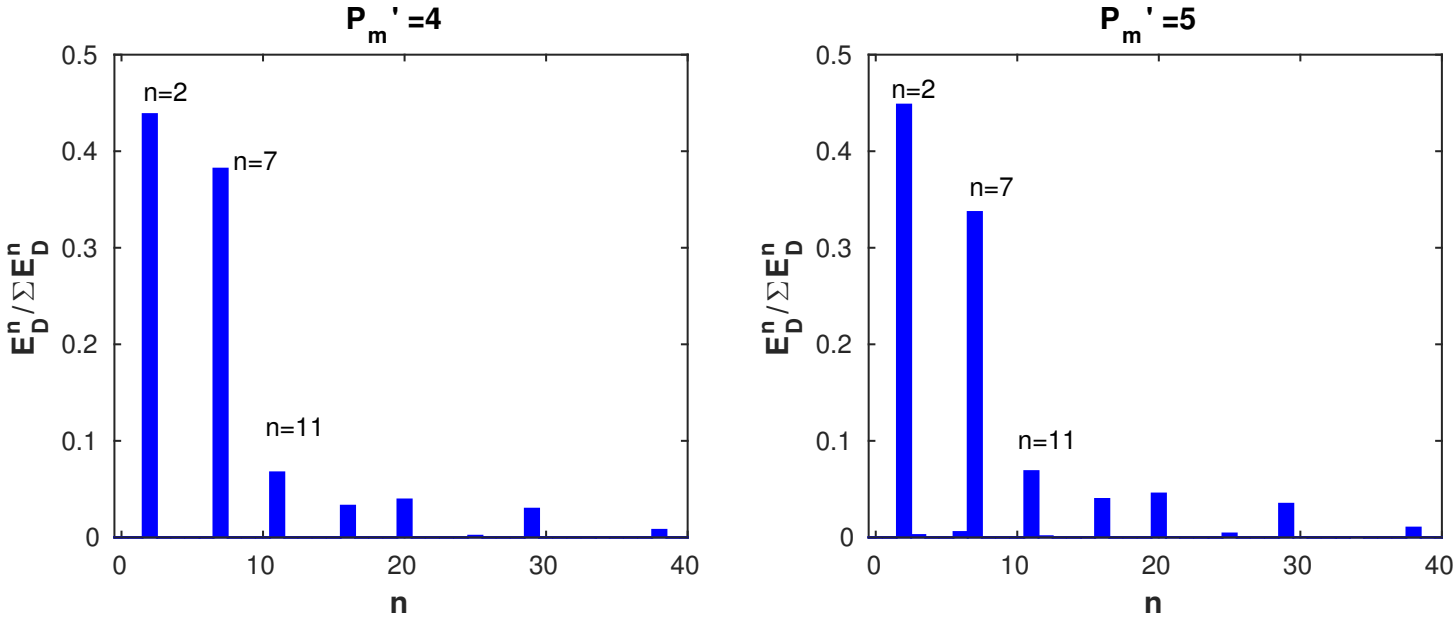

Figure 6.7: Axial spectra of D^2 for $Re = 6.37$ and different values of P'_m.

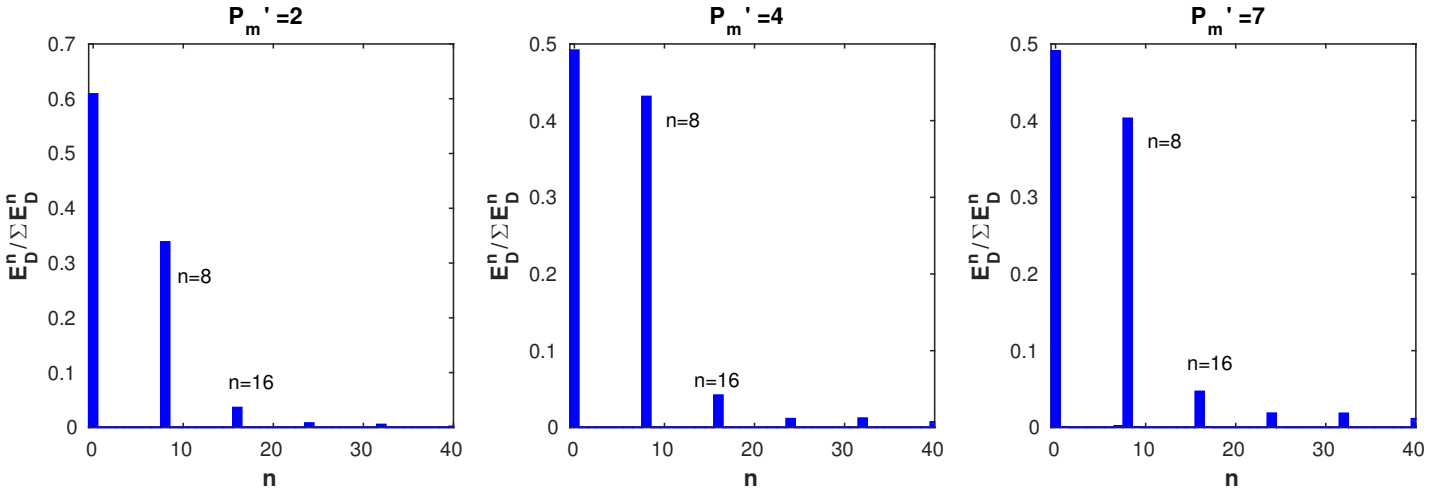

Figure 6.8: Axial spectra of D^2 for $Re = 10.2$ and different values of P'_m.

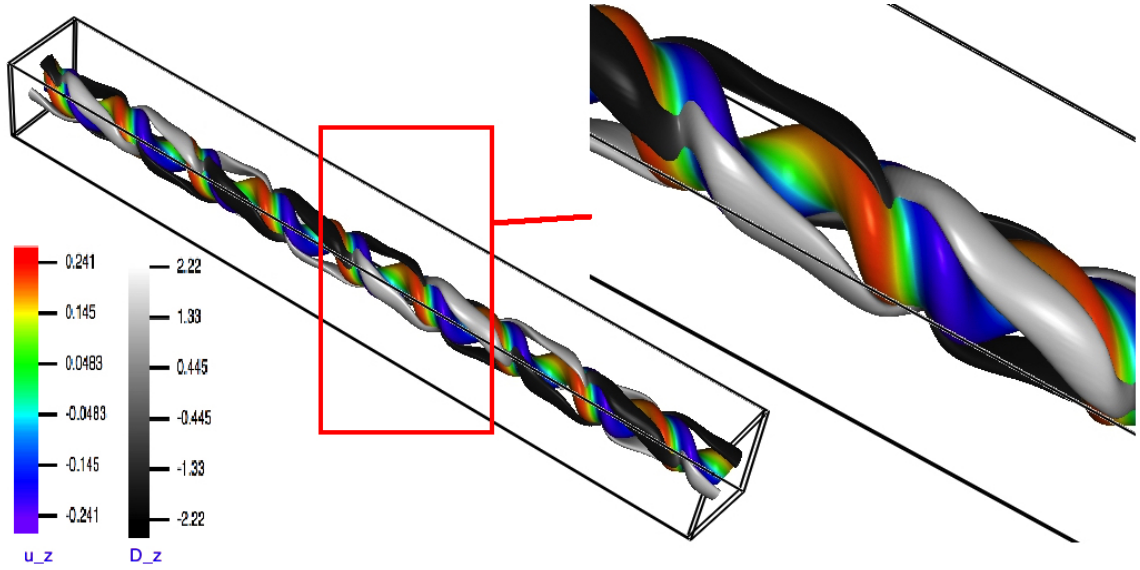

Figure 6.9: 3D visualization of the normalized kinetic energy isosurface $u^2/\langle u^2\rangle = 6.6$ and the normalized passive magnetic energy isosurface $D^2/\langle D^2\rangle = 9$, colored by the axial velocity field u_z and axial passive magnetic field D_z, respectively, for $Re = 6.37$ and $P'_m = 4$.

6.3.4 Influence of the boundary conditions

An important issue in dynamo computations is the precise nature of the boundary conditions, which can importantly influence the growth rate of the magnetic energy (even though the dynamo properties of some flows are surprisingly robust with respect to the choice of the boundary conditions [104]).

Influence of the radial periodicity As in the foregoing chapter, we have chosen the boundary conditions such that the axial component of the passive magnetic field D_z at the boundary can evolve freely without any constraint. If the cylinder's boundaries are close to the computational domain boundaries, the periodicity of the spectral methods might affect the evolution of D_z in the wall, which subsequently would change the evolution of $\boldsymbol{D}$ in the fluid domain. To check this, we compare two dynamo simulations where the cylinder's radius is kept $r = 1$ and the domains are modified for $Re = 8.27$, $P'_m = 4$. The first one is carried out in a box of size $\pi \times \pi \times 8\pi$ while the second in a box of size $2\pi \times 2\pi \times 8\pi$. Thus, the domain in the second case where $\boldsymbol{D}$ evolves freely is larger than the one in the first case. It is shown in Figure 6.10 that the growth rate of the passive magnetic energy has slightly increased from 0.0297 in the first domain to 0.0353 in the larger domain. However, qualitatively no important modification are observed in the

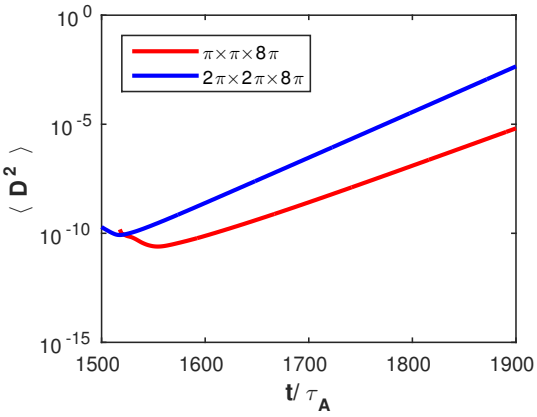

Figure 6.10: Time evolution of (a) kinetic energy, (b) passive magnetic energy, for a flow with $Re = 8.27$ and $P'_m = 4$ and different domains.

spatial structure of passive magnetic field as shown in Figure 6.11. Furthermore, this can be confirmed in Figure 6.12 where the axial spectra of the kinetic and passive magnetic energies in different computational domains remain almost unchanged.

Influence of the axial periodicity Due to the need of a high numerical resolution to solve the turbulent dynamo regime, large computational resources are required. Hence, in the following the cylindrical domain is reduced to half its length in the z-direction in an attempt to reduce the computational requirements. This would correspond, if the cylinder would be bent into a torus, to a toroidal domain with a diameter divided by two.

To check this geometrical effect on the dynamo properties, simulation of flows with $Re = 8.27$ and $P'_m = 4; 5.3; 8$ are carried out in a domain of size $\pi \times \pi \times 4\pi$. It is shown in Figure 6.13 that the critical Prandtl number in the case of $Re = 8.27$ and a domain of size $\pi \times \pi \times 4\pi$ is $P'_{mc} > 4$, while in Figure 6.4(a) $1.8 < P'_{mc} < 3$ in the case of $Re = 8.27$ and a domain of size $\pi \times \pi \times 8\pi$. Hence, reducing the domain size in the z-direction might not be always beneficial because it increases the critical magnetic Prandtl in some ranges of Re. Apparently, the additional space in a longer domain promotes the dynamo effect.

Free magnetic boundary conditions As a last verification we consider the case where all the magnetic components are left free to evolve at the boundary of the cylinder. The only constraint on the magnetic field outside the cylinder is the periodicity on the boundary of the numerical domain. This domain is a rectangular box of size $2\pi \times 2\pi \times 8\pi$, whereas the diameter of the cylinder is 2. It is shown in Figure 6.14 that the dominating modes of the passive magnetic energy's axial spectra remain unchanged in both cases while the

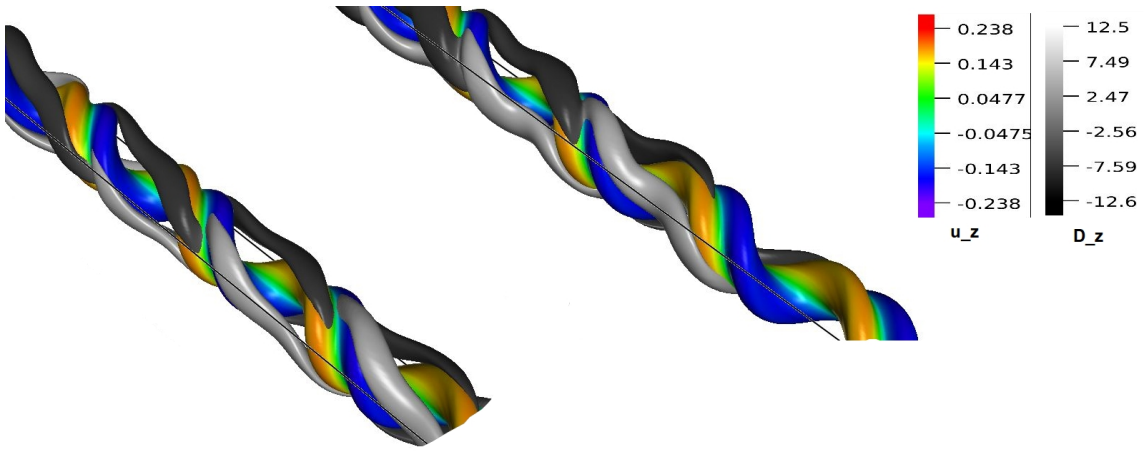

Figure 6.11: 3D visualization of the normalized kinetic energy isosurface $u^2/\langle u^2\rangle = 6.6$ and the normalized passive magnetic energy isosurface $D^2/\langle D^2\rangle = 9$, colored by the axial velocity field u_z and axial passive magnetic field D_z, respectively, with a domain of size (left) $\pi \times \pi \times 8\pi$, (right) $2\pi \times 2\pi \times 8\pi$, for $Re = 8.27$ and $P'_m = 4$.

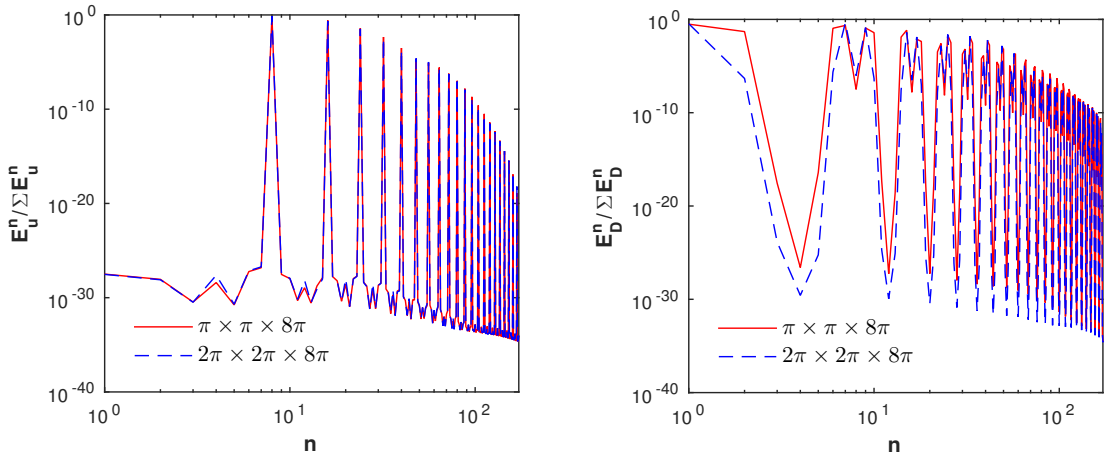

(a) (b)

Figure 6.12: Normalized axial spectra of (a) the kinetic and (b) the passive magnetic energies, for $Re = 8.27$ in different computational domains.

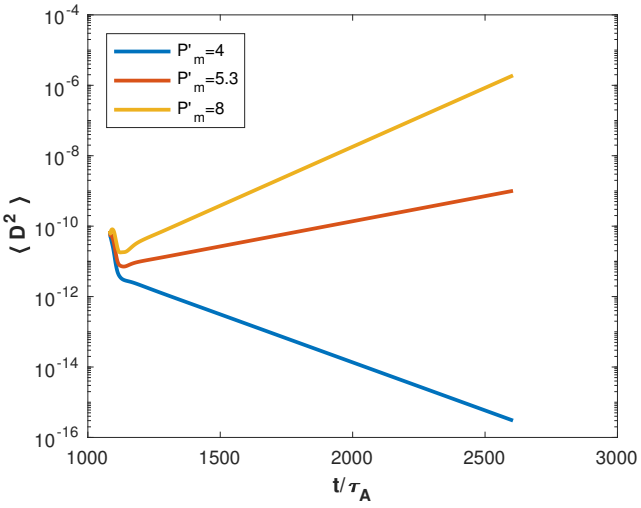

Figure 6.13: Time evolution of the mean passive magnetic energy in a domain of size $\pi \times \pi \times 4\pi$, for $Re = 8.27$ and different values of P'_m.

non-dominating ones in the case of free boundary conditions has grown larger than in the other case. However, the dominating modes are orders of magnitude larger (10^{10}) than the non-dominating modes, thus no clear changes in the dynamics are observed.

6.4 Turbulent dynamo

6.4.1 Numerical simulation of the turbulent dynamo

Simulations are now carried out for a flow in which all three fields $\boldsymbol{u}$ and $\boldsymbol{B}$ and $\boldsymbol{D}$ are evolving in time. Since in the previous chapter RFP simulations for $S \approx 25 \times 10^4$ (which corresponds to $Re = R_m \approx 434$) were well-resolved using $64 \times 64 \times 512$ grid points, the same numerical resolution is used ($64 \times 64 \times 512$) for $\boldsymbol{D}$. We carry out first simulations for a flow with $Re = R_m = 148$ and $R'_m = 295$. It is found that the resulting velocity field $\boldsymbol{u}$ and magnetic field $\boldsymbol{B}$ are well resolved, which is not the case for $\boldsymbol{D}$. To make sure that this difference is not due to the fact $Re < R'_m$, we carry out another simulation of a flow with $Re = R_m = 434$ using the same resolution ($64 \times 64 \times 512$) and compare the axial spectra of kinetic and magnetic energies of this flow with the one of the passive magnetic energy of the flow with $R'_m = 295$. This is shown in Figure 6.15(a). In the first flow, low wavenumbers contain most of the energy, which is not the case in the second flow where the energy is equi-distributed over all the wavenumbers. Such spectral behavior is

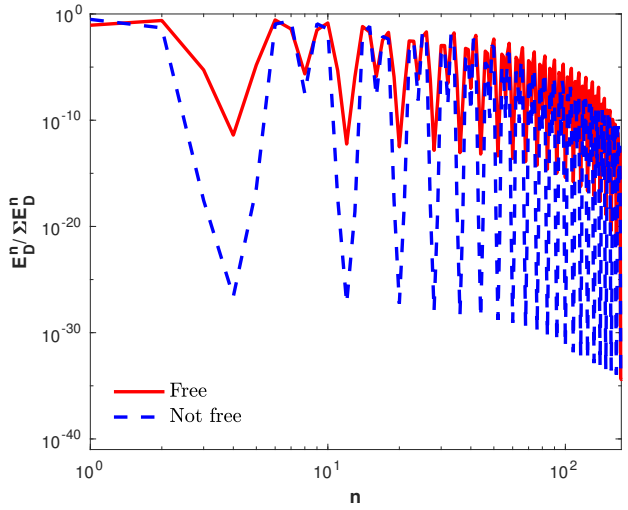

Figure 6.14: Normalized axial spectra of the passive magnetic energy for $Re = 8.27$ with different boundary conditions. The red curve corresponds to the case where all components of $\boldsymbol{D}$ evolve freely at the boundary, and blue to the case where the poloidal component D_p=0.

observed when the grid size of the simulation is not small enough to resolve the scales where the passive magnetic energy is diffused. To illustrate the change of modal behavior when the equations are well resolved, smaller R'_m and larger numerical resolution resolution are considered to make sure that $\boldsymbol{D}$ is well resolved. We show in Figure 6.15(b) the energy spectra of the velocity field $\boldsymbol{u}$ and magnetic field $\boldsymbol{B}$ of a flow with $Re = R_m = 51$ and of the passive magnetic field $\boldsymbol{D}$ of a second flow with $R'_m = 153$ using $128 \times 128 \times 512$ numerical resolution. Clearly, the energy in the three spectra is sufficiently dissipated at large wavenumbers, represented by a steeper dissipation range.

In conclusion, it seems that for a given resolution, when the field $\boldsymbol{B}$ is rather well resolved, the field $\boldsymbol{D}$ needs a finer resolution. At first sight this is rather surprising since the evolution-equation of $\boldsymbol{B}$ is identical to the evolution equation of $\boldsymbol{D}$. There must therefore be something going on in the coupling between the velocity-field and the magnetic field $\boldsymbol{B}$ through the Lorentz force, which prevents the magnetic field to generate the small scales observed in the passive $\boldsymbol{D}$ field. We will now attempt to give an explanation for that.

6.4.2 Saturation of the nonlinear dynamo

In the kinematic dynamo description, the passive magnetic field does not exhibit any Lorentz force $(\nabla \times \boldsymbol{D}) \times \boldsymbol{D}$ on the plasma. This case was investigated in reference [100]

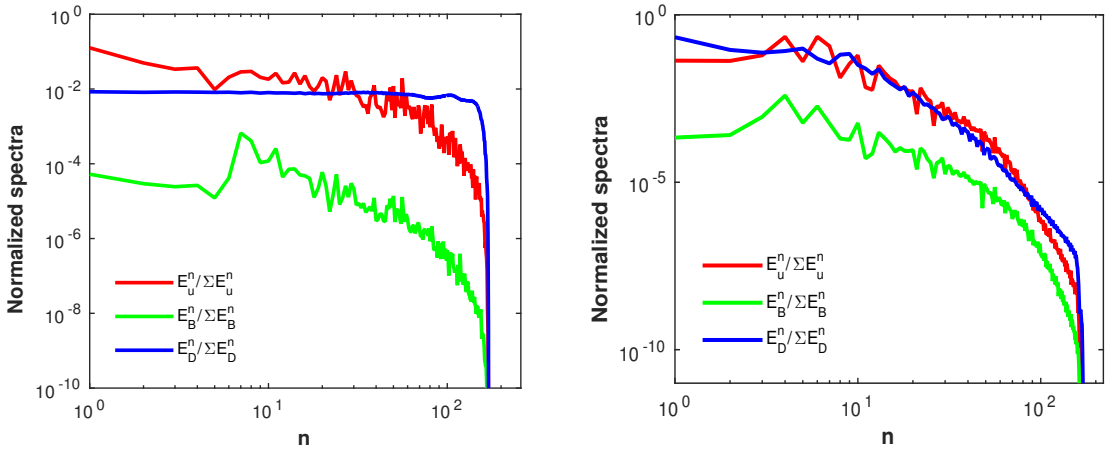

(a) (b)

Figure 6.15: Examples of a poorly resolved (a) and well resolved (b) simulation with respect to the passive field $\boldsymbol{D}$. (a) Normalized spectra of u^2 and B^2 for $R_m = 434$, and D^2 for $R'_m = 295$. (b) Normalized spectra of u^2 and B^2 for $R_m = 51$, and D^2 for $R'_m = 153$.

for the case of periodic box turbulence. Indeed, using the same 3 equations as in the present study they investigated how and whether a kinematic dynamo saturates when the amplified magnetic field, and thereby its retro-action on the velocity field becomes large enough to influence the dynamics. It was observed that even when the real magnetic field $\boldsymbol{B}$ saturates, the passive field $\boldsymbol{D}$ continues to grow.

One of the key insights obtained hereby is that the saturation is not due to the fact that the Lorentz-force changes the flow-structure such that it is not possible to amplify a magnetic field anymore. Indeed, if this was the case, $\boldsymbol{D}$ would saturate simultaneously with $\boldsymbol{B}$. Rather is it due to some intricate interplay between the velocity field and the magnetic field. It is therefore not visible from the velocity field alone in that case that the magnetic field saturates, and at which level. One should thus consider the simultaneous dynamics of $\boldsymbol{u}$ and $\boldsymbol{B}$.

One way to consider the simultaneous dynamics of the velocity and the magnetic field is to introduce the Elsasser variables, defined as,

$$\boldsymbol{\zeta}^+ = \boldsymbol{u} + \boldsymbol{D} \tag{6.21}$$

and

$$\boldsymbol{\zeta}^- = \boldsymbol{u} - \boldsymbol{D}. \tag{6.22}$$

In the case of full MHD, $\boldsymbol{D}$ is replaced by $\boldsymbol{B}$ in expressions (6.21) and (6.22). To simplify

the equations' derivation, we write the MHD equations as follows,

$$\frac{\partial \boldsymbol{u}}{\partial t} + \boldsymbol{u}\cdot\boldsymbol{\nabla}\boldsymbol{u} - \gamma\boldsymbol{B}\cdot\nabla\boldsymbol{B} = \nu\Delta\boldsymbol{u} - \nabla(P+\gamma\frac{B^2}{2}), \tag{6.23}$$

$$\frac{\partial \boldsymbol{B}}{\partial t} + \boldsymbol{u}\cdot\nabla\boldsymbol{B} - \boldsymbol{B}\cdot\nabla\boldsymbol{u} = \lambda\Delta\boldsymbol{B}, \tag{6.24}$$

$$\frac{\partial \boldsymbol{D}}{\partial t} + \boldsymbol{u}\cdot\nabla\boldsymbol{D} - \boldsymbol{D}\cdot\nabla\boldsymbol{u} = \lambda\Delta\boldsymbol{D}, \tag{6.25}$$

where $\gamma = 0$ in the case of the passive magnetic field and $\gamma = 1$ in the case of the full MHD system. Note that $\boldsymbol{u}$ and $\boldsymbol{D}$ can be written as,

$$\boldsymbol{u} = \frac{1}{2}(\boldsymbol{\zeta}^+ + \boldsymbol{\zeta}^-), \tag{6.26}$$

$$\boldsymbol{D} = \frac{1}{2}(\boldsymbol{\zeta}^+ - \boldsymbol{\zeta}^-). \tag{6.27}$$

We find therefore for $P_m = 1$,

$$\partial_t\boldsymbol{\zeta}^+ + \frac{3+\gamma}{4}\zeta_j^-\partial_j\zeta_i^+ + \frac{1-\gamma}{4}[\frac{\partial}{\partial x_j}(\zeta_j^+\zeta_i^+ + \zeta_j^-\zeta_i^- - \zeta_j^+\zeta_i^-)] = -\frac{\partial}{\partial x_i}(P+\gamma\frac{B^2}{2}) + \nu\Delta\boldsymbol{\zeta}^+, \tag{6.28}$$

and

$$\partial_t\boldsymbol{\zeta}^- + \frac{3+\gamma}{4}\zeta_j^+\partial_j\zeta_i^- + \frac{1-\gamma}{4}[\frac{\partial}{\partial x_j}(\zeta_j^+\zeta_i^+ + \zeta_j^-\zeta_i^- - \zeta_j^-\zeta_i^+)] = -\frac{\partial}{\partial x_i}(P+\gamma\frac{B^2}{2}) + \nu\Delta\boldsymbol{\zeta}^-, \tag{6.29}$$

or in compact notation,

$$\partial_t\boldsymbol{\zeta}^\pm + \frac{3+\gamma}{4}\zeta_j^\mp\partial_j\zeta_i^\pm + \frac{1-\gamma}{4}[\frac{\partial}{\partial x_j}(\zeta_j^+\zeta_i^+ + \zeta_j^-\zeta_i^- - \zeta_j^\pm\zeta_i^\mp)] = -\frac{\partial}{\partial x_i}(P+\gamma\frac{B^2}{2}) + \nu\Delta\boldsymbol{\zeta}^\pm. \tag{6.30}$$

One clear way to see the interaction between $\boldsymbol{u}$ and $\boldsymbol{B}$ or $\boldsymbol{u}$ and $\boldsymbol{D}$ is to consider the case in which the velocity and magnetic field align. Indeed rapid local alignment of the velocity and the magnetic field was observed in several studies of incompressible MHD [105–107]. For $\gamma = 1$, the whole term proportional to $(1-\gamma)$ vanishes. Furthermore, the cross products $\zeta_j^\pm\zeta_i^\mp$ vanish when $\boldsymbol{u} = \pm\boldsymbol{B}$ or $\boldsymbol{u} = \pm\boldsymbol{D}$. For $\gamma = 0$, the terms proportional to $(1-\gamma)$ do not vanish. We see thus that for $\gamma = 0$ (a passively advected vector field), the depletion of nonlinearity is much weaker than for the full MHD system, $\gamma = 1$, where the whole term in square brackets is identical zero.

The alignment of $\boldsymbol{u}$ and $\boldsymbol{D}$ is shown in Figure 6.16 where the PDF of the $(\boldsymbol{u}, \boldsymbol{D})$ angle's cosine, denoted $\cos(\angle(\boldsymbol{u}, \boldsymbol{D}))$, is plotted at instants $t = 0$ and $t = 1200\tau_A$. At instant $t = 0$, the PDF is almost constant, hence no $(\boldsymbol{u}, \boldsymbol{D})$ alignment is observed. At instant

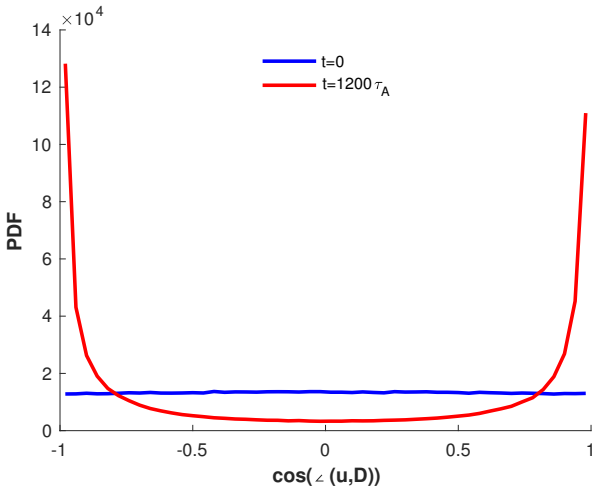

Figure 6.16: PDF of $\angle(\boldsymbol{u}, \boldsymbol{D})$ at instants $t = 0$ (blue) and $t = 1200\tau_A$ (red).

$t = 1200\tau_A$, the PDF reaches two peaks at $\cos(\angle(\boldsymbol{u}, \boldsymbol{D})) = \pm 1$, thus showing $(\boldsymbol{u}, \boldsymbol{D})$ alignment. However, the nonlinear term shown in equation (6.30) does not vanish in the case of alignment and equipartition. Therefore, it can be understood intuitively that the coupled $\boldsymbol{u}, \boldsymbol{D}$ dynamics do not have the same nonlinear behaviour as the $\boldsymbol{u}, \boldsymbol{B}$ dynamics. In particular the small scales of the magnetic field align rapidly with the magnetic field which leads to a depletion of the nonlinear term in the full MHD dynamics. The absence of this effect in the passively advected magnetic field dynamics, due to the presence of the nonlinear term in equation (6.30), is responsible for the rapid generation of small scale $\boldsymbol{D}$ modes even in the case of alignement, which therefore need a higher resolution to be resolved than the smallest $\boldsymbol{B}$ scales.

6.4.3 Dynamo growth rate and threshold

Simulations of a flow with $Re = 50$ and $P'_m = 1.43; 2$ are carried out, and the time evolution of the mean passive magnetic energy is plotted in Figure 6.17(a). It is observed that for $P'_m = 2$ the RFP field in the turbulent regime is capable of amplifying a seed magnetic field , and the RFP velocity field can therefore be called, as for the laminar case, a dynamo velocity field. In the case of $P'_m = 1.43$, the passive magnetic energy fluctuates around a constant value over a long-time interval. The threshold for dynamo action at $Re = 50$ is therefore close to $P'_m = 1.43$, and the critical magnetic Reynolds number in this case is thus $R'_{mc} = 71.5$. The new result is added to the data previously obtained in laminar regime (Figure 6.4(b)) and represented in green in Figure 6.17(b). The critical magnetic Reynolds number shows a tendency to become a constant at high Re regimes. Due to the

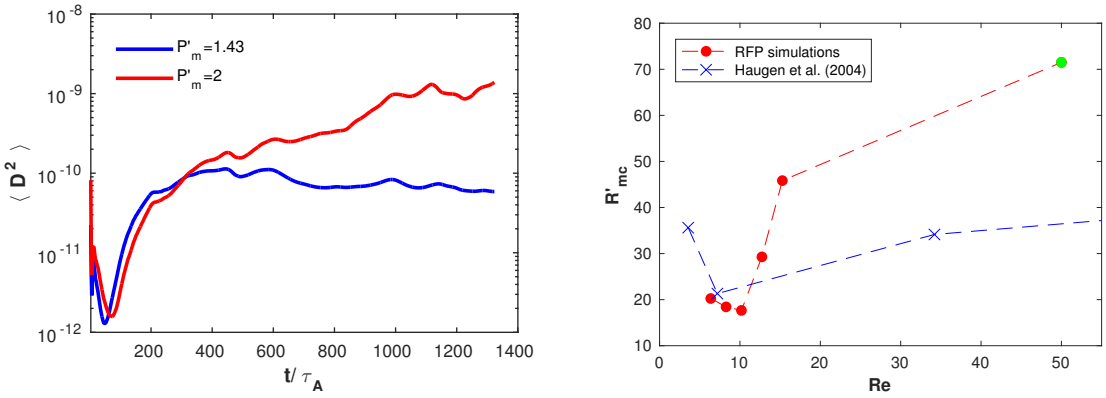

(a) (b)

Figure 6.17: (a) Time evolution of mean passive magnetic energy for a flow with $Re = 50$ and different values of P'_m. (b) Critical magnetic Reynolds number R'_{mc} function of Reynolds number Re.

high computational resources requirement for turbulent dynamo simulations, higher Re regimes are not explored in this manuscript.

Now we consider the time evolution of different axial modes of the kinetic, magnetic and passive magnetic energies. This is shown in Figure 6.18. In the case of passive magnetic energy, mode $n = 0$ is dominant for $t < 600\tau_A$, while different kinetic modes dominate during this period. Similarly for $t > 600\tau_A$, mode $n = 12$ is dominant in the kinetic energy spectra, while different modes dominate in the case of the passive magnetic energy. No clear correlation is observed between $\boldsymbol{u}$ and $\boldsymbol{D}$ in turbulent regime. An analysis of the average periodic interactions in this case could be carried out as reviewed in [108], but we have not attempted this.

6.5 Conclusion

To conclude this chapter, we can say that the RFP velocity field is capable of amplifying a seed magnetic field. In the laminar case it is even very efficient, considering the fact that the critical magnetic Reynolds number R'_{mc} is of the same order as that observed in flows specifically designed to generate a dynamo [81, 91, 101]. Also in the turbulent case dynamo action is observed. The numerical requirements are larger for such a simulation than for a standard RFP simulation, since the passive magnetic field can be considered "more nonlinear" than the actual magnetic field.

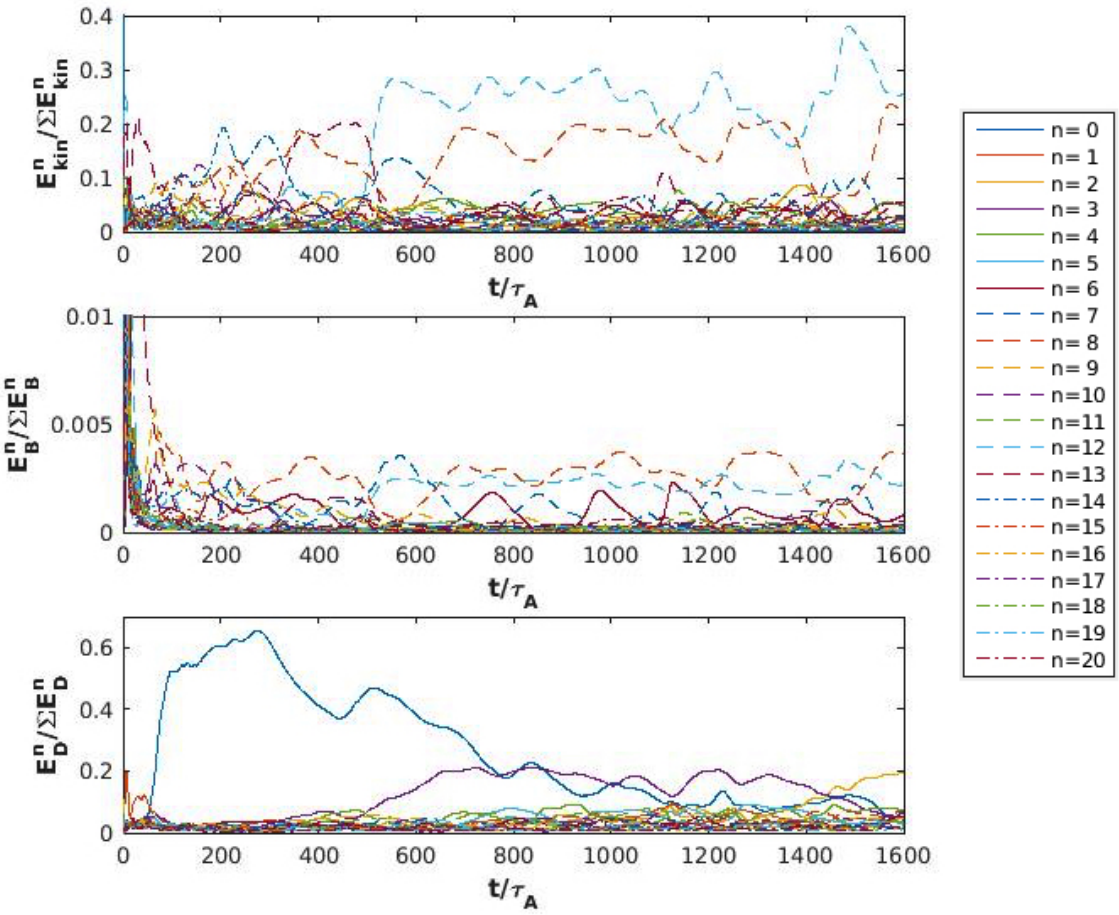

Figure 6.18: Time evolution of (a) kinetic, (b) magnetic and (c) passive magnetic axial modes for a flow with $Re = 50$ and $P'_m = 2$.

We hereby reconcile to some extent the RFP and the astrophysics community with respect to the question whether the RFP can be considered a dynamo or not.

Conclusion

The objective of this PhD thesis was to study several aspects of the RFP dynamics. This was done by considering the incompressible visco-resistive MHD description of a plasma in a straight cylinder. Furthermore, the plasma is assumed isothermal, and its conductivity and the transport coefficients are considered constant. Indeed this description is a very much simplified description of actual fusion plasmas. However it allows studying basic phenomena in the plasma. Indeed, our approach, as in previous investigations [25, 46, 47] is not to design a fusion reactor, or to model an existing one in as much detail as possible, but to highlight and understand some key physical mechanisms, which can allow to inspire the scientists and engineers which work on actual reactors. Whereas in hydrodynamics laboratory scale experiments can now be faithfully reproduced by numerical simulations, this is not yet the case for fusion plasmas, where either a precise description of the plasma is numerically too expensive in global simulations, or where global continuum descriptions miss some of the detailed plasma features. We have chosen this second approach and our simulations describe some global features, which, we hope, allow to obtain a better understanding of the RFP dynamics.

Numerically, a pseudo-spectral method was used to solve the governing equations combined with a penalization method, which consists in adding an additional term to the MHD equations that takes into account the corresponding Dirichlet conditions, used to impose the cylindrical geometry. These two methods were described in details in chapter 3. The advantage of the penalization method is the simplicity of geometry modification, which can be done just by changing a mask function.

This pseudo-spectral solver allowed us first to investigate the role of β in MHD simulations. This parameter has been long used to characterize magnetostatic equilibria of toroidally confined plasmas. In RFP regimes where the turbulent velocity field plays a major role in the dynamics, it is shown that this parameter is not adequate to characterize the importance of the pressure in the dynamics and the pressure effects on the RFP dynamics cannot be neglected. An elementary argument to explain this is that, if one considers two flows with different constant pressure, the β value will change but the dynamics will remain the same since the pressure gradient is null in both cases. Hence, the pressure gradient is what should

be considered rather than the pressure itself. We have shown that, when the momentum equation is expressed in terms of a parameter $\beta'_\nabla = \|\nabla P\|/\|\boldsymbol{J} \times \boldsymbol{B}\|$, the simulations for high Lundquist numbers S shows that β'_∇ remains constant with respect to S, while β drops approximately following a powerlaw proportional to $S^{-1/2}$. Furthermore, β'_∇ takes values close to unity, thus showing that the pressure gradients are of the same order of magnitude as the Lorentz-force, and therefore play a major role in the dynamics. Last, the radial profile of the axial magnetic field of simulations with large S, which corresponding to low β, does not approach the profiles corresponding to fully compressible simulations. This is another result which illustrates that β is not the proper parameter to describe the dynamics.

In chapter 5, we investigated the influence of shaping of the poloidal cross-section on the RFP dynamics. Simulations of flows with the same Lundquist number and different cross-sections, a circle and two different ellipses, were carried out. Results showed that the $F - \Theta$ curve remained relatively unchanged, while the spectral behaviour was drastically modified. In order to understand the effect of this change on the confinement, we studied the advection of a passive scalar in the three geometries. The radial profile of this scalar indicated a reduced radial turbulent diffusion in the ellipses' case and a remarkable change in the q-profile of the different geometries. However, it was shown subsequently that even when the magnetic field in the circular case relaxes toward a state similar to the one of elliptical geometry, the q-profiles remain different. All these results show that the shaping of the poloidal cross-section has a significant effect on the dynamics.

In the last chapter of this manuscript, we studied the dynamo effect using RFP flows. It is shown that the RFP velocity field is capable of amplifying a seed magnetic field. Furthermore, critical magnetic Reynolds numbers R'_{mc} extracted from the laminar dynamo simulations had the same order as those observed in flows designed to generate a dynamo. In the turbulent regime, the seed magnetic field showed a tendency to be more nonlinear, and thus requires higher numerical resolution. This was explained using the Elsasser variables to show that there is an additional nonlinear term added to the coupled dynamics, which is not zero in the case of alignment between the velocity and the seed magnetic field.

Perspectives

In the present work, the RFP fusion plasma is modeled using incompressible MHD simulations. Indeed this simplified model is far from reality, however it simplifies the study of basic phenomena. Since axial magnetic field reversal has a stronger tendency to occur in compressible MHD flows than in incompressible flows, it would be interesting to develop a compressible version of the present code.

In chapter 5, we saw that the q-profiles of the different geometries were different. Changing the initial conditions so that all the three geometries relax towards the same initial q-profile would constitute an interesting perspective. Also, the contrary, starting from the same initial q-profile and evaluate the differences in the eventual, relaxed states could further inform us on the influence of shaping.

The result in chapter 5 that shaping does have an effect on RFP dynamics could be extended to different geometries, for instance the D-shape cross-section which is chosen for ITER, in an attempt to optimize the confinement.

To have a more realistic measure of the change in confinement in different cases, the study measuring the radial diffusion in chapter 5 can be improved at several points. One improvement of the advection-diffusion equation can be done by replacing the forcing term by the ohmic heating ηJ^2 which would be the most natural way to study the advection in the case the considered scalar is the temperature.

Another possible refinement concerns the transport coefficients. One could consider in a follow-up study to replace the isotropic thermal diffusion by an anisotropic one, allowing thus faster diffusion along the magnetic field lines. Furthermore, since the QSH states were obtained for high currents [14] in circular RFPs, it would be interesting to see if we can generate these states in shaped RFPs.

Finally, for the dynamo study, high Reynolds simulations are needed to explore more the turbulent dynamo regime. These simulations will allow to explore the variation of the critical magnetic Reynolds number with respect to the Reynolds number.

Epilogue

It seems from these conclusions that the current understanding of the RFP, in particular due to its nonlinear character is still not complete. Given the complexity of the plasma description a further understanding necessarily needs an interaction between simulations, analytical studies, integrated modeling and experimental observations. The current limited understanding leaves for the moment still a large room for improvement of the RFP, hopefully enough to reach sustainable fusion.

Additional investigations

This chapter reports on two investigations which are not directly connected to the main subject of the rest of the manuscript. The first appendix reports on the development and validation of a novel numerical method for MHD computations. Appendix B reports the investigation on the mixing efficiency of a periodically modulated turbulent flow.

Appendix A

Advanced Lattice Boltzmann scheme for high-Reynolds number Magnetohydrodynamic flows

REGULAR ARTICLE

Advanced Lattice Boltzmann Scheme for High-Reynolds-number Magneto-Hydrodynamic Flows

A. De Rosis[a,b], Emmanuel Lévêque[b] , Robert Chahine[b]

[a]Department of Biomedical Engineering Technion - Israel Institute of Technology, 32000, Haifa, Israel
[b]Univ Lyon - Ecole Centrale de Lyon - CNRS - Laboratoire de Mécanique des Fluides et d'Acoustique, F-69134 Ecully cedex, France

ARTICLE HISTORY
Compiled May 15, 2017

ABSTRACT
Is the lattice Boltzmann method suitable to investigate numerically high-Reynolds-number magneto-hydrodynamic (MHD) flows? It is shown that a standard approach based on the Bhatnagar-Gross-Krook (BGK) collision operator rapidly yields unstable simulations as the Reynolds number increases. In order to circumvent this limitation, it is here suggested to address the collision procedure in the space of central moments for the fluid dynamics. Therefore, an hybrid LB scheme is introduced, which couples a central-moment scheme for the velocity with a BGK scheme for the space-and-time evolution of the magnetic field. This method outperforms the standard approach in terms of stability, allowing us to simulate high-Reynolds-number MHD flows with non-unitary Prandtl number while maintaining high accuracy.

KEYWORDS
Lattice Boltzmann method, magnetohydrodynamics, turbulence

The use of the lattice Boltzmann (LB) method has become ubiquitous in many areas of computational fluid dynamics, and now represents a consolidate alternative to classical approaches based on the discretization of the incompressible Navier-Stokes equations [1–8]. In short, the flow is inferred from the motion of distributions of fictitious particles streaming and colliding along the links of a regular lattice. The LB method has practical advantages with respect to a continuum-based formulation. In particular, LB dynamics is governed by a first-order partial differential equation in which non-localities and non-linearities are well separated [5]. Conversely, the integration of the Navier-Stokes equations requires the evaluation of first and second-order derivatives, and possibly the application of a non-local Poisson solver to obtain the pressure field. Moreover, the computational complexity of the continuum-based approach becomes rapidly prominent and evident when the fluid dynamics encompasses additional physical features such as magnetic effects. In that case, the particulate nature of the LB approach offers some tangible advantages, as will be demonstrated in this article.

The incompressible Navier-Stokes equations for magnetohydrodynamics (MHD) drive the evolution of an electrically conductive fluid of kinematic viscosity ν and

CONTACT A. De Rosis. Email: alessandro@bm.technion.ac.il, derosis.alessandro@icloud.com

magnetic diffusivity η in the form

$$\partial_t \boldsymbol{u} + (\boldsymbol{u}\cdot\nabla)\,\boldsymbol{u} = -\frac{\nabla p}{\rho} + \nu\Delta\boldsymbol{u} + \frac{\boldsymbol{j}\times\boldsymbol{b}}{\rho}$$
$$\partial_t \boldsymbol{b} = \nabla\times(\boldsymbol{u}\times\boldsymbol{b}) + \eta\Delta\boldsymbol{b}$$
$$\nabla\cdot\boldsymbol{u} = 0$$
$$\nabla\cdot\boldsymbol{b} = 0$$

where ρ and $\boldsymbol{u}$ are the mass density and velocity of the fluid, respectively. The vector field $\boldsymbol{b}$ denotes the magnetic field and $\boldsymbol{j} = \boldsymbol{\nabla}\times\boldsymbol{b}$ is the electric current. The fluid pressure p stems from the incompressibility constraint $\nabla\cdot\boldsymbol{u} = 0$. In comparison with the non-magnetic case, here it is mandatory to integrate a coupled set of non-linear partial differential equations for the velocity and magnetic fields, thus leading to heavy computations.

Our motivation is to explore the possibility to use the LB method to investigate numerically high-Reynolds-number MHD flows with non-unitary Prandtl number. The earliest attempt to build a lattice gas automaton for MHD refers to [9] by Montgomery and Doolen. It is based on a magnetic vector potential formulation. The inclusion of the Lorentz force relies on the computation of a Laplacian operator with the consequent implementation of an additional non-local finite-difference procedure. Later, a purely local lattice gas model has been introduced by Chen *et al.* [10]. However, this modeling requires to solve a 36-state MHD Cellular Automaton system at each node of a two-dimensional hexagonal lattice, hence leading to a dramatic computational cost. Martinez *et al.* [11] have managed to reduce the number of states to twelve. In addition, an hybrid scheme coupling the LB approach with finite-difference discretization has been proposed by Succi *et al.* [12] for two-dimensional MHD, allowing for simulations with a magnetic Prandtl number, defined as the ratio between the kinematic viscosity and the magnetic diffusivity, fixed at unity.

More recently, Dellar has demonstrated that the solution of the aforementioned set of MHD equations may be recovered by solving two coupled LB schemes based on the BGK collision operator [13]. The former involves densities of fictitious particles carrying amount of mass, namely f_i in each direction, and accounting for the evolution of the mass density ρ and momentum $\rho\boldsymbol{u}$ of the fluid. The latter involves particles carrying amount of magnetic field, namely $\boldsymbol{g}_i$ in each direction, and addressing the dynamics of the magnetic field $\boldsymbol{b}$. This algorithm overcomes the major limitations of the previous efforts. It is purely local, the magnetic Prandtl number $\mathrm{Pr_m}$ is not limited at unity and the computational cost is very affordable. This scheme will be considered below and used as a baseline for the development of an improved scheme dedicated to high-Reynolds-number MHD flows.

Following [13], the D2Q9 and D2Q5 lattices are adopted for f_i and $\boldsymbol{g}_i$, respectively. Here, two-dimensional modeling is considered for the sake of clarity, the extension to three dimensions being straightforward and outlined at the end of the article. The lattice directions are denoted by $\boldsymbol{c}_i = [|c_{ix}\rangle, |c_{iy}\rangle]$ with

$$|c_{ix}\rangle = [0,\,1,\,0,\,-1,\,0,\,1,\,-1,\,-1,\,1]^\top,$$
$$|c_{iy}\rangle = [0,\,0,\,1,\,0,\,-1,\,1,\,1,\,-1,\,-1]^\top,$$

where $|\bullet\rangle$ denotes a column vector and the superscript $\top$ indicates the transpose of a vector. At position $\boldsymbol{x}$ and time t, the LB scheme advances the set of distributions in

a two-step procedure. Namely, a streaming step for fluid particles

$$f_i(\boldsymbol{x}+\boldsymbol{c}_i\Delta t, t+\Delta t) = f_i^{\rm coll}(\boldsymbol{x},t)$$

is consecutive to a collision step

$$f_i^{\rm coll}(\boldsymbol{x},t) = f_i(\boldsymbol{x},t) - \omega_\nu \left[f_i(\boldsymbol{x},t) - f_i^{eq}(\boldsymbol{x},t)\right].$$

The so-called BGK approximation refers to this simple form of the collision operator, which expresses as the relaxation with the same rate of all distributions towards absolute equilibrium. Similarly, for the magnetic-field particles

$$\boldsymbol{g}_i(\boldsymbol{x}+\boldsymbol{c}_i\Delta t, t+\Delta t) = \boldsymbol{g}_i^{\rm coll}(\boldsymbol{x},t)$$

with

$$\boldsymbol{g}_i^{\rm coll}(\boldsymbol{x},t) = \boldsymbol{g}_i(\boldsymbol{x},t) + \omega_\eta \left[\boldsymbol{g}_i^{eq}(\boldsymbol{x},t) - \boldsymbol{g}_i(\boldsymbol{x},t)\right].$$

Here and henceforth, the index i spans the directions $i = 0\cdots 8$ (D2Q9 lattice) and $i = 0\cdots 4$ (D2Q5 lattice) for the distributions f_i and $\boldsymbol{g}_i$, respectively. The relaxation frequencies ω_ν and ω_η are related to the kinematic viscosity and magnetic diffusivity of the fluid by

$$\nu = \left(\frac{1}{\omega_\nu} - \frac{1}{2}\right) c_s^2$$

and

$$\eta = \left(\frac{1}{\omega_\eta} - \frac{1}{2}\right) \theta^2$$

with $c_s^2 = \theta^2 = \frac{1}{3}$ in lattice units. In this framework, the variable c_s (and θ) refers to the characteristic speed of the particles and may be associated to some extent with a lattice sound speed. Since, nearly-incompressible flows are concerned, the related Mach number $\mathrm{Ma} = |\boldsymbol{u}|/c_s \ll 1$. Let us recall that in the lattice Boltzmann method, the incompressible limit $\rho = \rho_0$ is approached with $\delta\rho/\rho_0 = O(\mathrm{Ma}^2)$ [14]. The equilibrium distributions are given by

$$\begin{aligned} f_i^{eq} &= w_i\rho\left[1 + \frac{\boldsymbol{c}_i\cdot\boldsymbol{u}}{c_s^2} + \frac{(\boldsymbol{c}_i\cdot\boldsymbol{u})^2}{2c_s^4} - \frac{\boldsymbol{u}\cdot\boldsymbol{u}}{2c_s^2}\right] \\ &+ \frac{w_i}{2c_s^4}\left[\frac{1}{2}|\boldsymbol{c}_i|^2|\boldsymbol{b}|^2 - (\boldsymbol{c}_i\cdot\boldsymbol{b})^2\right] \qquad (1) \\ g_{i\beta}^{eq} &= W_i\left[b_\beta + \frac{c_{\alpha i}}{\theta^2}\left(u_\alpha b_\beta - u_\beta b_\alpha\right)\right] \qquad (2) \end{aligned}$$

where α and β span the Cartesian coordinates. The weighting factors are $w_0 = 4/9$, $w_{1\ldots4} = 1/9$, $w_{5\ldots8} = 1/36$ for the fluid dynamics, whereas $W_0 = 1/3$ and $W_{1\ldots4} = 1/6$

for the magnetic field. Finally, the macroscopic fields are inferred locally by

$$\rho = \sum_{i=0}^{8} f_i, \quad \rho \boldsymbol{u} = \sum_{i=0}^{8} f_i \boldsymbol{c}_i, \quad \boldsymbol{b} = \sum_{i=0}^{4} \boldsymbol{g}_i. \tag{3}$$

Paul Dellar has demonstrated that this LB scheme was compliant with the MHD equations in the continuous limit through a Chapman-Enskog expansion [13].

This original scheme is now tested against the Orszag-Tang vortex problem [13,15]. This test case has become a popular benchmark representative of many features of turbulent MHD flows, such as magnetic reconnection, formation of jets and dynamic alignment. The deterministic initial conditions allows for a direct comparison between several numerical modeling. Precisely, the flow of an electrically conductive fluid develops in a square periodic box of size $L = 2\pi$ m with the initial velocity fields

$$\boldsymbol{u}(\boldsymbol{x}, 0) = 2 \times [-\sin y, \sin x] \tag{4}$$

$$\boldsymbol{b}(\boldsymbol{x}, 0) = 2 \times [-\sin y, \sin 2x] \tag{5}$$

in m/s (physical units). The initial density is uniform with $\rho(\boldsymbol{x}, 0) = 1$ kg/m^3. In our simulations, each dimension is discretized into $N = 1024$ grid points. The grid resolution is therefore $\Delta x = L/N \approx 6 \times 10^{-3}$ m and the time step is fixed at $\Delta t = 5 \times 10^{-5}$ s. In lattice units, this yields the reference velocity $u_0 = 2 \times \Delta t / \Delta x \approx 1.6 \times 10^{-2}$ and the Mach number $\mathrm{Ma} \equiv u_0 / c_s \approx 3 \times 10^{-2}$. The Reynolds number is defined as $\mathrm{Re} = u_0 N / \nu$. Moreover, the magnetic Prandtl number is set to $\mathrm{Pr_m} \equiv \nu / \eta = 1$. Five runs have been performed by varying Re between 500 and 5000. In Fig. 1, the time evolution of the maxima of the electric current $j_{\max}(t) = \max_{\boldsymbol{x}} |j(\boldsymbol{x}, t)|$ is displayed. Notice that the current has only one non-zero component j. Furthermore, the LB method allows us to compute the current locally and directly from the distributions, thus avoiding the use of additional time-consuming finite-difference operators [16].

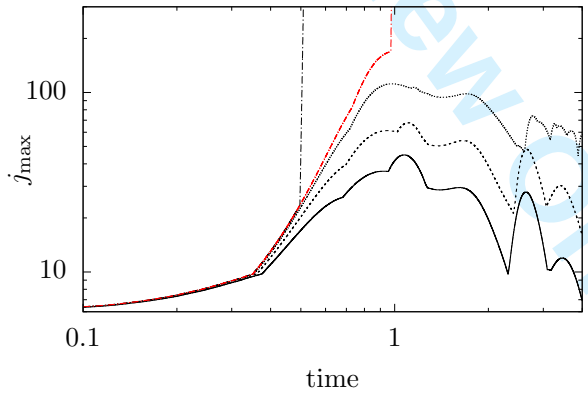

Figure 1. Orszag-Tang vortex problem. LB simulations based on the BGK collision operator [13]. Time evolution of the current maxima at Re = 500 (continuous line), 1000 (dashed), 2500 (dotted) and 5000 (dashed-dotted). At the highest Re, an instability occurs at $t \approx 0.52$ s. For the same Re, a finer grid consisting of 1536^2 grid points (red dashed-dotted) allows us to extend the range of simulation. However, a blow-up eventually occurs at $t \approx 0.99$ s.

The three lowest values of Re lead to stable simulations (see Fig. 1). As expected, the maxima grow exponentially in the earliest stage [17,18]. However, a sudden blow-up

is experienced at $t \approx 0.52$ s at $\mathrm{Re} = 5000$. This observation is consistent with previous results in [19], where marked difficulties were found to carry numerical experiments beyond $t = 0.6$ s. A refinement of the grid with 1536 grid points per direction partially alleviates the onset of instability, which is now delayed at time $t \approx 0.99$ s. Let us mention that the time step has also been reduced in order to keep the Mach number constant. In conclusion, it is found that within the BGK approximation large-time behavior can be investigated only by adopting very fine grid resolutions, thus leading to very expensive computations. This constraint becomes prohibitive when simulating high-Reynolds-number MHD flows.

The poor performance of the LB scheme under the BGK approximation appears more evident in Fig. 2. The maximal attainable Reynolds number for the Orszag-Tang problem is reported as a function of the magnetic Prandtl number $\mathrm{Pr_m}$. It is found that this approach is unsuitable to simulate high-Reynolds and low-Prandtl numbers phenomena, in particular for liquid metals with $\mathrm{Pr_m} \sim 10^{-5}$.

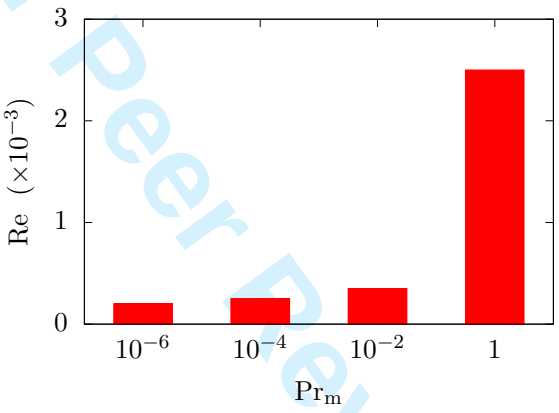

Figure 2. Orszag-Tang vortex problem. LB simulations based on the BGK collision operator [13]. Maximal attainable Reynolds number as a function of the magnetic Prandtl number.

The previous observed limitations are related to the very nature of the scheme. Despite its simplicity, effectiveness and large popularity, the BGK collision operator is known to suffer from numerical instabilities when large velocity gradients arise in the flow. Two main factors contribute to this deficiency: The uncontrolled growth of ghost (beyond hydrodynamics) modes [20,21] and the lack of sufficient Galilean invariance [22–28]. By decomposing the collision kernel in a space of raw moments, the multiple-relaxation-time model has proved to increase the stability by properly relaxing high-order moments [29]. However, the lack of Galilean invariance still persists [30]. A possible alleviation of this latter may be addressed by the entropic LBM [31], which was also adopted to investigate MHD turbulence [32]. More recently, a different idea has been proposed by Geier *et al.* [33] suggesting to relax the moments in a reference frame that moves with the fluid. This can be simply achieved by shifting the lattice velocities by the local fluid velocity, that is

$$|\bar{c}_{ix}\rangle = |c_{ix} - u_x\rangle \quad \text{and} \quad |\bar{c}_{iy}\rangle = |c_{iy} - u_y\rangle. \tag{6}$$

In this case, the involved quantities are called central moments (CMs). This method is also referred to as "cascaded" LB scheme, since the post-collision state of any central moment depends only on moments of lower order thus generating a pyramidal

hierarchical structure [34–38]. The numerical implementation of the cascaded LB scheme is known to be cumbersome. Nevertheless, some recent attempts have demonstrated that a simplified version of the CMs-based scheme (in a non-orthogonal basis) may be derived, entailing easier implementations [39–41]. This approach is here applied in the context of high-Reynolds-number MHD flows for the fluid particles.

By introducing the basis

$$\bar{\mathbf{T}} = [\bar{\mathbf{t}}_0, \ldots, \bar{\mathbf{t}}_i, \ldots, \bar{\mathbf{t}}_8], \tag{7}$$

with

$$\begin{aligned}
\bar{\mathbf{t}}_0 &= [1,\,1,\,1,\,1,\,1,\,1,\,1,\,1,\,1]^\top, \\
\bar{\mathbf{t}}_1 &= |\bar{c}_{ix}\rangle, \qquad \bar{\mathbf{t}}_2 = |\bar{c}_{iy}\rangle, \\
\bar{\mathbf{t}}_3 &= |\bar{c}_{ix}^2 + \bar{c}_{iy}^2\rangle, \qquad \bar{\mathbf{t}}_4 = |\bar{c}_{ix}^2 - \bar{c}_{iy}^2\rangle, \\
\bar{\mathbf{t}}_5 &= |\bar{c}_{ix}\bar{c}_{iy}\rangle, \qquad \bar{\mathbf{t}}_6 = |\bar{c}_{ix}^2\bar{c}_{iy}\rangle, \\
\bar{\mathbf{t}}_7 &= |\bar{c}_{ix}\bar{c}_{iy}^2\rangle, \qquad \bar{\mathbf{t}}_8 = |\bar{c}_{ix}^2\bar{c}_{iy}^2\rangle,
\end{aligned} \tag{8}$$

a suitable set of central moments is represented by

$$|k_i\rangle = [k_0, \ldots, k_i, \ldots, k_8]^\top, \tag{9}$$

with

$$|k_i\rangle = \bar{\mathbf{T}}^\top |f_i\rangle \tag{10}$$

and $|f_i\rangle = [f_0, f_1, f_2, f_3, f_4, f_5, f_6, f_7, f_8]^\top$. Each moment relaxes to an equilibrium state, k_i^{eq}, defined by replacing f_i with f_i^{eq} in Eq. (10). The resulting expressions of the equilibrium CMs are

$$\begin{aligned}
k_0^{eq} &= \rho, \\
k_1^{eq} &= 0, \\
k_2^{eq} &= 0, \\
k_3^{eq} &= \frac{2}{3}\rho, \\
k_4^{eq} &= b_y^2 - b_x^2, \\
k_5^{eq} &= -b_x b_y, \\
k_6^{eq} &= -\rho u_x^2 u_y + \frac{u_y}{2}\left(b_x^2 - b_y^2\right) + 2u_x b_x b_y, \\
k_7^{eq} &= -\rho u_x u_y^2 + \frac{u_x}{2}\left(b_y^2 - b_x^2\right) + 2u_y b_x b_y, \\
k_8^{eq} &= \frac{\rho}{9}\left(27u_x^2u_y^2 + 1\right) + \frac{u_x^2 - u_y^2}{2}\left(b_x^2 - b_y^2\right) \\
&- 4u_x u_y b_x b_y.
\end{aligned} \tag{11}$$

One can immediately notice the presence of some terms accounting for the magnetic field, stemming from the second term at the right-hand side of Eq. (1). The collision

operator reads

$$k_i^\star = k_i + \omega_i \left(k_i^{eq} - k_i\right) \quad \text{with } i = 3 \dots 8, \tag{12}$$

where ω_i is the relaxation frequency associated with the moment k_i. The superscript $\star$ refers to post-collision values. To be compliant with the MHD equations in the continuous limit, only the frequencies related to k_4 and k_5 need to be specified as a function of the fluid kinematic viscosity. Specifically, $\nu = (\frac{1}{\omega_\nu} - \frac{1}{2})c_s^2$ with $\omega_4 = \omega_5 = \omega_\nu$. The frequency ω_3 is related to the bulk viscosity, whereas ω_6, ω_7 and ω_8 are associated to higher-order ghost moments and can be set equal to unity, *i.e.* these moments are fixed at their equilibrium value after the collision step. Let us note that k_0, k_1 and k_2 are invariant with respect to the collision and are not involved in the collision step.

The post-collision central moments eventually yield the post-collision populations by inverting the mapping Eq. (10):

$$|f_i^\star\rangle = \left(\bar{\mathbf{T}}^\top\right)^{-1} |k_i^\star\rangle, \tag{13}$$

with $|k_i^\star\rangle = [\rho, 0, 0, k_3^\star, \dots, k_8^\star]^\top$ and $|f_i^\star\rangle = [f_0^\star, \dots, f_8^\star]^\top$. The collision step is followed up with a streaming of the populations towards their neighboring nodes on the lattice[1]. Note that this scheme only involves the evolution of the f_i's for the fluid particles. The evolution of the magnetic distributions $\boldsymbol{g}_i$ relies on the standard BGK collision operator, hence resulting in an hybrid scheme that combines CMs and multi-time relaxation for the fluid density and momentum, and single-time relaxation for the magnetic field.

To validate our hybrid scheme, the results are compared in Table 1 to those obtained in a high-resolution spectral simulation of the Orszag-Tang vortex at Re ≈ 628 at $\mathrm{Pr_m} = 1$ [13]. At time instants $t = 0.5$ s and $t = 1$ s, the current and vorticity maxima are registered. The latter is evaluated as $\zeta_{\max} = \max_{\boldsymbol{x}} |\zeta(\boldsymbol{x})|$ with $\zeta = \boldsymbol{\nabla} \times \boldsymbol{u}$ being the vorticity. The relative discrepancy (in percents) between present and reference values is denoted by err.

	t (s)	[13]	Present	err(%)
$j_{\max}$	0.5	18.24	18.24	0
	1	46.59	46.65	0.13
$\zeta_{\max}$	0.5	6.758	6.756	0.03
	1	14.20	14.18	0.14

Table 1. Orszag-Tang vortex problem at Re ≈ 628 ($\mathrm{Pr_m} = 1$). Reference spectral values from [13] and our results for the peak values of the electric current, $j_{\max}$, and vorticity, $\zeta_{\max}$, at two representative time instants.

Our scheme shows excellent properties in terms of accuracy. The relative error appears to slightly increase in time, which may be related to the rise of very large gradients both in the magnetic and velocity fields, as time advances. The capability to handle non-unitary magnetic Prandtl numbers is now examined. Therefore, the previous simulation is repeated with $\mathrm{Pr_m} = 0.5,\ 1,\ 2$. This is achieved by varying the magnetic diffusivity. In Fig. 3, the space-averaged magnetic energy $E_m =$

[1] In the Supplementary Material, a script `CentralMoments_MHD.m` is attached allowing the reader to derive the entire formulation.

$\frac{1}{N^2}\sum_{\boldsymbol{x}}|b(\boldsymbol{x})|^2$, kinetic energy $E_k = \frac{1}{N^2}\sum_{\boldsymbol{x}}|u(\boldsymbol{x})|^2$ and total energy $E = E_m + E_k$ are plotted as a function of time. The adoption of a constant ν explains the substantial

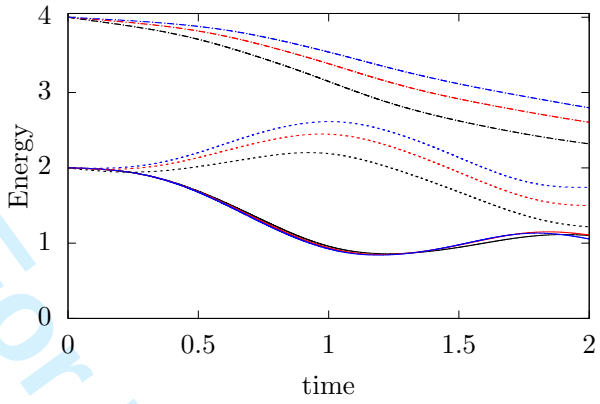

Figure 3. Orszag-Tang vortex problem at Re ≈ 628. Time evolution of the space-average kinetic (continuous lines), magnetic (dotted lines) and total (dashed-dotted lines) energies with $\mathrm{Pr_m} = 0.5$ (black), 1 (red) and 2 (blue). The kinetic energy does not experience a large influence. Conversely, the magnetic energy increases with $\mathrm{Pr_m}$ due to the reduction of the magnetic diffusivity η.

insensitivity of the kinetic energy to the variation of $\mathrm{Pr_m}$. Conversely, the magnetic energy, and the total energy as a consequence, undergoes large variations. In particular, E_m increases with $\mathrm{Pr_m}$ as the magnetic diffusivity reduces. Independently from the magnetic Prandtl number, a significant transfer of energy operates between the magnetic field and the flow, which is fully consistent with the original observations reported by Orszag and Tang in [15].

The tests at variable Re and fixed $\mathrm{Pr_m} = 1$ previously performed with the BGK collision operator (see Fig. 1) are now reproduced by implementing our hybrid LB scheme. In Fig. 4, the current maxima are displayed. It can be immediately appreciated

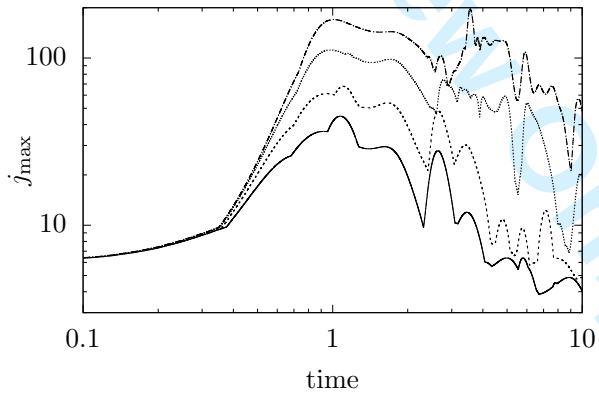

Figure 4. Orszag-Tang vortex problem. Hybrid LB simulation: Time evolution of the current maxima at Re = 500 (continuous line), 1000 (dashed), 2500 (dotted) and 5000 (dashed-dotted).

that the stability is drastically enhanced. In practice, a grid consisting of 1024^2 points now allows us to overcome the limit $t \approx 0.99$ s, for which a finer space-and-time resolution had led to a blow-up with the BGK scheme. After an exponential growth, a

faster self-similar increase is experienced with $j_{\max} \sim t^3$. It should be noted that this drastic change is slightly anticipated for larger Re. After reaching the peak value, the curves decrease with large oscillations. The decay is less prominent at high Re. These LB results are fully consistent with the previous reports in [42,43].

Further insights are available in Fig. 5(a), where the space-averaged magnetic enstrophy is reported as a function of time. This quantity is computed as $\mathcal{E}_m = \frac{1}{N^2}\sum_{\boldsymbol{x}} j(\boldsymbol{x})^2$. After reaching a maximum at $t \approx 1.2$ s, the curves corresponding to Re = 500 and Re = 1000 rapidly decay as $\sim t^{-2}$ with oscillations reflecting those experienced for the current maxima. As the Reynolds number increases, a plateau is observed after the initial growth. The local maximum at $t \approx 3.5$ s for the flow at Re = 5000 justifies the peak of $j_{\max}$ at that time instant. Eventually, all the enstrophies decay with a comparable rate under the effect of the overall dissipation. Fig. 5(b) shows the overall dissipation rate $\epsilon = \nu\mathcal{E}_k + \eta\mathcal{E}_m$, where the kinetic enstrophy

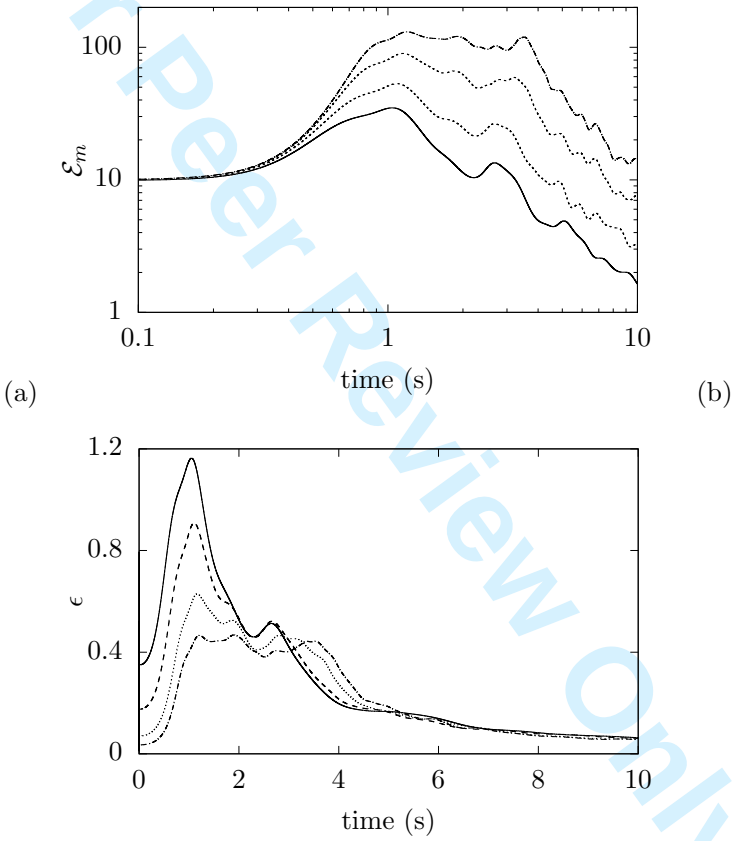

Figure 5. Orszag-Tang vortex problem. (a) Time evolution of the magnetic enstrophy at Re = 500 (continuous line), 1000 (dashed), 2500 (dotted) and 5000 (dashed-dotted). (b) Time evolution of the overall dissipation rate.

is $\mathcal{E}_k = \frac{1}{N^2}\sum_{\boldsymbol{x}} \zeta(\boldsymbol{x})^2$, $\zeta = \boldsymbol{\nabla} \times \boldsymbol{u}$ being the vorticity. In the earliest stage, the dissipation increases as Re decreases, highlighting a strong incidence of fluid and magnetic diffusivities. The dissipation rate exhibits a peak at the beginning of the flow. This initial increase is related to the development of small-scale structures in the velocity and magnetic fields. After this transient stage, ϵ reaches a plateau with a common value for the highest Reynolds numbers. This feature supports Pouquet's

hypothesis that the dissipation rate should converge towards a finite non-zero limit as $\nu = \eta \to 0$ in the developed regime [44]. This plateau is very apparent for the flow at $\mathrm{Re} = 5000$. In agreement with [15], this suggests that a flow singularity with $\zeta \to \infty$, *i.e.* flow structures of arbitrarily small size may occur at a finite time when $\mathrm{Re} \to \infty$.

In Fig. 6, the contour plot of the electric current at salient time instants give a better insight of the dynamics of the magnetic field. At $t = 1$ s, the field exhibits few folds. A straight current sheet passes through the center of the domain, where the maximum is located. This central current sheet goes unstable and very thin structures develop in the flow. At $t = 5$ s, folds seem to surround two big oculi separated by the central sheet, which it is now stabilized. As the time advances, these two big zones are

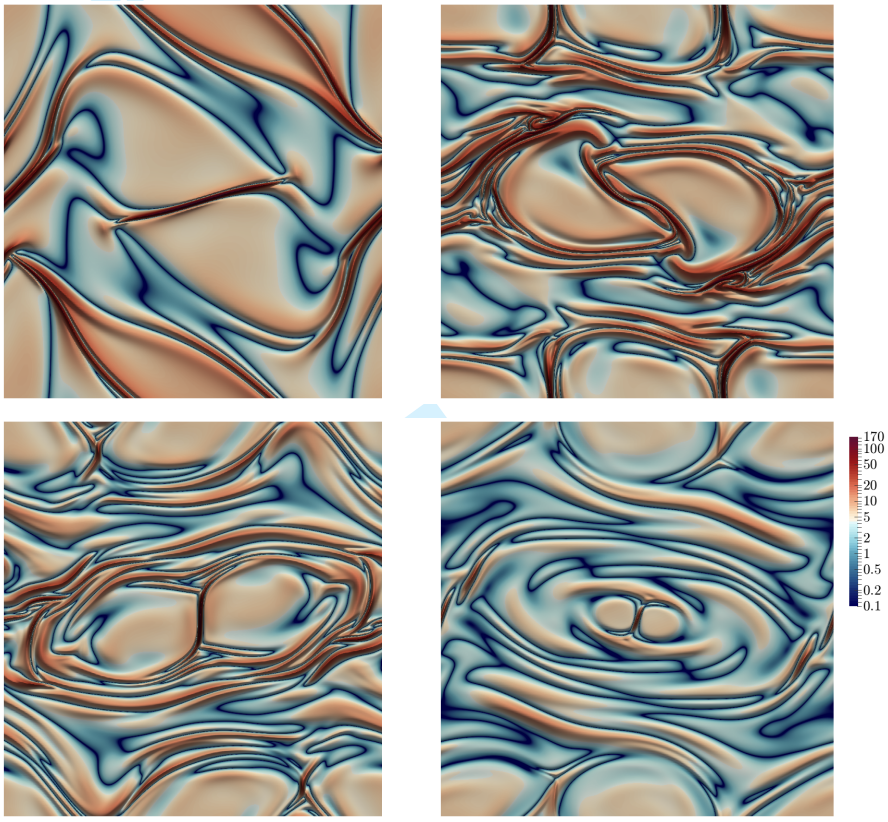

Figure 6. Evolution of the electric current at $\mathrm{Re} = 5000$ at salient time instants, *i.e.* $t = 1$ s (top left), 3.5 s (top right), 5 s (bottom left) and 9 s (bottom right). The maximal current is initially located in the central current sheet. The current field undergoes instabilities and many folds arise. Eventually, the central sheet becomes stable again and small-scale structures disappear progressively.

progressively damped by the diffusivities. An Alfenization of the flow, *i.e.* $\boldsymbol{u} = \pm\boldsymbol{b}$, is expected in the region of high concentration of folds [42]. A quantitative assessment of this effect can be obtained by evaluating the correlation coefficient between the velocity and magnetic fields as $r = \dfrac{2\boldsymbol{u}\cdot\boldsymbol{b}}{u^2 + b^2}$. The map of its absolute value is plotted at $t = 3.5$ s in Fig. 7. We observe that the correlation is more marked in the vicinity of the current sheets, whereas $\boldsymbol{u}$ and $\boldsymbol{b}$ remain mostly uncorrelated in the rest of the domain. This effect is very well captured by our LB simulation. Finally, our proposed scheme shows an impressive stability even for low values of the magnetic Prandtl number. In fact,

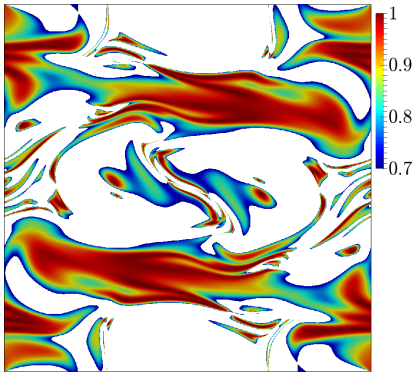

Figure 7. Absolute value of the correlation coefficient r at time instant $t = 3.5$ s. The flow shows strong correlation in the proximity of current sheets.

we are able to simulate scenarios with vanishing $\mathrm{Pr_m}$ (as $\nu \to 0$) without experiencing the limitations stemming from the adoption of the BGK model.

The possibility to extend the formulation of our hybrid LB scheme to three dimensions is now outlined. In that case, the D3Q27 and D3Q7 lattices should be used for the distributions f_i and $\boldsymbol{g}_i$, respectively. For the magnetic field, the LB scheme shall still rely on the BGK collision operator with $\theta^2 = 1/4$ and the weights W_i related to the D3Q7 lattice. For the velocity field, the scheme should be handled according to the CMs-based scheme recently introduced in [40]. In short, it consists of building the matrix $\bar{\mathbf{T}}$ in the D3Q27 velocity space and to compute pre-collision, equilibrium and post-collision CMs accordingly. The overall construction of the algorithm remains unaltered.

In conclusion, we have demonstrated the feasibility of the LB method to investigate high-Reynolds MHD flows at non-unitary Prandtl number with an hybrid scheme. Specifically, it is fruitful to decompose the collision stage entering in the dynamics of the fluid velocity in the space of central moments in order to overcome the stability limitations affecting the BGK scheme. In two-dimensions, we have shown that this hybrid scheme enables to reproduce very accurately the key features of the Orszag-Tang vortex problem. Its implementation is not awkward and the generalization to three dimensions is rather straightforward.

Supplementary material

A script is provided in the Supplementary Material (`D2Q9_CentralMoments_MHD.m`) allowing the reader to perform all the symbolic manipulations to obtain the proposed scheme.

This work has been carried out within the framework of the "Programme Avenir Lyon Saint-Etienne" at the *Université de Lyon* (ANR-11-IDEX-0007) under the Program "Investissements d'Avenir" operated by the French National Research Agency. The research leading to these results has received funding from the People Programme (Marie Curie Actions) of the European Union's Seventh Framework Programme (FP7/2007-2013) under REA grant agreement n° PCOFUND-GA-2013-609102, through the PRESTIGE programme coordinated by Campus France.
This article is based upon work from COST Action MP1305, supported by COST

(European Cooperation in Science and Technology). The authors are grateful to W.J.T. Bos and N. Plihon for useful hints about magneto-hydrodynamic turbulence.

References

[1] McNamara GR, Zanetti G. Use of the boltzmann equation to simulate lattice-gas automata. Phys Rev Lett. 1988;61(20):2332.
[2] Higuera F, Succi S, Benzi R. Lattice gas dynamics with enhanced collisions. Europhys Lett. 1989;9(4):345–349.
[3] Benzi R, Succi S, Vergassola M. The lattice Boltzmann equation: Theory and applications. Phys Rep. 1992;222(3):145–197.
[4] Chen S, Doolen G. Lattice Boltzmann method for fluid flows. Annu Rev Fluid Mech. 1998;30(1):329–364.
[5] Succi S. The lattice Boltzmann equation for fluid dynamics and beyond. Clarendon; 2001.
[6] Chen H, Kandasamy S, Orszag S, et al. Extended boltzmann kinetic equation for turbulent flows. Science. 2003;301(5633):633–636.
[7] Succi S. Lattice Boltzmann 2038. Europhys Lett. 2015;109(5):50001–50007.
[8] Succi S. Chimaera simulation of complex states of flowing matter. Phil Trans R Soc A. 2016;374(2080):20160151.
[9] Montgomery D, Doolen GD. Magnetohydrodynamic cellular automata. Phys Lett A. 1987; 120(5):229–231.
[10] Chen H, Matthaeus W, Klein L. An analytic theory and formulation of a local magnetohydrodynamic lattice gas model. Phys Fluids. 1988;31(6):1439–1455.
[11] Martínez DO, Chen S, Matthaeus WH. Lattice boltzmann magnetohydrodynamics. Phys Plasmas. 1994;1(6):1850–1867.
[12] Succi S, Vergassola M, Benzi R. Lattice boltzmann scheme for two-dimensional magnetohydrodynamics. Phys Rev A. 1991 Apr;43:4521–4524. Available from: `http://link.aps.org/doi/10.1103/PhysRevA.43.4521`.
[13] Dellar PJ. Lattice kinetic schemes for magnetohydrodynamics. J Comput Phys. 2002; 179(1):95–126.
[14] Dellar PJ. Incompressible limits of lattice boltzmann equations using multiple relaxation times. J Comput Phys. 2003;190(2):351–370.
[15] Orszag SA, Tang CM. Small-scale structure of two-dimensional magnetohydrodynamic turbulence. J Fluid Mech. 1979;90(01):129–143.
[16] Pattison M, Premnath K, Morley N, et al. Progress in lattice boltzmann methods for magnetohydrodynamic flows relevant to fusion applications. Fusion Eng Des. 2008; 83(4):557–572.
[17] Frisch U, Pouquet A, Sulem PL, et al. The dynamics of two-dimensional ideal mhd. J Mec Theor et Appl. 1983;1:191–216.
[18] Klapper I, Rado A, Tabor M. A lagrangian study of dynamics and singularity formation at magnetic null points in ideal three-dimensional magnetohydrodynamics. Phys Plasmas. 1996;3(11):4281–4283.
[19] Grauer R, Marliani C. Current-sheet formation in 3d ideal incompressible magnetohydrodynamics. Phys Rev Lett. 2000;84(21):4850.
[20] Chen H, Teixeira C, Molvig K. Digital physics approach to computational fluid dynamics: Some basic theoretical features. Int J Mod Phys C. 1997;08(04):675–684.
[21] Latt J, Chopard B. Lattice boltzmann method with regularized pre-collision distribution functions. Math Comput Simulat. 2006;72(2–6):165 – 168.
[22] Qian YH, Orszag SA. Lattice bgk models for the navier-stokes equation: Nonlinear deviation in compressible regimes. Europhys Lett. 1993;21(3):255.
[23] Nie XB, Shan X, Chen H. Galilean invariance of lattice boltzmann models. EPL. 2008; 81(3):34005.

[24] Chen Y, Ohashi H, Akiyama M. Thermal lattice bhatnagar-gross-krook model without nonlinear deviations in macrodynamic equations. Phys Rev E. 1994 Oct;50:2776–2783.
[25] Qian YH, Zhou Y. Complete galilean-invariant lattice bgk models for the navier-stokes equation. Europhys Lett. 1998;42(4):359.
[26] Házi G, Kávrán P. On the cubic velocity deviations in lattice boltzmann methods. J Phys A Math Gen. 2006;39(12):3127.
[27] Keating B, Vahala G, Yepez J, et al. Entropic lattice boltzmann representations required to recover navier-stokes flows. Phys Rev E. 2007;75(3):036712.
[28] Dellar PJ. Lattice boltzmann algorithms without cubic defects in galilean invariance on standard lattices. J Comput Phys. 2014;259:270 – 283.
[29] d'Humières D. Multiple-relaxation-time lattice Boltzmann models in three dimensions. Philos T R Soc A. 2002;360(1792):437–451.
[30] Chen H, Gopalakrishnan P, Zhang R. Recovery of galilean invariance in thermal lattice boltzmann models for arbitrary prandtl number. Int J Mod Phys C. 2014;25(10):1450046.
[31] Boghosian BM, Love PJ, Coveney PV, et al. Galilean-invariant lattice-boltzmann models with h theorem. Phys Rev E. 2003;68(2):025103.
[32] Vahala G, Keating B, Soe M, et al. Mhd turbulence studies using lattice boltzmann algorithms. Commun Comput Phys. 2008;4:624–646.
[33] Geier M, Greiner A, Korvink J. Cascaded digital lattice Boltzmann automata for high Reynolds number flow. Phys Rev E. 2006;73(6):066705.
[34] Geier M, Greiner A, Korvink J. Properties of the cascaded lattice Boltzmann automaton. Int J Mod Phys C. 2007;18(04):455–462.
[35] Geier M, Greiner A, Korvink J. A factorized central moment lattice Boltzmann method. The European Physical Journal Special Topics. 2009;171(1):55–61.
[36] Premnath K, Banerjee S. Incorporating forcing terms in cascaded lattice Boltzmann approach by method of central moments. Phys Rev E. 2009;80(3):036702.
[37] Premnath K, Banerjee S. On the three-dimensional central moment lattice Boltzmann method. J Stat Phys. 2011;143(4):747–794.
[38] Geier M, Schönherr M, Pasquali A, et al. The cumulant lattice Boltzmann equation in three dimensions: Theory and validation. Comput Math Appl. 2015;70(4):507–547.
[39] Lycett-Brown D, Luo K. Multiphase cascaded lattice Boltzmann method. Comput Math Appl. 2014;67(2):350–362.
[40] De Rosis A. Nonorthogonal central-moments-based lattice boltzmann scheme in three dimensions. Phys Rev E. 2017;95:013310.
[41] De Rosis A. Non-orthogonal central moments relaxing to a discrete equilibrium: A d2q9 lattice boltzmann model. Europhys Lett. 2017;116(4):44003.
[42] Mininni P, Pouquet A, Montgomery D. Small-scale structures in three-dimensional magnetohydrodynamic turbulence. Phys Rev Lett. 2006;97(24):244503.
[43] Alexakis A, Mininni PD, Pouquet A. Shell-to-shell energy transfer in magnetohydrodynamics. i. steady state turbulence. Phys Rev E. 2005 Oct;72:046301. Available from: http://link.aps.org/doi/10.1103/PhysRevE.72.046301.
[44] Pouquet A. On two-dimensional magnetohydrodynamic turbulence. J Fluid Mech. 1978; 88(1):1–16.

Appendix B

Mixing in modulated turbulence. Numerical results

Mixing in modulated turbulence. Numerical results

Yuyao Yang[1], Robert Chahine[1], Robert Rubinstein[2], Wouter J.T. Bos[11]
[1] *LMFA, CNRS, Ecole Centrale de Lyon, Université de Lyon, 69134 Ecully, France*
[2] *Newport News, VA, USA*

We investigate the mixing of a passive scalar in an isotropic turbulent flow in the presence of a time-periodic forcing. The results corroborate recent analytical predictions on the frequency dependence of the scalar variance and dissipation. In particular, when the modulation amplitude is large, it is shown that a low frequency modulation diminishes the mixing efficiency, whereas it enhances the transfer rate of kinetic energy.

I. INTRODUCTION

Is it possible to enhance the mixing efficiency of a turbulent flow by adding a periodic modulation to the mixing protocol? That is the main question we address in this investigation by considering the academic case of isotropic turbulence mixing a passive scalar.

The mixing rate of a scalar quantity advected by a fluid is a key quantity in a wide range of applications. Increasing the mixing rate by changing the flow properties can have far reaching consequences in process-optimization. Whereas the mixing in laminar flows can often be studied analytically, and the mixing rate can be greatly enhanced by changing the boundary conditions[1] or the time-dependence of the flow[2], the turbulent case is in general far more complicated. It is not even known if it is possible to affect, in a controlled way, the mixing of a turbulent flow by changing the large-scale forcing.

If any understanding of the modification of turbulent mixing through time-dependent forcing is to be obtained, we think it is compulsory to look at the most simplified case. We consider therefore the academic case of periodically forced isotropic turbulence, advecting a passive scalar.

The influence of a time-periodic forcing on the turbulence itself is a relatively young problem, despite its obvious academic interest. Indeed, first results on the response of a turbulent velocity field on a time-periodic isotropic forcing were obtained in the beginning of the 2000s. The initial studies aimed at identifying a possible resonance in the energy transfer process[3–5]. Direct numerical simulations[6,7] and experiments[8,9] were carried out to systematically investigate the response of the kinetic energy and dissipation rate to the forcing frequency. Analytical studies, using two-point closure techniques, allowed to explain the different scaling regimes of the time-dependent quantities[10] and assess he ability of engineering models to reproduce the different features[11].

Obviously it is extremely interesting to transpose these ideas to turbulent mixing. Inspired by the results in[6], the application of particular forcing schemes to influence turbulent mixing was considered in[12]. In that study the forcing was introduced in different wavenumber bands in Fourier space to mimic the complex nature of turbulent flows generated by realistic objects. The influence of the so-generated flow on turbulent mixing was assessed by monitoring the wrinkling of level-sets of an advected scalar. Those results inspired several experimental investigations with application to turbulent combustion (see for instance[13,14]). In[12] the spatial character of the forcing was modified, but no temporal modulation was applied. In the experiments the modulation was both spatial and temporal, and it is not straightforward to disentangle the different effects, so that it is not clear whether the observed effects were caused by the time-periodic nature of the experimental inlet conditions or the spatial complexity of the latter. The influence of the geometry of a large-scale forcing on mixing has thus already received some attention, but the temporal modulation of the flow was not considered in these studies.

In a recent paper[15], we carried out an analytical study of such a case: mixing in periodically forced turbulence. We showed that the second-order contributions of a perturbation analysis of the nonlinear transfer with respect to a modulation of the velocity forcing will lead to (1) an enhanced energy transfer (2) a reduced scalar transfer. Since the study was based on a simple turbulence closure and the perturbation analysis assumed small modulation amplitude, it is important to check the results in a more realistic setting, where the Navier-Stokes and advection-diffusion equations are not modeled, but directly evaluated. That is what will be done in the present investigation.

In the next section (section II) we will outline the strategy to assess the influence of a periodic forcing on the mixing of a passive scalar, we will recall the analytical results and discuss the numerical tools. Then, in section III we will show and discuss the results, before concluding in section IV.

II. DEFINITIONS, PREDICTIONS AND NUMERICAL SET-UP

A. Description of the problem

We consider the Navier-Stokes equations for incompressible flow $\boldsymbol{u}$, mixing a passive scalar θ:

$$\frac{\partial}{\partial t}\boldsymbol{u} + \boldsymbol{u}\cdot\nabla\boldsymbol{u} = -\nabla P + \nu\nabla^2\boldsymbol{u} + \boldsymbol{f} \tag{1}$$

$$\nabla\cdot\boldsymbol{u} = 0 \tag{2}$$

$$\frac{\partial}{\partial t}\theta + \boldsymbol{u}\cdot\nabla\theta = D\nabla^2\theta + g, \tag{3}$$

where P is the pressure (normalized by a uniform density), ν and D are kinematic viscosity and diffusivity, respectively. The flow and the scalar field are kept in a statistically stationary state through an energy and scalar variance input $\boldsymbol{f}$, g, chosen such that ensemble averaging (or phase-averaging) yields,

$$\langle f_i u_i \rangle = \overline{p} + \tilde{p}\cos(\omega t), \tag{4}$$
$$\langle g\theta \rangle = \overline{p}_\theta + \tilde{p}_\theta \cos(\omega t), \tag{5}$$

where the quantities p and p_θ denote the average kinetic energy and scalar variance injection rates. Overlined quantities denote time-averages and tilded quantities denote a periodic (non-zero frequency phase-averaged) contribution. The precise form of the forcing is given in the appendix. In our study the flow domain is a spatially periodic box. In the present setting the evolution equations for the kinetic energy $k = \frac{1}{2}\left\langle |\boldsymbol{u}|^2 \right\rangle$ and the variance of the scalar $k_\theta = \frac{1}{2}\left\langle \theta^2 \right\rangle$ reduce to

$$\frac{dk}{dt} = p - \epsilon \tag{6}$$
$$\frac{dk_\theta}{dt} = p_\theta - \epsilon_\theta. \tag{7}$$

In these equations ϵ and ϵ_θ are the phase averaged dissipation of kinetic energy and scalar variance, respectively. All the different statistical quantities of interest will in the following be decomposed into a time-averaged and a periodic component. The time-averaged balance equations for the kinetic energy and scalar variance are given by

$$0 = \overline{p} - \overline{\epsilon} \tag{8}$$
$$0 = \overline{p}_\theta - \overline{\epsilon}_\theta, \tag{9}$$

and the periodic quantities evolve according to

$$-\omega\tilde{k}\sin(\omega t + \phi_k) = \tilde{p}\cos(\omega t) - \tilde{\epsilon}\cos(\omega t + \phi_\epsilon) \tag{10}$$
$$-\omega\tilde{k}_\theta \sin(\omega t + \phi_{k_\theta}) = \tilde{p}_\theta \cos(\omega t) - \tilde{\epsilon}_\theta \cos(\omega t + \phi_{\epsilon_\theta}) \tag{11}$$

In these expressions, we have assumed that all quantities will periodically oscillate around a mean value with a period ω. In previous works,[4–7,10], the frequency dependence of $\tilde{k}$ and $\tilde{\epsilon}$ was investigated. The influence of the modulation on the time-averaged quantities $\overline{k}$ and $\overline{\epsilon}$ has not received any attention yet, in particular since a linear perturbation analysis does not show any influence of the modulation on the averages. It is however these average quanties that quantify the transfer efficiency. Indeed one can introduce the transfer efficiency of kinetic energy χ as the inverse of the integral timescale

$$\chi = \frac{\overline{\epsilon}}{\overline{k}}. \tag{12}$$

The value of χ measures the efficiency of the energy transfer through the energy cascade.

In order to measure the transfer efficiency of the passive scalar, one can define the mixing rate χ_θ,

$$\chi_\theta = \frac{\overline{\epsilon}_\theta}{\overline{k}_\theta}, \tag{13}$$

measuring the efficiency of a flow to transfer scalar variance to diffusivity-dominated scales, or in other words, the mixing efficiency.

B. Summary of analytical results

We will recall the predictions, obtained by a linear perturbation analysis of the spectral transfer [10] and [15]. First, in [10] we derived, using spectral closure, the frequency dependence of the modulated part of the kinetic energy $\tilde{k}$ and viscous dissipation $\tilde{\epsilon}$. In the low frequency, or quasistatic limit, both quantities were predicted to tend to constant values, independent of the frequency,

$$\tilde{\epsilon} = \tilde{p} \tag{14}$$
$$\tilde{k} = \frac{2}{3}\alpha_p \bar{k}, \tag{15}$$

where the relative forcing amplitude is defined by

$$\alpha_p = \frac{\tilde{p}}{\bar{p}}. \tag{16}$$

For large frequencies an asymptotic power-law dependence was derived of the form

$$\tilde{k} \sim \alpha_p \bar{k}(\omega T)^{-1} \quad \text{for} \quad \omega T \gg 1 \tag{17}$$
$$\tilde{\epsilon} \sim \alpha_p \bar{\epsilon}(\omega T)^{-3} \quad \text{for} \quad 1 \ll \omega T \ll R_\lambda \tag{18}$$
$$\tilde{\epsilon} \sim \alpha_p \bar{\epsilon} R_\lambda^{-2}(\omega T)^{-1} \quad \text{for} \quad \omega T \gg R_\lambda \tag{19}$$

We will start by re-assessing these results in section III A.

In[15] we have addressed the case of a passive scalar mixed by a modulated turbulence analytically. The simplest spectral closure for nonlinear transfer of energy and scalar variance was used to obtain predictions on the different quantities, for the case in which the modulation was only applied to the forcing of the velocity field. Since the scalar forcing does in this case not contain a time-periodic component, the equation for the modulated scalar variance is,

$$-\omega\tilde{k}_\theta \sin(\omega t + \phi_{k_\theta}) = -\tilde{\epsilon}_\theta \cos(\omega t + \phi_{\epsilon_\theta}). \tag{20}$$

From this equation it is not obvious that the scalar should contain a periodic component. Indeed from (20), taking the modulus, we find that

$$\omega|\tilde{k}_\theta| = |\tilde{\epsilon}_\theta|. \tag{21}$$

No further information can be obtained from these equations about the frequency dependence of $\tilde{k}_\theta$. Obviously, $\tilde{k}_\theta = 0$ is a possible solution of these equations. But since the velocity field advecting the scalar contains a periodic contribution, it is not excluded that a periodic contribution is observed in the scalar dynamics. It is shown in[15] that the scalar statistics are indeed affected by the velocity modulation in a non-trivial way. The resulting linear response to the modulation is

$$\tilde{k}_\theta \sim \alpha_p \bar{k}_\theta(\omega T)^{-2} \quad \text{for} \quad \omega T \gg 1 \tag{22}$$
$$\tilde{\epsilon}_\theta \sim \alpha_p \bar{\epsilon}_\theta(\omega T)^{-3} \quad \text{for} \quad \omega T \gg 1, \tag{23}$$

and this will here be verified numerically.

More importantly, retaining second-order contributions in the perturbation analysis, we obtained in reference[15] estimates of the influence of the modulation on the time-averaged quantities, χ and χ_θ. The derived expressions in the low ω limit are

$$\frac{\chi}{\chi(\tilde{p}=0)} = \left(1 + \frac{1}{12}\alpha_p^2\right)^{2/3}. \tag{24}$$

and

$$\frac{\chi_\theta}{\chi_\theta(\tilde{p}=0)} = \frac{\left(1 - \frac{1}{12}\alpha_p^2\right)}{\left(1 + \frac{1}{12}\alpha_p^2\right)^{1/3}}, \tag{25}$$

where $\chi(\tilde{p}=0)$ and $\chi_\theta(\tilde{p}=0)$ are the transfer efficiencies in the absence of modulation. These expressions show that a modulation of the forcing can influence the average value of the transfer efficiency. For the kinetic energy transfer χ, this effect is positive, whereas for the scalar mixing rate this effect is negative. These expressions also show that the relative strength of the forcing, $\alpha_p = \tilde{p}/\overline{p}$ must be large for the modulation to affect the transfer rates significantly. To illustrate: for $\alpha_p = 0.2$, it is found that $\chi/\chi(\tilde{p}=0) = 1.002$ and $\chi_\theta/\chi_\theta(\tilde{p}=0) = 0.996$, whereas these values change to 1.05 and 0.89 respectively for $\alpha_p = 1$.

This is a major result, since the analytical predictions suggest that we can affect the mixing efficiency of a turbulent flow by modulating the energy input. However, the way in which a modulation affects the average transfer rates is not what is desirable in most applications. In general one would prefer the opposite situation where a modification of the mixing protocol would lead to a consumption of less kinetic energy to mix better. The analytical results suggest that a slow modulation will lead to more kinetic energy transfer, for a less efficient scalar transfer.

Since these predictions were obtained using a second-order perturbation of a simplified transfer model, it is important to check them numerically. Indeed, within the framework of a perturbation analysis, we consider that we measure the response of a system to an infinitesimal perturbation. In the case of a periodic perturbation the response is assumed to be at the same frequency as the perturbation, around the unaltered system. When the perturbation is large, the system itself can be affected importantly, and linear-response theory is no longer valid. In our case, a perturbation of the injection with an amplitude equal to the average injection cannot possibly be considered infinitesimal. It is therefore interesting to see if such a perturbation modifies the time-averaged properties of the flow, as suggested by expressions (24) and (25), obtained, as we said, from a second-order perturbation analysis.

C. Numerical set-up

A standard pseudospectral method is used to compute the velocity and scalar field in a space-periodic cubic domain of size 2π. A conventional 2/3 wavenumber truncation is used to eliminate the aliasing error and a third order Runge-Kutta, Total Variation Diminishing scheme is used as time discretisation. The same code was used in ref.[16] to study the mixing of temperature fluctuations in isotropic turbulence.

A total number of 46 simulations is carried out at two different values of the Taylor-scale Reynolds number, $R_\lambda = 32$ and 105. A challenge in the study of the frequency response of turbulent flows is the convergence of the statistics. At low forcing frequencies the simulations become very long if a sufficient number of periods is to be resolved. At high frequencies the response to a periodic forcing will be shown to be small, so that also in this case long simulations are needed, not to resolve sufficient periods, but to be able to distinguish the frequency response from the turbulent fluctuations. Obtaining converged statistics is therefore challenging in both the small and large frequency limits.

Details on the numerical parameters and on the post-processing procedure are given in the Appendix.

III. RESULTS

Two different cases will be considered: the case of mixing in a modulated turbulent velocity field ($\tilde{p} \neq 0$ and $\tilde{p}_\theta = 0$) and the case where only the scalar injection is modulated ($\tilde{p} = 0$ and $\tilde{p}_\theta \neq 0$).

A. Response of turbulence and mixing on a periodic kinetic energy input

In this section we consider the case where we only modulate the kinetic energy,

$$p = \overline{p} + \tilde{p}\cos(\omega t), \tag{26}$$

$$p_\theta = \overline{p_\theta}. \tag{27}$$

It will be shown that the modulation $\tilde{p}$ of the velocity field does also affect the mixing of the passive scalar.

1. Frequency response of the modulated kinetic energy and dissipation

The frequency response of $\tilde{k}$ and $\tilde{\epsilon}$ is shown in Fig. 1 for $R_\lambda = 32$. We compare in this figure the frequency responses for two different relative forcing amplitudes, $\alpha_p = \tilde{p}/\overline{p} = 0.2$ and $\alpha_p = 1$. In order to compare the frequency response for the different forcing amplitudes,

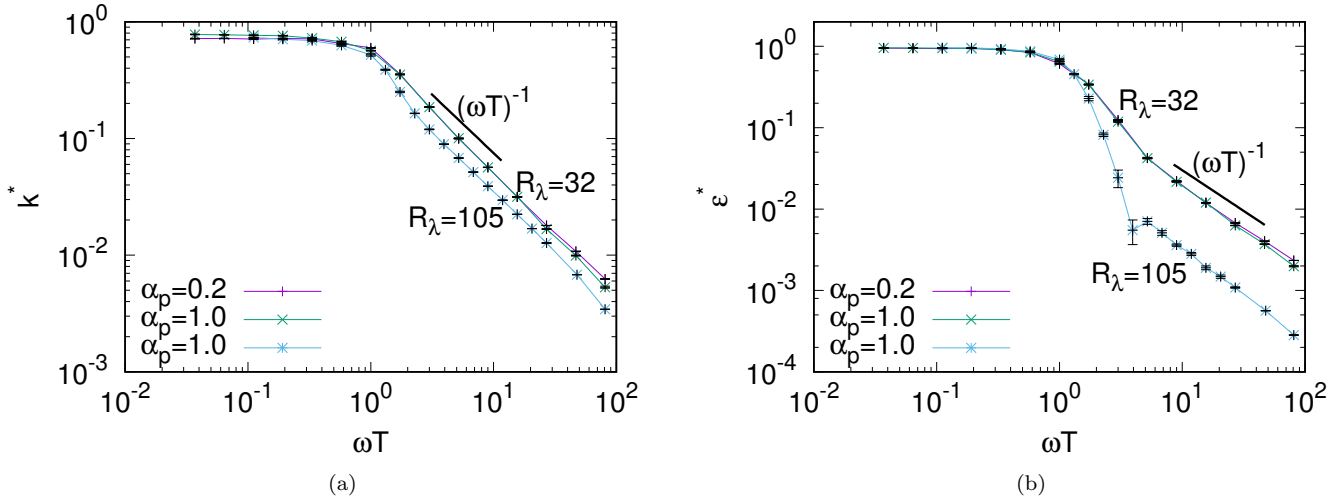

(a) (b)

FIG. 1: The frequency dependence of (a) $k^* = \frac{\tilde{k}}{\overline{k}}\alpha_p^{-1}$ and (b) $\epsilon^* = \frac{\tilde{\epsilon}}{\overline{\epsilon}}\alpha_p^{-1}$ as a function of ωT for $R_\lambda = 32$ and $R_\lambda = 105$, $\alpha_p = 0.2$ and $\alpha_p = 1$.

we plot in these figures the quantities

$$k^* = \alpha_p^{-1}\frac{\tilde{k}}{\overline{k}} \quad \text{and} \quad \epsilon^* = \alpha_p^{-1}\frac{\tilde{\epsilon}}{\overline{\epsilon}} \tag{28}$$

as a function of frequency. Several observations can be made. Firstly, the 20% and 100% relative forcing amplitudes give results that superpose at almost all frequencies for both quantities. These observations seem to indicate that the results of the linear-perturbation analysis are robust enough to be transposable to the case where $\alpha_p = 1$, i.e., the case where the modulation amplitude has the same value as the mean value. Numerically, this is convenient, since the $\alpha_p = 1$ results allow to obtain results at a lower computational cost, and therefore, at higher Reynolds number, because the signal-to-noise ratio is larger.

Secondly, the powerlaw dependence proportional to ω^{-1} observed in[6] and[10] is clearly reproduced both for $\tilde{k}$ and $\tilde{\epsilon}$. At small frequencies both $\tilde{k}$ and $\tilde{\epsilon}$ tend to constant values, as predicted in[10], but unlike the DNS results in[6] at these frequencies, perhaps due to unconverged statistics in their simulations. Indeed, in[6], a local maximum was observed at low frequencies, suggestive of a resonance. This effect is not observed in our results, neither was it in the closure studies[10].

Furthermore, Figure 1 also illustrates the influence of the Reynolds number on the modulated kinetic energy and dissipation. It is observed that this influence is small for the modulated kinetic energy. However, for the dissipation this influence is larger, as was explained in[10] by the fact that the ω^{-1} asymptote is inversely proportional to the Reynolds number, since it corresponds to the direct influence of the viscous damping on the forced scales (see expression (19)). The intermediate zone between the low frequency plateau and the high frequency asymptote was theoretically predicted to be proportional to ω^{-3} for large Reynolds numbers. This frequency range is too small here to be conclusive on the presence, or not, of such a power law.

2. Frequency response of the modulated scalar variance and its dissipation

The results on $\tilde{k}$ and $\tilde{\epsilon}$ in the foregoing section are in agreement with previous work (except for the small local maximum observed in[6]). In Figure 2 we evaluate quantities which have not received any attention yet in experiments and simulations: $\tilde{k}_\theta$ and $\tilde{\epsilon}_\theta$. It is observed that the large-frequency asymptotes (22) and (23) predicted in[15] are well reproduced. More precisely it is observed that the scalar variance contains a periodic component which is constant at low frequencies, and rapidly drops off at high frequencies, following a powerlaw proportional to ω^{-3}. The periodic part of the scalar dissipation is then determined by relation (21), as seems to be confirmed in figure 2, where for ω tending to zero $\tilde{\epsilon}_\theta$ is proportional to ω, and for large values of ω the asymptotic slope is proportional to ω^{-2}. It seems that the analytical predictions based on the linear perturbation of a simple flux closure for the nonlinear transfer is sufficient to predict the small and large frequency asymptotes of both $\tilde{k}_\theta$ and $\tilde{\epsilon}_\theta$.

3. Influence of the modulation on the mixing and transfer efficiencies

In Figure 3, the influence of the modulation is shown on the quantities χ and χ_θ. Our forcing scheme is de-

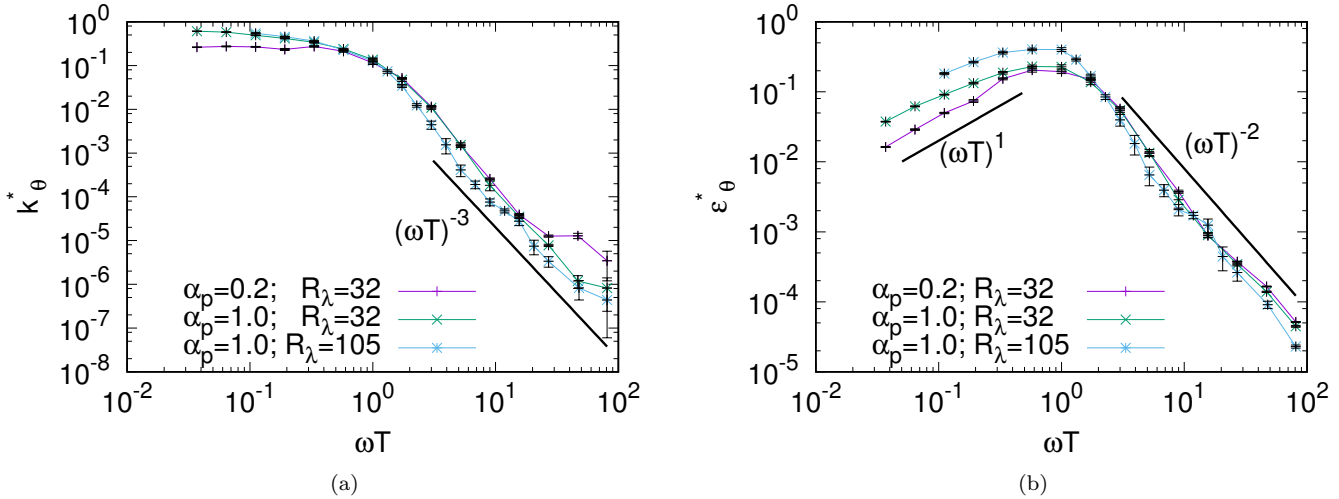

(a) (b)

FIG. 2: Frequency response of (a) the modulated scalar variance $k^*_\theta = \frac{\tilde{k}_\theta}{\bar{k}_\theta}\alpha_p^{-1}$ and (b) modulated scalar dissipation $\epsilon^*_\theta = \frac{\tilde{\epsilon}_\theta}{\bar{\epsilon}_\theta}\alpha_p^{-1}$ for $R_\lambda = 32$ and $R_\lambda = 105$. The relative forcing amplitude is $\alpha_p = 1$.

signed to keep the average rate of ϵ and ϵ_θ constant. Thereby, in none of our simulations, the values of $\bar{\epsilon}(\omega)$ and $\bar{\epsilon}(\tilde{p} = 0)$ differ more than 2%. The transfer and mixing efficiency are then determined by the variations in $\bar{k}(\omega)$ and $\bar{k}_\theta(\omega)$ (see equations (12) and (13)). It is shown that for $\alpha_p = 0.2$, no clear modification of the mixing efficiency and transfer rate is observed. Indeed, the analytical study predicted the effect for this value of α_p to be less than 0.5%, well below the statistical errors induced by the time-averaging. However, for $\alpha_p = 1$, a clear effect is observed, of the order of +7% for χ and −20% for χ_θ. These are of the same order of magnitude, but slightly larger than the analytically predicted values $(+5\%, -11\%)$. Clearly the analytical study predicted the correct tendencies and order of magnitude of the influence of the modulation of the mixing and transfer rate. The fact that the numerical values are not exactly predicted cannot be considered very surprising given the nature of the simplifications in the analytical study. These results confirm thus that the modulation of the velocity field can affect the average transfer and mixing efficiencies. The Reynolds number does not seem to be an important parameter for the values we considered.

B. Modulation of the scalar injection

For completeness, we now consider the case where we only modulate the scalar input,

$$p = \overline{p}, \tag{29}$$

$$p_\theta = \overline{p_\theta} + \tilde{p}_\theta \cos(\omega t). \tag{30}$$

Naturally the modulation $\tilde{p}_\theta$ should not influence the velocity field and we therefore only evaluate the influence of the modulation on the scalar quantities.

In Figure 4 we show the results for $k^*_\theta = \alpha_p^{-1}\tilde{k}_\theta/\bar{k}_\theta$ and dissipation $\epsilon^*_\theta = \alpha_p^{-1}\tilde{\epsilon}_\theta/\bar{\epsilon}_\theta$ as a function of the modulation frequency for $\alpha_p = 1$, $R_\lambda = 32$ and $R_\lambda = 105$. A very close similarity with the results for k^* and ϵ^* in Figure 1 is observed. In particular the small and large frequency asymptotes are identical. Indeed, the reasonings leading to the prediction of the frequency behaviour of the kinetic energy and dissipation[10] can be extended to the case of the passive scalar, in particular in the limit of the linear response approximation.

IV. CONCLUSION

In this manuscript, we have answered to the question whether a periodic modulation of a turbulent flow changes its mixing properties. It was clearly shown that for large modulation amplitudes, the modulation affects the energy transfer positively, whereas it diminishes the mixing efficiency, as was predicted in a recent analytical study[15]. The average mixing rate was shown to decrease by approximately 20%, for two distinct Reynolds numbers, whereas the energy transfer rate increases by approximately 7%. This result shows that in most applications where an efficient mixing is required for a minimum amount of energy, the modulation of the velocity field is not a good idea. We should however mention that these results concern the case of isotropic turbulence and that a possible mixing enhancement by the modulation of spatially inhomogeneous mixing devices cannot be excluded. However, we show here that it is not the heart of the turbulent mechanism, the energy and scalar cascade, which is affected in the desired way by the modulation

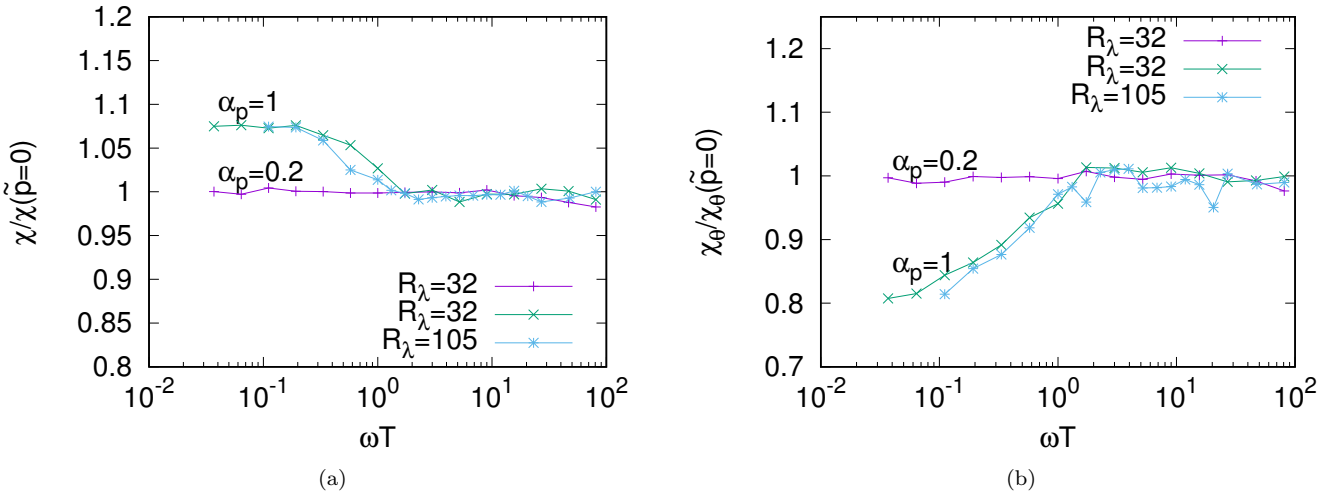

FIG. 3: Influence of the large-scale modulation on the transfer-rate χ and mixing-efficiency χ_θ, for $R_\lambda = 32$ and $R_\lambda = 105$, $\alpha_p = 0.2$ and $\alpha_p = 1$.

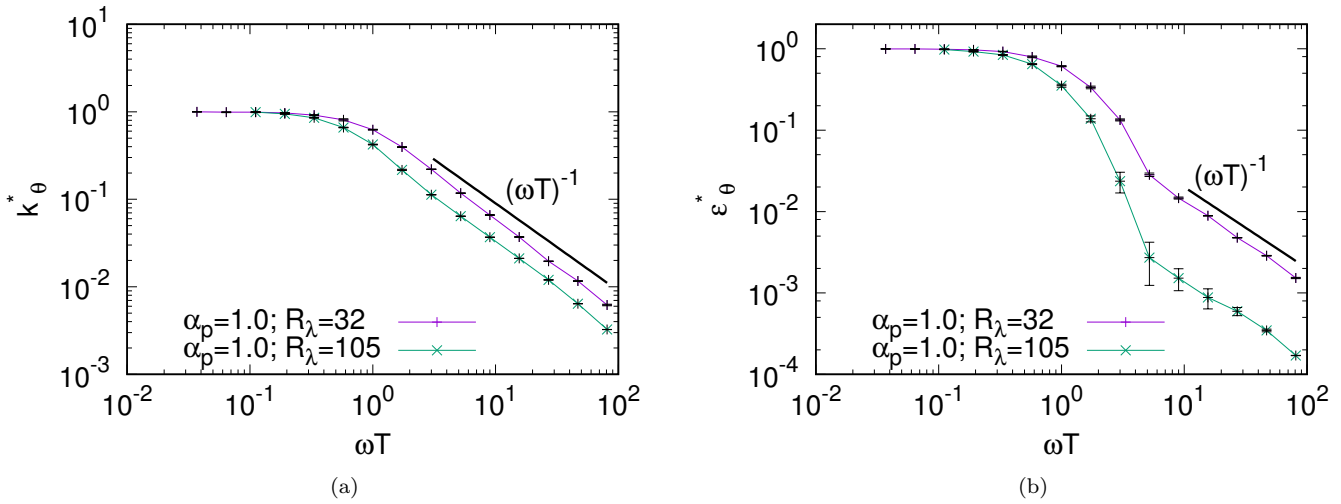

FIG. 4: Amplitudes of the modulated scalar variance $k^*_\theta = \frac{\tilde{k}_\theta}{\bar{k}_\theta}\alpha_p^{-1}$ and (b) modulated scalar dissipation $\epsilon^*_\theta = \frac{\tilde{\epsilon}_\theta}{\bar{\epsilon}_\theta}\alpha_p^{-1}$ as a function of ωT for the case of a modulated scalar injection. Results for $R_\lambda = 32$ and $R_\lambda = 105$, both at $\alpha_p = 1$.

of an isotropic forcing.

We further showed that in this large amplitude modulation regime the frequency response of the amplitudes of the periodical components of the kinetic energy, scalar variance and their dissipations are still in agreement with the outcome from linear perturbation analysis.

APPENDIX: FURTHER DETAILS ON THE NUMERICAL SIMULATIONS AND POSTPROCESSING PROCEDURE

The numerical simulations are carried out at two different resolutions, corresponding to different values of the Reynolds number. First, low resolution simulations at a spatial resolution of 64^3 are performed with kinematic viscosity $\nu = 0.009$, corresponding to a Taylor Reynolds number $Re_\lambda = 32$, with eddy turn-over time $T = 1.949$. The resolution allows to resolve the smallest scales upto $k_{max}\eta = 0.93$. Another set of simulations is carried out at a resolution of $N^3 = 256^3$ gridpoints, kinematic vis-

cosity $\nu = 0.0009$; Taylor Reynolds number $Re_\lambda = 105$; eddy turn-over time $T = 2.317$ and $k_{max}\eta = 0.97$. In all simulations the Schmidt number $Sc \equiv \nu/D = 1$. We think that the consideration of other values of Sc will not qualitatively alter the results, as long as $Pe = UL/D$ is sufficiently large for the advection to be dominant over diffusion.

The Fourier-transformed velocity and scalar field are denoted by $\hat{u}_i$ and $\hat{\theta}$, respectively. The forced Fourier-modes are the modes in the range $0.5 < |\boldsymbol{\kappa}| \leq 2.5$. Only for these modes the forcing terms are non-zero and have the form

$$\hat{f}_i(\boldsymbol{\kappa}, t) = \frac{1}{N_F} \frac{\hat{u}_i(\boldsymbol{\kappa}, t)}{|\hat{\boldsymbol{u}}(\boldsymbol{\kappa}, t)|^2} (\overline{p} + \tilde{p}\cos(\omega t)) \qquad (31)$$

$$\hat{g}(\boldsymbol{\kappa}, t) = \frac{1}{N_F} \frac{\hat{\theta}(\boldsymbol{\kappa}, t)}{\left|\hat{\theta}(\boldsymbol{\kappa}, t)\right|^2} (\overline{p}_\theta + \tilde{p}_\theta \cos(\omega t)), \qquad (32)$$

with N_F the total number of forced modes. These forcing schemes will result in a statistically isotropic velocity and scalar field.

Previous investigations[6,10] focused in particular on the linear response of turbulence on a periodic modulation. In this limit linearized equations around a given equilibrium allow to analytically derive certain results. The verification of such results is not straightforward in the nonlinear regime, where the perturbation is large. Ideally, to investigate the linear response of a turbulent flow, the amplitude of the forcing should be chosen small compared to the amplitude of the steady part of the forcing ($\alpha_p \equiv \tilde{p}/\bar{p} \ll 1$). However, since the turbulent fluctuations are in this case much larger than the periodic response, very long simulations should be carried out to obtain an estimate of the frequency response. In particular at large frequencies, where the frequency response will be shown to drop rapidly as a function of frequency this would impose prohibitively long computations. A compromise is to consider a larger modulation amplitude. In this study, as in[6], we use $\alpha_p \equiv \tilde{p}/\bar{p} = 0.2$. This allows to obtain converged statistics for a large range of frequencies at a reasonable computational cost for low Reynolds number ($R_\lambda = 32$). For higher Reynolds number this already leads to prohibitively long simulations. Therefore we have carried out another set of simulations with a relative modulation amplitude $\alpha_p = 1$. Even though this certainly violates the linear perturbation assumption, we will show that the frequency-response of the modulated quantities is not quantitatively altered. We will further show that this has an interesting direct influence on the time-averaged quantities.

Before extracting the frequency response of the simulations, the flow was simulated for approximately 10 eddy turn-over times to obtain a statistically steady state. It proved convenient to determine the amplitude of the periodic response by using a Fourier-transform of the signal. Before Fourier-transforming the time-series of a given quantity, a hanning window function is applied to the signal to eliminate the aliasing error at high frequencies due to the finite length of the signal. In the frequency spectra, if the simulations are carried out for a sufficiently long time-interval, the amplitude of the periodic response is easily identified by a sharp peak. Comparing the value of this peak to the neighbouring values in the spectrum gives a direct estimate of the signal-to-(turbulent)-noise ratio. In all simulations the value of the peak at the considered frequency was at least ten times the value of the neighbouring values in the spectra. For the phase averaged amplitudes, error-bars are added to the datapoints in the figures, computed from the signal to noise ratio. In most cases, this error-bar is smaller than the size of the symbols used in the figures. The time-averaged value is conveniently estimated from the $\omega = 0$ component of the spectrum.

The different simulations we have carried out are documented in table I.

ωT	N	t	α_p	R_λ
0	0	800	0.2	32
0.037	4	1316	0.2	32
0.064	8	1519	0.2	32
0.11	8	877	0.2	32
0.19	8	506	0.2	32
0.33	8	292	0.2	32
0.57	8	169	0.2	32
1	15	183	0.2	32
1.7	90	633	0.2	32
3	180	731	0.2	32
5	540	1266	0.2	32
9	360	487	0.2	32
16	810	633	0.2	32
27	1080	487	0.2	32
47	110	29	0.2	32
81	200	30	0.2	32
0	0	800	1	32
0.037	4	1316	1	32
0.064	8	1519	1	32
0.11	8	877	1	32
0.19	8	506	1	32
0.33	8	292	1	32
0.57	8	169	1	32
1	15	183	1	32
1.7	35	246	1	32
3	60	243	1	32
5	105	246	1	32
9	180	243	1	32
16	315	246	1	32
27	540	243	1	32
47	945	246	1	32
81	1800	271	1	32
0	0	40	1	105
0.11	2	262	1	105
0.19	3	227	1	105
0.33	3	131	1	105
0.57	3	76	1	105
1	2	29	1	105
1.7	6	50	1	105
3	12	58	1	105
5	54	151	1	105
9	108	175	1	105
16	54	50	1	105
27	108	58	1	105
47	162	50	1	105
81	324	58	1	105

TABLE I: Simulation parameters: normalized frequency ωT, number of simulated periods N, simulated time-interval t, relative forcing amplitude α_p and Reynolds number R_λ.

ACKNOWLEDGMENTS

All simulations were carried out using the facilities of the PMCS2I (École Centrale de Lyon).

[1] E. Gouillart, N. Kuncio, O. Dauchot, B. Dubrulle, S. Roux, and J.-L. Thiffeault, Walls inhibit chaotic mixing, Phys. Rev. Lett. **99**(11), 114501 (2007).

[2] H. Aref, Stirring by chaotic advection, J. Fluid Mech. **143**, 1 (1984).

[3] D. Lohse, Periodically kicked turbulence, Phys. Rev. E **62**, 4946 (2000).

[4] A. von der Heydt, S. Grossmann, and D. Lohse, Response maxima in modulated turbulence, Phys. Rev. E **67**, 046308 (2003).

[5] A. von der Heydt, S. Grossmann, and D. Lohse, Response maxima in modulated turbulence. II. Numerical simulations, Phys. Rev. E **68**, 066302 (2003).

[6] A. K. Kuczaj, B. J. Geurts, and D. Lohse, Response maxima in time-modulated turbulence: Direct numerical simulations, Europhys. Lett. **73**, 851 (2006).

[7] A. Kuczaj, B. Geurts, D. Lohse, and W. van de Water, Turbulence modification by periodically modulated scale-dependent forcing, Computers & Fluids **37**(7), 816–824 (2008).

[8] O. Cadot, J. Titon, and D. Bonn, Observation of resonances in modulated turbulence, J. Fluid Mech. **485**, 161 (2003).

[9] H. Cekli, C. Tipton, and W. van de Water, Resonant enhancement of turbulent energy dissipation, Phys. Rev. Lett. **105**(4), 044503 (2010).

[10] W. J. T. Bos, T. Clark, and R. Rubinstein, Small scale response and modeling of periodically forced turbulence, Phys. Fluids **19**, 055107 (2007).

[11] R. Rubinstein and W. J. T. Bos, On the unsteady behavior of turbulence models, Phys. Fluids **21**, 041701 (2009).

[12] A. K. Kuczaj and B. J. Geurts, Mixing in manipulated turbulence, J. Turbul. **7**, N67 (2006).

[13] A. Verbeek, G. Stoffels, R. Bastiaans, and T. van der Meer, Optimization of combustion in gas turbines by applying resonant turbulence, in *International Gas Union Research Conference, IGRC 2011*, Foundation IGRC, 2011.

[14] A. A. Verbeek, T. W. Bouten, G. G. Stoffels, B. J. Geurts, and T. H. van der Meer, Fractal turbulence enhancing low-swirl combustion, Combustion and Flame **162**(1), 129–143 (2015).

[15] W. Bos and R. Rubinstein, Mixing in modulated turbulence. Analytical results, Comput. Fluids **151**, 102 (2017).

[16] W. J. T. Bos, R. Chahine, and A. Pushkarev, On the scaling of temperature fluctuations induced by frictional heating, Phys. Fluids **24**, 015108 (2015).

Bibliography

[1] Vaclav Smil. *Energy Transitions: Global and National Perspectives.* 2016.

[2] Cia world factbook. *https://www.cia.gov/library/publications/the-world-factbook/geos/xx.html.*

[3] Jeffrey P Freidberg. *Plasma physics and fusion energy.* Cambridge university press, 2008.

[4] Fritz Wagner, G Becker, K Behringer, D Campbell, A Eberhagen, W Engelhardt, G Fussmann, O Gehre, J Gernhardt, G v Gierke, et al. Regime of improved confinement and high beta in neutral-beam-heated divertor discharges of the asdex tokamak. *Physical Review Letters*, 49(19):1408, 1982.

[5] D.F. Escande. What is a reversed field pinch? *https://hal.archives-ouvertes.fr/hal-00909102*, (2013).

[6] J.B. Taylor. Relaxation of toroidal plasma and generation of reverse magnetic fields. *Phys. Rev. Lett.*, 33, (1974).

[7] D. F. Escande, P. Martin, S. Ortolani, A. Buffa, P. Franz, L. Marrelli, E. Martines, G. Spizzo, S. Cappello, A. Murari, R. Pasqualotto, and P. Zanca. Quasi-single-helicity reversed-field-pinch plasmas. *Phys. Rev. Lett.*, 85:1662, (2000).

[8] P. Martin *et al.* Quasi-single helicity states in the reversed field pinch: Beyond the standard paradigm. *Phys. Plasmas*, 24, (2000).

[9] P. Martin *et al.* Overview of quasi-single helicity experiments in reversed field pinches. *Nucl. Fusion*, 43, (2003).

[10] L. Frassinetti, I. Predebon, H. Koguchi, Y. Yagi, Y. Hirano, H. Sakakita, G. Spizzo, and R.B. White. Improved particle confinement in transition from multiple-helicity to quasi-single-helicity regimes of a reversed-field pinch. *Phys. Rev. Lett.*, 97, (2006).

[11] D. Terranova, A. Alfier, F. Bonomo, P. Franz, P. Innocente, and R. Pasqualotto. Enhanced confinement and quasi-single-helicity regimes induced by poloidal current drive. *Phys. Rev. Lett.*, 99, (2007).

[12] M. D. Wyman *et al.* Plasma behaviour at high β and high density in the Madison Symmetric Torus RFP. *Phys. Plasmas*, 15, (2008).

[13] R. Lorenzini *et al.* Self-organized helical equilibria as a new paradigm for ohmically heated fusion plasmas. *Nature Phys.*, 5, (2009).

[14] P. Piovesan *et al.* Magnetic order and confinement improvement in high-current regimes of RFX-mod with MHD feedback control. *Nucl. Fusion*, 49, (2009).

[15] P. Piovesan *et al.* Influence of external 3D magnetic fields on helical equilibrium and plasma flow in RFX-mod. *Plasma Phys. Control. Fusion*, 53, (2011).

[16] P. Piovesan *et al.* RFX-mod: A multi-configuration fusion facility for three-dimensional physics studies. *Phys. Plasmas*, 20, (2013).

[17] Harold Grad and Hanan Rubin. Hydromagnetic equilibria and force-free fields. *Journal of Nuclear Energy (1954)*, 7(3-4):284–285, 1958.

[18] VD Shafranov. Plasma equilibrium in a magnetic field. *Reviews of Plasma Physics*, 2:103, 1966.

[19] EA Frieman and Liu Chen. Nonlinear gyrokinetic equations for low-frequency electromagnetic waves in general plasma equilibria. *Phys. Fluids*, 25, (1982).

[20] D.H.E. Dubin, J.A. Krommes, C. Oberman, and W.W. Lee. Nonlinear gyrokinetic equations. *Phys. Fluids*, 26, (1983).

[21] Y Sarazin, V Grandgirard, J Abiteboul, S Allfrey, X Garbet, Ph Ghendrih, G Latu, A Strugarek, G Dif-Pradalier, PH Diamond, et al. Predictions on heat transport and plasma rotation from global gyrokinetic simulations. *Nuclear Fusion*, 51(10):103023, 2011.

[22] SI Braginskii. Transport processes in a plasma. *Reviews of plasma physics*, 1, (1965).

[23] J. P. Freidberg. Ideal magnetohydrodynamics theory of magnetic fusion systems. *Rev. Mod. Phys.*, 54(3), (1982).

[24] David Montgomery and SHAN XIAOWEN. Toroidal resistive mhd equilibria. *Comments on Plasma Physics and Controlled Fusion*, 15, (1994).

[25] Jorge A Morales, Wouter JT Bos, Kai Schneider, and David C Montgomery. Intrinsic rotation of toroidally confined magnetohydrodynamics. *Physical review letters*, 109, (2012).

[26] D.C. Robinson. Tearing-mode-stable diffuse-pinch configurations. *Nucl. Fusion*, 18(7), (1978).

[27] LS Solov'ev. Hydromagnetic stability of a plasma in a quasi-uniform magnetic field. *Soviet Physics JETP*, 26, (1968).

[28] L Woltjer. Hydromagnetic equilibrium ii. stability in the variational formulation. *Proceedings of the National Academy of Sciences*, 45, (1959).

[29] HK Moffatt and A Tsinober. Helicity in laminar and turbulent flow. *Annual review of fluid mechanics*, 24(1):281–312, 1992.

[30] A. Reiman. Taylor relaxation in a torus of arbitrary aspect ratio and cross section. *Phys. Fluids*, 24, (1981).

[31] S Cappello and R Paccagnella. Proceedings of the workshop on theory of fusion plasmas, (1990).

[32] S Cappello and R Paccagnella. Nonlinear plasma evolution and sustainment in the reversed field pinch. *Physics of Fluids B: Plasma Physics*, 4, (1992).

[33] John M Finn, Rick Nebel, and Charles Bathke. Single and multiple helicity ohmic states in reversed-field pinches. *Physics of Fluids B: Plasma Physics*, 4, (1992).

[34] S. Cappello and D. F. Escande. Bifurcation in viscoresistive MHD: The hartmann number and the reversed field pinch. *Phys. Rev. Lett.*, 85, (2000).

[35] L Marrelli, P Martin, G Spizzo, P Franz, BE Chapman, D Craig, JS Sarff, TM Biewer, SC Prager, and JC Reardon. Quasi-single helicity spectra in the madison symmetric torus. *Phys. Plasmas*, 9, (2002).

[36] P Piovesan, G Spizzo, Y Yagi, H Koguchi, T Shimada, Y Hirano, and P Martin. Self-organization towards helical states in the toroidal pinch experiment reversed-field pinch. *Phys. Plasmas*, 11, (2004).

[37] Lorenzo Frassinetti, Per R Brunsell, James R Drake, Sheena Menmuir, and Marco Cecconello. Spontaneous quasi single helicity regimes in extrap t2r reversed-field pinch. *Phys. Plasmas*, 14, (2007).

[38] DF Escande, R Paccagnella, S Cappello, C Marchetto, and F D'Angelo. Chaos healing by separatrix disappearance and quasisingle helicity states of the reversed field pinch. *Phys. Rev. Lett.*, 85, (2000).

[39] P Franz, L Marrelli, P Piovesan, I Predebon, F Bonomo, Lorenzo Frassinetti, P Martin, G Spizzo, BE Chapman, D Craig, et al. Tomographic imaging of resistive mode dynamics in the madison symmetric torus reversed-field pinch. *Phys. Plasmas*, 13:012510, (2006).

[40] D Bonfiglio, S Cappello, and DF Escande. Dominant electrostatic nature of the reversed field pinch dynamo. *Phys. Rev. Lett.*, 94, (2005).

[41] J. B. Taylor. Relaxation and magnetic reconnection in plasmas. *Rev. Mod. Phys.*, 58, (1986).

[42] Susanna Cappello, D Bonfiglio, DF Escande, SC Guo, A Alfier, R Lorenzini, and RFX Team. The reversed field pinch toward magnetic order: a genuine self-organization. In *AIP Conference Proceedings*, volume 1069, pages 27–39, ()2008).

[43] S. Futatani, J. A. Morales, and W. J.T. Bos. Dynamic equilibria and magnetohydrodynamic instabilities in toroidal plasmas with non-uniform transport coefficients. *Phys. Plasmas*, 22, (2015).

[44] C. Canuto, M. Hussaini, A. Quarteroni, and T. Zang. *Spectral Methods in Fluid Dynamics*. Springer, 1987.

[45] J. A. Morales, M. Leroy, W. J.T. Bos, and K. Schneider. Simulation of confined magnetohydrodynamic flows with Dirichlet boundary conditions using a pseudo-spectral method with volume penalization. *J. Comp. Phys.*, 274, (2014).

[46] J. A. Morales, W. J.T. Bos, K. Schneider, and D. Montgomery. On the effect of toroidicity on reversed field pinch dynamics. *Plasma Phys. Control. Fusion*, 56, (2014).

[47] J. A. Morales. *Confined magnetohydrodynamics applied to magnetic fusion plasmas*. PhD thesis, Ecole Centrale de Lyon, (2013).

[48] Dmitry Kolomenskiy and Kai Schneider. A fourier spectral method for the navier–stokes equations with volume penalization for moving solid obstacles. *Journal of Computational Physics*, 228(16), (2009).

[49] G Allen Gary. Plasma beta above a solar active region: rethinking the paradigm. *Solar Physics*, 203(1):71–86, 2001.

[50] JA Wesson. Hydromagnetic stability of tokamaks. *Nuclear Fusion*, 18(1):87, 1978.

[51] R. Paccagnella, A. Bondeson, and H. Lütjens. Ideal toroidal stability beta limits and shaping effect for reversed field pinch configurations. *Nucl. Fusion*, 31(10), (1991).

[52] Magali Muraglia, Olivier Agullo, Masatoshi Yagi, Sadruddin Benkadda, P Beyer, Xavier Garbet, S-I Itoh, Kimitaka Itoh, and Abhijit Sen. Effect of the curvature and the β parameter on the nonlinear dynamics of a drift tearing magnetic island. *Nuclear Fusion*, 49(5):055016, 2009.

[53] D Bonfiglio, M Veranda, S Cappello, DF Escande, and L Chacón. Experimental-like helical self-organization in reversed-field pinch modeling. *Physical review letters*, 111(8):085002, 2013.

[54] M Veranda, D Bonfiglio, S Cappello, L Chacón, and DF Escande. Impact of helical boundary conditions on nonlinear 3d magnetohydrodynamic simulations of reversed-field pinch. *Plasma Physics and Controlled Fusion*, 55(7):074015, 2013.

[55] D Bonfiglio, M Veranda, S Cappello, L Chacón, and DF Escande. Sawtooth mitigation in 3d mhd tokamak modelling with applied magnetic perturbations. *Plasma Physics and Controlled Fusion*, 59(1):014032, 2016.

[56] Lodewijk Woltjer. A theorem on force-free magnetic fields. *Proceedings of the National Academy of Sciences*, 44(6):489–491, 1958.

[57] Arkady Tsinober, Prakash Vedula, and PK Yeung. Random taylor hypothesis and the behavior of local and convective accelerations in isotropic turbulence. *Physics of Fluids*, 13(7):1974–1984, 2001.

[58] Mark Nelkin. Universality and scaling in fully developed turbulence. *Advances in physics*, 43(2):143–181, 1994.

[59] AY Aydemir, DC Barnes, EJ Caramana, AA Mirin, RA Nebel, DD Schnack, and AG Sgro. Compressibility as a feature of field reversal maintenance in the reversed-field pinch. *The Physics of fluids*, 28(3):898–902, 1985.

[60] F. Troyon, R. Gruber, H. Saurenmann, S. Semenzato, and S. Succi. MHD-limits to plasma confinement. *Plasma Phys. Control. Fusion*, 26, (1984).

[61] A.F. Almagri, S. Assadi, R.N. Dexter, S.C. Prager, J.S. Sarff, and J.C. Sprott. *Nucl. Fusion*, 27, (1987).

[62] A.A.M. Oomens, H.S. Lassing, and A.F.G. Van Der Meer. Reversed Field Pinch discharges with elongated minor cross-section. *Rijnhuizen report 90-197*, (1990).

[63] S.C. Guo, X.Y. Xu, Z.R. Wang, and Y.Q. Liu. Does shaping bring an advantage for reversed field pinch plasmas? *Nucl. Fusion*, 53, (2013).

[64] S Cappello and D Biskamp. Reconnection processes and scaling laws in reversed field pinch magnetohydrodynamics. *Nucl. Fusion*, 36:571, 1996.

[65] John M Finn, Rick Nebel, and Charles Bathke. Single and multiple helicity ohmic states in reversed-field pinches. *Physics of Fluids B: Plasma Physics*, 4(5):1262–1279, 1992.

[66] D Bonfiglio, S Cappello, and DF Escande. Impact of a uniform plasma resistivity in mhd modelling of helical solutions for the reversed field pinch dynamo. *arXiv preprint arXiv:1603.03563*, 2016.

[67] A. Reiman. Minimum energy state of a toroidal discharge. *Phys. Fluids*, 23, (1980).

[68] S.A. Thorpe. Turbulence and mixing in a Scottish loch. *Phil. Trans. Roy. Soc. London A*, 286:125–181, (1977).

[69] D. Montgomery. Magnetohydrodynamic stability thresholds as a function of Hartmann number and pinch ratio. *Plasma Phys. Control. Fusion*, 34, (1992).

[70] D. Montgomery. Hartmann, Lundquist, and Reynolds: the role of dimensionless numbers in nonlinear magnetofluid behavior. *Plasma Phys. Control. Fusion*, 35, (1993).

[71] X. Shan and D. Montgomery. On the role of the Hartmann number in magnetohydrodynamic activity. *Plasma Phys. Control. Fusion*, 35, (1993).

[72] G. H. Keetels, H. J. H. Clercx, and G. J. F. van Heijst. Spontaneous angular momentum generation of two-dimensional fluid flow in an elliptic geometry. *Phys. Rev. E*, 78, (2008).

[73] W. J. T. Bos, S. Neffaa, and K. Schneider. Self-organization and symmetry-breaking in two-dimensional plasma turbulence. *Phys. Plasmas*, 17, (2010).

[74] George Backus. A class of self-sustaining dissipative spherical dynamos. *Annals of Physics*, 4(4):372–447, 1958.

[75] S Childress. A class of solutions of the magnetohydrodynamic dynamo problem. *The Application of Modern Physics to the Earth and Planetary Interiors*, pages 629–648, 1969.

[76] Yu B Ponomarenko. Theory of the hydromagnetic generator. *Journal of Applied Mechanics and Technical Physics*, 14(6), 1973.

[77] Gareth O Roberts. Spatially periodic dynamos. *Philosophical Transactions of the Royal Society of London A: Mathematical, Physical and Engineering Sciences*, 266(1179), 1970.

[78] TG Cowling. Mon not r astron soc. *Mon. Not. R. Astron. Soc.*, 94:39, 1934.

[79] Henry K Moffatt. *Field generation in electrically conducting fluids*. Cambridge University Press, Cambridge, London, New York, Melbourne, 1978.

[80] Wolfgang Dobler, Peter Frick, and Rodion Stepanov. Screw dynamo in a time-dependent pipe flow. *Physical Review E*, 67(5):056309, 2003.

[81] A Chupin, P Frick, and R Stepanov. The screw dynamo in a thick torus. *Astronomische Nachrichten*, 332(1):11–16, 2011.

[82] Norbert Seehafer. Nature of the α effect in magnetohydrodynamics. *Physical review E*, 53(1), 1996.

[83] Chris A Jones. Dynamo theory. *Dynamos (P. Cardin and L. Cugliandolo, eds.)*, 88:45–137, 2007.

[84] Agris Gailitis, Olgerts Lielausis, Sergej Dement'ev, Ernests Platacis, Arnis Cifersons, Gunter Gerbeth, Thomas Gundrum, Frank Stefani, Michael Christen, Heiko Hänel, et al. Detection of a flow induced magnetic field eigenmode in the riga dynamo facility. *Physical Review Letters*, 84(19), 2000.

[85] Agris Gailitis, Olgerts Lielausis, Ernests Platacis, Sergej Dement'ev, Arnis Cifersons, Gunter Gerbeth, Thomas Gundrum, Frank Stefani, Michael Christen, and Gotthard Will. Magnetic field saturation in the riga dynamo experiment. *Physical Review Letters*, 86(14), 2001.

[86] Robert Stieglitz and Ulrich Müller. Experimental demonstration of a homogeneous two-scale dynamo. *Physics of Fluids*, 13(3), 2001.

[87] Romain Monchaux, Michaël Berhanu, Mickaël Bourgoin, Marc Moulin, Ph Odier, J-F Pinton, Romain Volk, Stéphan Fauve, Nicolas Mordant, François Pétrélis, et al. Generation of a magnetic field by dynamo action in a turbulent flow of liquid sodium. *Physical review letters*, 98(4), 2007.

[88] Michaël Berhanu, Romain Monchaux, Stéphan Fauve, Nicolas Mordant, François Pétrélis, Arnaud Chiffaudel, François Daviaud, Bérengère Dubrulle, Louis Marié, Florent Ravelet, et al. Magnetic field reversals in an experimental turbulent dynamo. *EPL (Europhysics Letters)*, 77(5), 2007.

[89] Romain Monchaux, Michael Berhanu, Sébastien Aumaître, Arnaud Chiffaudel, François Daviaud, Bérengère Dubrulle, Florent Ravelet, Stephan Fauve, Nicolas Mordant, François Pétrélis, et al. The von kármán sodium experiment: Turbulent dynamical dynamos. *Physics of Fluids*, 21(3), 2009.

[90] Gary A Glatzmaier and Paul H Roberts. computer simulation of a geomagnetic field reversal. *Nature*, 377, 1995.

[91] Yannick Ponty, PD Mininni, DC Montgomery, J-F Pinton, Hélene Politano, and Annick Pouquet. Numerical study of dynamo action at low magnetic prandtl numbers. *Physical Review Letters*, 94(16):164502, 2005.

[92] E.J. Caramana and D.A. Baker. The dynamo effect in sustained Reversed-Field Pinch discharges. *Nucl. Fusion*, 24(4), (1984).

[93] H.A.B. Bodin and A.A. Newton. Reversed-field-pinch research. *Nucl. Fusion*, 20(4), (1980).

[94] R.G. Watt and R.A. Nebel. Sawteeth, magnetic disturbances, and magnetic flux regeneration in the reversed field pinch. *Phys. Fluids*, 26(4), (1983).

[95] H. Ji *et al.* Effect of collisionality and diamagnetism on the plasma dynamo. *Phys. Rev. Lett.*, 75, (1995).

[96] H.R. Strauss. The dynamo effect in fusion plasmas. *Phys. Fluids*, 28, (1985).

[97] A. Yoshizawa. Self-consistent turbulent dynamo modeling of reversed field pinches and planetary magnetic fields. *Phys. Plasmas*, 2, (1990).

[98] D. Bonfiglio, S. Cappello, and D.F. Escande. Dominant electrostatic nature of the reversed field pinch dynamo. *Phys. Rev. Lett.*, 94, (2005).

[99] S. Cappello, D. Bonfiglio, and D.F. Escande. Magnetohydrodynamic dynamo in reversed field pinch plasmas: Electrostatic drift nature of the dynamo velocity field. *Phys. Plasmas*, 13, (2006).

[100] Fausto Cattaneo and Steven M Tobias. Dynamo properties of the turbulent velocity field of a saturated dynamo. *Journal of Fluid Mechanics*, 621:205–214, 2009.

[101] Nils Erland L Haugen, Axel Brandenburg, and Wolfgang Dobler. Simulations of nonhelical hydromagnetic turbulence. *Physical Review E*, 70(1):016308, 2004.

[102] S Kenjereš and K Hanjalić. Numerical simulation of a turbulent magnetic dynamo. *Physical review letters*, 98(10):104501, 2007.

[103] Saša Kenjereš and Kemal Hanjalić. Numerical insights into magnetic dynamo action in a turbulent regime. *New Journal of Physics*, 9(8):306, 2007.

[104] B Favier and MRE Proctor. Growth rate degeneracies in kinematic dynamos. *Physical Review E*, 88(3):031001, 2013.

[105] Salah Neffaa, Wouter JT Bos, and Kai Schneider. The decay of magnetohydrodynamic turbulence in a confined domain. *Physics of Plasmas*, 15(9):092304, 2008.

[106] WH Matthaeus, A Pouquet, PD Mininni, P Dmitruk, and B Breech. Rapid alignment of velocity and magnetic field in magnetohydrodynamic turbulence. *Physical review letters*, 100(8):085003, 2008.

[107] S Servidio, WH Matthaeus, and P Dmitruk. Depression of nonlinearity in decaying isotropic mhd turbulence. *Physical review letters*, 100(9):095005, 2008.

[108] Pablo D Mininni. Scale interactions in magnetohydrodynamic turbulence. *Annual Review of Fluid Mechanics*, 43:377–397, 2011.